University of Colorado, Boulder
CU Scholar

Mechanical Engineering Graduate Theses & Dissertations

Mechanical Engineering

Spring 1-1-2014

Advancing Microscope and Probe Design for Near-Field Scanning Microwave Microscopy

Joel C. Weber
University of Colorado Boulder, jcweber16@gmail.com

Follow this and additional works at: https://scholar.colorado.edu/mcen_gradetds

Part of the Mechanical Engineering Commons, and the Nanoscience and Nanotechnology Commons

Recommended Citation
Weber, Joel C., "Advancing Microscope and Probe Design for Near-Field Scanning Microwave Microscopy" (2014). *Mechanical Engineering Graduate Theses & Dissertations*. 87.
https://scholar.colorado.edu/mcen_gradetds/87

This Dissertation is brought to you for free and open access by Mechanical Engineering at CU Scholar. It has been accepted for inclusion in Mechanical Engineering Graduate Theses & Dissertations by an authorized administrator of CU Scholar. For more information, please contact cuscholaradmin@colorado.edu.

ADVANCING MICROSCOPE AND PROBE DESIGN FOR NEAR-FIELD SCANNING MICROWAVE MICROSCOPY

by

JOEL C. WEBER

B.A., Georgia Institute of Technology, 2009

A thesis submitted to the

Faculty of the Graduate School of the

University of Colorado in partial fulfillment

of the requirement for the degree of

Doctor of Philosophy

Department of Mechanical Engineering

2014

This thesis entitled:

Advancing Microscope and Probe Design for Near-Field Scanning Microwave Microscopy

written by Joel C. Weber

has been approved for the Department of Mechanical Engineering

____

Victor M. Bright

____

Pavel Kabos

Date________________

The final copy of this thesis has been examined by the signatories, and we

Find that both the content and the form meet acceptable presentation standards

Of scholarly work in the above mentioned discipline.

Weber, Joel C. (Ph.D., Mechanical Engineering)

Advancing Microscope and Probe Design for Near-Field Scanning Microwave Microscopy

Thesis directed by Professor Victor M. Bright

In this thesis, we address the design and application of a microscope and probes for near-field scanning microwave microscopy. We provide an introduction to the development of microwave microscopy and its contributions to material metrology. In particular, we focus on its application to the study of photovoltaics. We then expand beyond these studies to the fabrication of nanowire-based probes for microwave microscopy. These probes provide avenues for advancing an array of scanning probe techniques, including continued measurements on photovoltaics with improved resolution.

To begin, we present a near-field scanning microwave microscope that has been configured for imaging photovoltaic samples. Our system incorporates a Pt-Ir tip inserted into an open-ended coaxial cable allowing the microwave reflection S_{11} signal to be measured across a sample. A phase-tuning circuit increased impedance-measurement sensitivity by allowing for tuning of the S_{11} minimum down to -78 dBm. A bias-T and preamplifier enabled simultaneous, non-contact measurement of the DC tip-sample current and a tuning fork feedback system provided simultaneous topographic data. Light-free tuning fork feedback provided characterization of photovoltaic samples both in the dark and under illumination. In addition to single-point measurements on Si and GaAs samples, microwave measurements were obtained on a $Cu(In,Ga)Se_2$ (CIGS) sample. The S_{11} and DC features were found to spatially broaden around grain boundaries with the sample under illumination. The broadening is attributed to optically-generated charge that becomes trapped and changes the local depletion of the grain boundaries.

Next, we report on the fabrication of a GaN nanowire probe for near-field scanning microwave microscopy. A single nanowire was Pt-bonded to a commercial Si cantilever prior to either an

evaporated Ti/Al or an ALD W coating, providing a microwave signal pathway. Testing over a calibration sample shows the probe to have capacitance resolution down to ~0.03 fF with improved sensitivity and reduced uncertainty compared with a commercial microwave probe. Imaging of MoS_2 sheets found the probe to be immune to surface contamination, owing to its flexible, high-aspect ratio morphology. By improving microwave and topographical sensitivity in a mechanically robust architecture, this probe serves as an ideal platform for additional complimentary scanning probe techniques.

DEDICATION

This thesis is dedicated to my parents, Eric and Jodi, and my sister Sarah. To my parents, I am extremely lucky to have two such loving and caring people in my life. From childhood, you have taught me the importance of balancing work and play while encouraging me to indulge in all of my interests. Knowing that your support is unconditional has given me the courage to risk failure in the pursuit of success. To my sister, there are not many people who get to grow up with one of their best friends like I did. You proved to be an invaluable crash test dummy down countless driveway obstacle courses and have always been there to share in a laugh at our parents' expense or take me down a peg when needed.

I am extremely grateful to have each of you in my life.

PERSONAL ACKNOWLEDGEMENTS

I would like to extend a special thank you to the roommates I've had during my time in Boulder. To Jesse Capecelatro, Brian Francisco, Jim Cezo, Katie Alexander, Lewis Cox, and Mark Schutte, you guys have all been paramount to surviving the stresses that inevitably surface during graduate school. Whether it was spending long evenings on Prof. Oleg's HW, hours lost in the CO mountain range, or simply enjoying a pint at the Southern Sun, your friendships have defined my experience at CU and, hopefully, for many more years to come.

I would also like to acknowledge two important friendships I've made here that have helped shape both my work and my personal growth over the last five years. To John Burkhardt and Kenny Richards, we've had some unforgettable experiences together. I will always treasure our time spent around campfires, discussing anything and everything under a starry Colorado night sky. It's hard to predict where life will take me in the coming years, but I know that you guys will continue to be a big part of the journey.

Finally, I would like to extend a special thank you to Lola Underwood. Your friendship and unwavering support during the writing of my thesis were instrumental to its successful completion. My committee members have made it clear that your homemade muffins were largely responsible for me passing both my comps and dissertation exams, for which I will be forever grateful. I hope that I will be able to return the favor during whatever challenges life may cast our way.

PROFESSIONAL ACKNOWLEDGEMENTS

I would like to thank my NIST advisers, Dr. Pavel Kabos and Dr. Kris Bertness, for their guidance and the many opportunities they have given me over the last four years. From the beginning, my work here has been beyond the scope of my academic background, but your patience and instruction have opened up research avenues that otherwise would not have been possible. I would also like to thank Dr. Mitch Wallis. Your knowledge and advice were instrumental during my initial foray into microwave microscopy, and your knack for experimental design and troubleshooting has saved me countless times when, as always, research did not go as planned. To the postdocs in our group, Dr. Atif Imtiaz, Dr. Sang Lim, and Dr. Sam Berweger, our discussions have provided me with invaluable insight into navigating both my work and as well as life in general as a graduate student.

Finally, I would like to offer a special thank you to my CU Boulder adviser Prof. Victor Bright. It was your work that inspired me to apply to CU for a graduate degree in the first place. You opened up my pathway to working at a national lab and your wealth of experience kept me on a path towards graduation from the beginning. For all of these opportunities and guidance, I am extremely grateful.

Contents

1 Introduction 1

1.1 Overview 2

1.2 Scope of this Thesis 5

1.3 Literature Review 7

1.3.1 Historical Development of NSMM 7

1.3.2 Theory of NSMM Operation and Modeling 12

1.3.3 Photovoltaic Technologies 24

1.3.4 Alternative Tools for Analyzing Photovoltaic Performance 40

2 Near-Field Scanning Microwave Microscopy Measurements on Photovoltaics 48

2.1 Overview 49

2.2 NSMM Application to Photovoltaics from Literature 50

2.3 Design and Layout of NSMM 56

2.4 NSMM Redesign 61

2.5 Height Profile Measurements 67

2.6 Imaging of Photovoltaics 77

2.7 Modeling of NSMM 85

3 GaN Nanowire Probe for Near-Field Scanning Microwave Microscopy 92

3.1 Overview 93

3.2 Fabrication and Testing of Ti/Al NW Probe 94

3.2.1 Fabrication 94

3.2.2 Microcapacitor Calibration Sample 96

3.2.3 Microwave Results 98

3.2.4 Topography and Mechanical Wear Results 104

3.3 Fabrication and Testing of W-ALD NW Probe 107

3.3.1 Fabrication 107

3.3.2 Microwave Results and Testing 111

3.3.3 Imaging MoS_2 Sample 116

4 Conclusions and Future Work 121

4.1 Summary and Contributions 122

4.1.1 Applying NSMM to Photovoltaics 122

4.2.2 Novel GaN NW Probe for NSMM 123

4.2 Future Work 125

4.2.1 Wafer-Scale Fabrication of NW Probes 125

4.2.2 Development of a p-n Junction LED Multi-Probe 128

4.2.3 Application of NW NSMM Probes to Biological Samples 131

Bibliography 135

List of Tables

2.1 Spot size and intensity values for the multi-channel laser source 66

2.2 GaAs sample properties 70

2.3 Parameters for CIGS samples 73

3.1 ALD Surface Reactions 108

List of Figures

1.1 Picture of NSMM with tuning fork feedback system in contact with Pt-Ir tip 5

1.2 Overview of GaN NW attached to commercial Si cantilever 6

1.3 Different types of near-field microwave probes 10

1.4 Spatial information at the near-field dependent on aperture size 13

1.5 Two-port network 14

1.6 Circuit diagram of sample and RLC circuit 16

1.7 Image charge distribution 19

1.8 $\Delta f/f_0$ vs Q/Q_0 for Si and fused silica 21

1.9 Geometry of COMSOL NSMM model 23

1.10 Model of resonant frequency and S_{11} vs. probe-sample distance 24

1.11 Energy band diagram for a direct bandgap semiconductor 26

1.12 Donor and acceptor levels in a semiconductor 28

1.13 Absorption coefficient as a function of photon energy for Si and GaAs 30

1.14 Recombination process in semiconductors 32

1.15 Simple solar cell structure 33

1.16 Current-voltage characteristic of a Si solar cell 34

1.17 Cross-sectional view of a Si solar cell with screen printed contacts 35

1.18 Cross-sectional view of a $GaInP_2$/GaAs tandem solar cell 37

1.19 Cross-sectional view of a chalcopyrite device structure 38

1.20 Progress in research-cell efficiencies 39

1.21 Photoluminescence decay method 42

1.22 Diffusion process along CIGS grain boundaries 45

1.23 NSOM probe tips 47

2.1 NSMM setup from literature designed to image Si solar cells 51

2.2 Probe tip-solar cell schematic and model 53

2.3 3-D NSMM images of S_{11} dependence on incident light intensities 54

2.4 3-D NSMM images of S_{11} dependence on incident light wavelength 55

2.5 Schematic of original NIST NSMM 57

2.6 SEM image of mechanically cut Pt-Ir tip 58

2.7 Schematic of probe tip construction 58

2.8 S_{11} 2-D scan of sample CS99 60

2.9 Reflection frequency response due to changes in phase shifter 62

2.10 Model of tuning fork holder 64

2.11 Tuning fork probe amplitude as a function of frequency 64

2.12 S_{11} versus frequency with tuning fork in and out of contact 65

2.13 Microwave reflectance resonance curves for GaAs 68

2.14 Cu height-dependent frequency shifts with model 69

2.15 GaAs height-dependent frequency shifts with model 70

2.16 Spatial dependence of height profile measurements on GaAs 71

2.17 Si height-dependent frequency shifts with model 72

2.18 Current density vs. voltage and AFM scans on CS30 and CS70 73

2.19 Frequency shifts for CS30 and CS70 75

2.20 Spectral dependence of quantum efficiency for CS30 and CS70 75

2.21 Difference in frequency shifts plotted against difference in quantum efficiency 76

2.22 Scan of quartz calibration sample 78

2.23 Line scan from quartz topography image 78

2.24 Measured current density vs. internal voltage for CIGS 80

2.25 30 x 30 μm^2 topography, DC, and S_{11} images of CIGS 83

2.26 Magnified image of CIGS S_{11} image 84

2.27 RLC model of NSMM tip-sample interaction 86

2.28 2-D axisymmetric COMSOL model 87

2.29 Meshed COMSOL model 88

2.30 Nanoscale capacitance measurement and tip-sample system 90

2.31 Capacitance as a function of tip-sample distance 91

3.1 Fabrication of a GaN NW NSMM probe 95

3.2 Agilent microwave nose cone and probe holder 96

3.3 Microcapacitor calibration sample 97

3.4 Rocky Mountain Nanotechnology microwave probe 99

3.5 Scan results for Ti/Al NW probe over microcapacitor 100

3.6 S_{11} line cut across microcapacitor 102

3.7 S_{11} mean and max contrasts across microcapacitor 103

3.8 Topography line cut across microcapacitor 105

3.9 Mechanical wear on Ti/Al NW and commercial probes 106

3.10 XRR results on W ALD 109

3.11 XRD results on W ALD 110

3.12 GaN NW probe post W ALD 111

3.13 W ALD probe S_{11} image on microcapacitor 113

3.14 Modeling probe-microcapacitor capacitance interaction 114

3.15 Modeling probe-SiO_2 staircase interaction 116

3.16 Scan results on MoS_2 thin films 118

3.17 Topography line cut differences between W ALD and commercial probes 120

4.1 Selective epitaxial growth of GaN NWs 126

4.2 Wafer-scale fabrication process 127

4.3 Fabrication of a p-n junction NW probe 130

4.4 Damaged Si AFM probe body 131

4.5 Milled GaN NW probe 133

Chapter 1

Introduction and Background

CONTENTS

1.1 Overview 2

1.2 Scope of this Thesis 5

1.3 Literature Review 7

1.3.1 Historical Development of NSMM 7

1.3.2 Theory of NSMM Operation and Modeling 12

1.3.3 Photovoltaic Technologies 24

1.3.4 Alternative Tools for Analyzing Photovoltaic Performance 40

1.1 Overview

Near-field scanning microwave microscopy (NSMM) integrates a microwave signal path into a scanning probe microscope to enable nanoscale spatially resolved measurements of impedance. NSMM impedance measurements reveal quantitative information about a variety of complex electromagnetic material properties including sheet resistance, dielectric constant, and calibrated nanoscale capacitance. These capabilities make the NSMM suitable for studying a diverse range of advanced materials and devices. However, continued improvements are necessary to fully realize imaging of unique structures while ensuring that measurements are repeatable and quantifiable. The work presented in this thesis comprises part of a continuing effort to meet this goal and can be divided into two broad sections: (1) advancing NSMM microscope design with the aim of enabling high-resolution imaging of photovoltaics, and (2) advancing NSMM probe design by improving signal-to-noise resolution and creating a mechanically robust foundation suitable for other scanning probe technologies.

Advancing microscope design was largely driven by our desire to apply the NSMM's measurement capabilities to photovoltaic materials with the goal of better understanding the relationship between material properties, device morphology, and device performance. Third-generation photovoltaics, in particular, are affected by the location and orientation of grains, defects, compositional variations, and engineered interfaces, thus requiring novel, nanoscale imaging techniques to compliment traditional solar cell characterization methodologies.

The NSMM presented in this work relies on a sharp tip to achieve nanoscale resolution. The complex impedance is a strong function of the tip-sample distance; therefore, height control throughout the entire scan is imperative for accuracy and extraction of quantitative information. Early NSMM technology lacked this ability and was only capable of producing images where topographical information was convolved with the measurement of electrical properties.

However, the development of combined atomic force microscopy (AFM) / microwave microscopy enabled simultaneous acquisition of topographical and microwave data. While this has proved suitable for the study of semiconductor-based devices, complete characterization of photovoltaics requires the ability to image in both the dark and under illumination. This constraint precludes the use of laser beam-bounce systems, which are traditionally found in AFM feedback loops, as such schemes may unintentionally illuminate the sample under test. NSMM designs based on a tuning-fork feedback system eliminate such sources of stray light while permitting simultaneous, non-contact measurements of topographic and electromagnetic material properties. Previously, tuning-fork-based NSMMs have successfully imaged homogeneous, doped Si solar cells and measured material properties as a function of illumination wavelength and intensity.

We present a new NSMM that combines simultaneous topographical, microwave, and direct current (DC) data collection capabilities. This system operates in both dark and illuminated states, has imaging capabilities at multiple microwave frequencies in the range 1 GHz–20 GHz, and achieves nanometer-scale spatial resolution while scanning at room temperature in ambient air. Operation in the microwave near-field regime permits surpassing the free-space Abbé resolution limit of half wavelength (on the order of centimeters for gigahertz signals in free space). The interaction of the NSMM probe with the sample can be simulated as a perturbation of a resonant microwave circuit. This tip-sample interaction changes the resonant frequency and quality factor (Q) of the reflected microwave signal.

In addition to improving the application of NSMM to photovoltaics, we also advanced probe design for commercial AFM-based NSMMs with an eye towards creating a suitable foundation for the development of a multi-probe capable of merging multiple microscopy technologies. One example of a commonly used NSMM probe consists of a Pt metal cantilever and tip affixed to a dielectric chip. Because AFM-based NSMMs image in a contact-scanning mode, these metal probe tips are susceptible to wear over time. This wear alters the probe radius, affecting scan

resolution and the tip-sample complex impedance. Scan-to-scan variability impedes efforts to quantify microwave measurements and necessitates repeated calibration procedures over time.

We have significantly reduced the problem of mechanical-wear on the probe while increasing microwave resolution through the incorporation of a GaN nanowire (NW) into a commercial Si probe. Nanostructures, particularly carbon nanotubes, have been used to improve a variety of scanning probe technologies including atomic force microscopy, scanning tunneling microscopy, and near-field optical microscopy. Their high-aspect ratios provide improved topographical resolution while their material properties can be manipulated to control their mechanical and electrical response. In our case, the defect-free nature of the GaN NWs minimizes wear during contact scanning while improving electrical contact with the sample under study. Furthermore, their flexible nature causes the NW probes to be relatively immune to surface contaminants when compared against commercial Pt tips.

Although the GaN NW NSMM probes presented in this thesis are manufactured one at a time with homogeneous NWs, they provide the foundation for continued advances in a variety of scanning probe fields. The development of a wafer-scale process will enable commercialization of these NW probes while the incorporation of a p-n junction through doping during the growth phase will enable the NWs to emit light. Among other imaging possibilities, such advancements will make the probes suitable for characterizing photovoltaics without the use of an external laser.

1.2 Scope of this Thesis

The first portion of the work presented in this thesis has primarily focused on the design and operating procedure for a NSMM suited to the study of photovoltaic samples. Research initially centered on characterizing bulk material properties by conducting single point height profile measurements in an effort to characterize microscope sensitivity. Work progressed to high resolution, noncontact scanning of photovoltaic samples under varying illumination conditions through a redesign of the NSMM. The primary improvement was the implementation of a tuning fork feedback system capable of maintaining ~10 nm control over varied sample topography (Fig. 1.1). Ongoing studies on a variety of photovoltaic samples and other samples of interest provide future avenues to better understand device properties at the micro- and nanoscale.

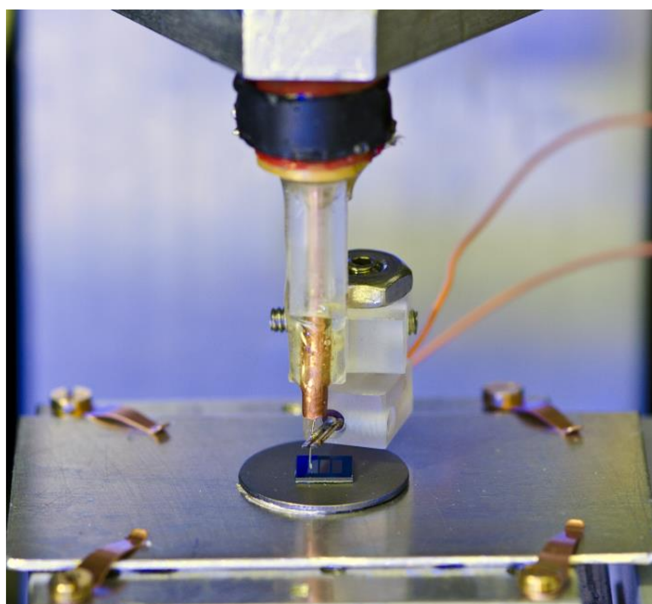

FIG. 1.1. Picture of NSMM highlighting tuning fork feedback system in contact with Pt-Ir tip. Tip is currently held ~10 nm over the calibration sample.

The second portion of this work centered on fabricating an improved probe compatible with commercial NSMM systems. Using the nanomanipulator in the focused ion beam, a single GaN

nanowire grown through molecular beam epitaxy was harvested and attached to a commercial Si cantilever (Fig. 1.2). The entire probe structure was coated with either sputtered Ti/Al or atomic layer deposition of W to provide a microwave pathway. For testing, these nanowire probes were inserted into an Agilent 5400 NSMM and used to image a microcapacitor calibration sample developed at NIST. When compared against a commercial Pt NSMM probe, the NW probe showed improved microwave sensitivity coupled with reduced mechanical wear. Benefits in microwave and topographical resolution from imaging over 2-D thin MoS_2 sheets will also be explored. The probe provides the structural foundation for the future development of a light-emitting multi-probe encapsulating a multitude of scanning probe capabilities.

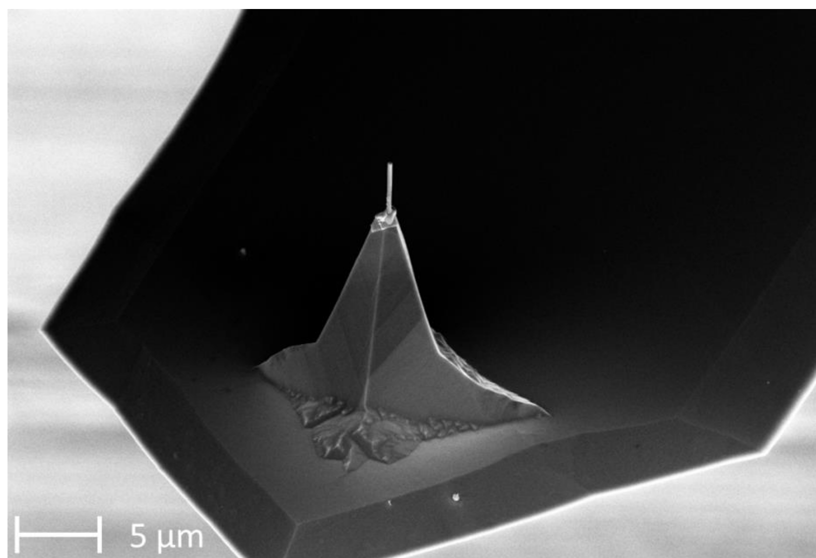

FIG. 1.2 Overview of GaN NW attached to a commercial Si cantilever using a Pt weld.

1.3 Literature Review

1.3.1 Historical Development of NSMM

Near-field scanning microwave microscopy can trace its origins back over eighty years to a forward-looking proposal by Synge aspiring to take advantage of evanescent waves in an effort to surpass the Abbe limit[1]. This limit restricts the resolving power of far field microscopes to approximately $\lambda/2$, where λ represents the wavelength of light used to illuminate the sample. While we will investigate the origins and implications of this law more closely later in this thesis, it served for a long time to prevent precision microscopy from entering the realm of invisible electromagnetic waves even with the development of relevant electronic detectors. Synge proposed replacing the simultaneous data acquisition of standard optical microscopy with a point by point scanning technique. His microscope called for an opaque-screen with a 10 nm diameter hole to be moved at a height 10 nm above a transparent sample. Visible light shined through the hole would be collected in a raster scan. The position control and precision in machining needed to achieve his goal were well beyond the technical limits of the time and his idea would remain dormant for nearly forty years until independent work by Frait and Soohoo provided the first experimental verification at microwave frequencies[2-3]. By studying a traditional ferromagnetic resonance cavity (FMR), they determined that the cavity averaged over material properties for samples placed inside of it, providing macroscopic information. By inverting the design and placing the sample under the cavity with a small hole for microwave coupling, they created the first FMR microwave microscope. While the hole size (500 µm) was significantly larger than Synge's initial proposal, the use of microwave frequencies in the range of 5 - 10 GHz (λ = 6 - 3 cm) demonstrated sample contrast well below the Abbe limit.

A similar experiment by Ash and Nicholls at 10 GHz with a 1.5 mm aperture helped introduce several important and currently used concepts to NSMM measurements and opened the field to the wider science community[4]. The microscope incorporated a quasi-optical hemispherical resonator with a 10 GHz resonant frequency that provided high Q for the reflected microwave signal. They used this sensitivity to measure changes in sample permittivity down to 10 % in non-contact mode with lateral resolution of 0.5 mm. The sample under study was modulated at a constant frequency while being scanned under the aperture. The microwave reflection signal was then phase-selected at the modulation frequency to improve signal to noise resolution. At the time, this technique demonstrated contrast sensitivity to metal films deposited on dielectric substrates and is still widely used in NSMM applications today.

While the initial foundation for resonant based NSMM was being developed, other work led by Bryant and Gunn focused on non-resonant aperture probes[5]. Their microscope relied on a coaxial transmission line to carry microwave signal down to the aperture and allow interaction with the sample under study. Although some of the microwave energy was absorbed by the sample or stored in evanescent waves, a portion was either reflected back along the transmission line or scattered as far-field radiation. Either of these latter effects could be monitored as a function of sample position with respect to the aperture, allowing an image to be formed while quantitatively measuring semiconductor resistivities. Their coaxial design, while limited in terms of resolving power compared with the microscope reported in this thesis, shared the same fundamental operating principles. It consisted of an open-ended coaxial probe with an inner conductor that tapered down to 1 mm. This concept was expanded upon in the coming years through work by Fee, Chu, and Hansch. Their open-ended coaxial center line had a reduced diameter of 500 µm with an end that tapered down to 30 µm[6]. They successfully reported reflected microwave and phase shift signal with a spatial resolution exceeding the Abbe limit by over three orders of magnitude.

The preceding developments largely set the stage for NSMM to flourish into a powerful metrology tool capable of studying a vast array of devices including semiconductors, biological samples, and, more recently, photovoltaics. Before delving into specifics in feedback control and circuit design, it would be beneficial to first separate NSMM designs into two distinct categories: aperture-based and aperture-less, with Fig. 1.3 providing several examples of both implementations[7-13]. Aperture-based NSMM represents a realization of the concept first put forth by Synge. It uses a sub-wavelength aperture to limit the interaction of the probe with the sample to a very small volume. The works discussed above by Synge, Frait, Soohoo, and Ash and Nicholls all fall into this category. Aperture-less probes, on the other hand, rely on a field concentrating feature to localize microwave interaction with the sample. These features typically take the form of AFM probes or STM tips which have been integrated into the microwave signal path and often result in much stronger signals with higher sensitivity to electromagnetic changes within the sample. The early works of Bryant and Gunn as well as Fee, Chu, and Hansch describe this design. Due to its increased resolution, sensitivity, and ease of implementation with other modern microscopy techniques, the NSMM design in this thesis follows the aperture-less model.

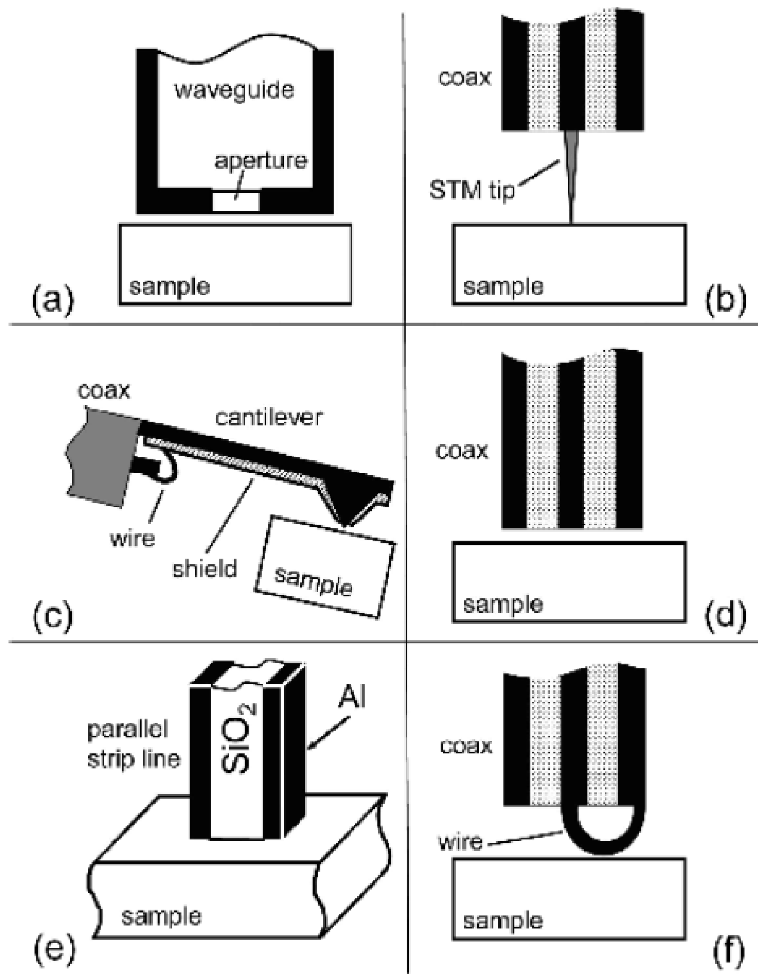

FIG. 1.3 The main types of near-field microwave probes: (a) aperture in a waveguide, (b) STM tip, (c) AFM tip, (d) open end of coaxial line, (e) parallel strip transmission line, and (f) magnetic loop. Figure from reference[14].

The complex impedance typically measured by NSMM is a strong function of the tip/sample distance. Therefore, height control throughout the entire scan is imperative for accuracy in scanning and extraction of quantitative information. Early NSMM technology lacked this ability and was only capable of producing images where topographical information was convolved with the measurements of electrical properties[13]. However, a variety of means have been developed which enable simultaneous acquisition of topographical and microwave data, as well as the

subsequent extraction of quantitative measurements. First, we will review the scanning tunneling based distance control, which was initially used in a modified form with our NSMM. The scanning tunneling microscope (STM) will be reviewed in more detail in the alternative microscopy tool section, but for now, it will suffice to mention that this technique establishes a quantum mechanical vacuum tunneling current at extremely close distances between the tip and a conducting or semiconducting sample (~1 nm)[15]. While extremely accurate, ideal operating conditions include a low temperature, high vacuum environment and preclude the use of insulating samples. As mentioned before, the STM tip serves as the microwave concentrating feature during measurements.

A second technique is based on the principle of shear force based distance control. This concept was pioneered for use with near-field scanning optical microscopy (NSOM) as a means to enable nanometer precision height control[16-17]. Because a typical NSOM tip consists of a flexible optical fiber, it can be readily attached to a quart tuning fork or piezoelectric element and dithered via an input AC signal. Optical or electrical feedback tracks changes in the frequency, phase, or amplitude of the driven motion of the tuning fork as the tip interacts with the sample, providing necessary height changes during scanning. Shear force feedback has been demonstrated on a variety of probe structures and can be useful in photovoltaic NSMM studies due to its ability to operate without an external light source. As such, it was chosen as the primary feedback during the redesign of the NSMM reported in this thesis[18-20].

The advent of atomic force microscopy (AFM) has provided the basis for a wide array of advanced microscopy techniques. The ability to combine a variety of measuring capabilities with the AFM's sub-nanometer resolution feedback system on both insulating and conducting materials makes it a powerful foundation for microscopy. The repulsion force between the tip and the sample provides height information during an NSMM scan while microwave transmission lines carry signal down to the field concentrating tip via a signal path built into the AFM cantilever[21-22].

This concept will be utilized to create the nanowire AFM probe presented in Chapter 3 of this thesis. Additional NSMM designs have also sought to combine AFM tapping mode feedback with sample height modulation to improve sensitivity to material parameters[23].

1.3.2 Theory of NSMM Operation and Modeling

The power of the NSMM lies in its ability to probe samples at microwave frequencies while greatly surpassing the far-field diffraction (Abbe) limit[24]. In the far-field, the image is constructed purely by propagating waves. The resolution limit arises by measuring the radius (d) and angle (θ) of convergence of a lens used to focus light propagating through a medium with index of refraction n:

$$d = \frac{\lambda}{2(n \sin \theta)} \qquad 1.1$$

where $n \sin \theta$ is known as the numerical aperture and has an ideal value of 1, resulting in a resolution limit of $\sim\lambda/2$. The wave number of these propagating waves is given by

$$k = \frac{2\pi}{\lambda} = \sqrt{k_x^2 + k_y^2 + k_z^2} \qquad 1.2$$

where k_x, k_y, and k_z are real numbers. However, these purely real solutions to the wave equation cannot fully describe a spherical wave with a wave front radius smaller than λ[13, 25-26]. NSMM gives rise to such a situation with the introduction of near-field interactions involving the air-conductor boundary of a sharp tip or the sub-wavelength dimensions of an aperture (Fig. 1.4).

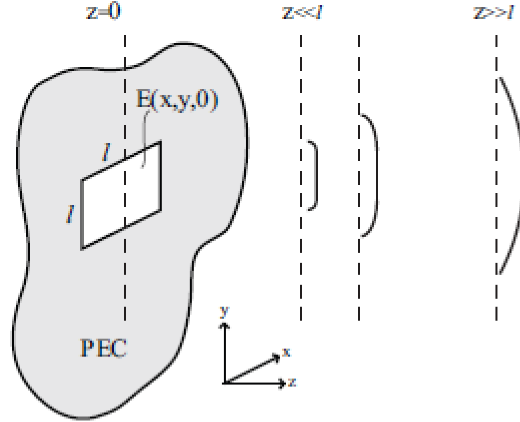

FIG. 1.4. The near-field of an aperture carries with it spatial information on the order of the aperture size. This creates a sampling function of small spatial extent and allows the NSMM to measure a sample under study in a small area. Figure from reference[13].

To fully describe such a spherical wave, complex solutions to the wave equation must be taken into account. For our purposes, this involves a complex k_z to arise which decays exponentially and typically cannot propagate beyond $\sim\lambda$. These waves are known as evanescent waves whose wave number contains a larger lateral component

$$k_r = \sqrt{k_x^2 + k_y^2} \qquad 1.3$$

leading to increased lateral resolving power $\sim 1/k_r$. The sharp-tip (radius R_0) geometry of the NSMM reported in this thesis also leads to the development of near-field evanescent waves in order to form a spherical wave and satisfy the tip/air boundary condition. This geometry results in $k_r \sim 1/R_0$ and lateral resolution approaching $\sim R_0$. Evanescent wave decay length also restricts useful tip-sample distance to $\sim R_0$, and lateral resolution may be increased further for samples with a high effective permittivity.

Before delving into NSMM modeling, we will briefly outline the microwave reflection coefficient S_{11} and its units. The scattering matrix (S-matrix) is used to mathematically define how microwave power propagates through an N-port network. S-parameters are complex values containing both magnitude and phase information (we tracked both during image scans of photovoltaics)[27]. S-parameters vary as a function of frequency across the network and thus the operating frequency of the vector network analyzer must be defined. We will limit our discussion here to a two-port network which covers the majority of NSMM transmission and reflection studies (Fig. 1.5).

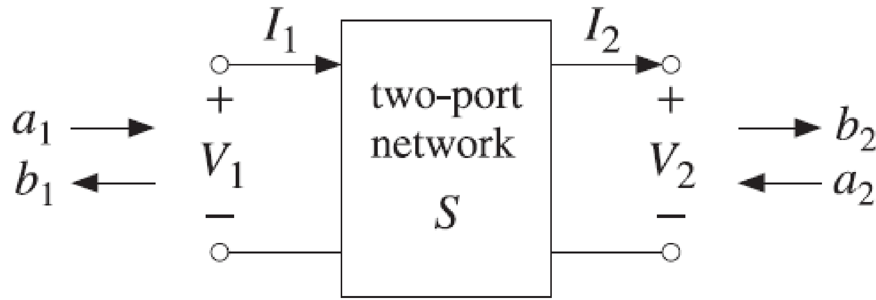

FIG. 1.5. Two-port network.

Incident power on each port is characterized by a_n while output power is characterized by b_n. The S-parameter matrix provides the relationship between these incident and reflected powers:

$$\begin{pmatrix} b_1 \\ b_2 \end{pmatrix} = \begin{pmatrix} S_{11} & S_{12} \\ S_{21} & S_{22} \end{pmatrix} \begin{pmatrix} a_1 \\ a_2 \end{pmatrix} . \qquad 1.4$$

Expanding the matrix gives the output powers

$$b_1 = S_{11}a_1 + S_{12}a_2 \qquad 1.5$$

$$b_2 = S_{21}a_1 + S_{22}a_2 \, . \qquad 1.6$$

For each of the above S-parameters, the first number refers to the responding port while the second number refers to the incident port. As such, S_{21} is a measurement of the response of port 2 due to an incident power on port 1. For our system, we are concerned with the reflection S-parameter S_{11}. Following the same guidelines, this is a power measurement on port 1 due to an incident power on port 1, making our microwave circuit a one-port network. S_{11} can further be described by its impedance relationship

$$S_{11} = \frac{Z_L - Z_0}{Z_L + Z_0} \qquad 1.7$$

where Z_L is the load impedance and Z_0 is the characteristic impedance of the circuit (typically 50 Ω). S-parameters for this paper are reported with units dBm, indicating a dimensionless power ratio in W/mW.

Several methods have been put forth to analytically and computationally model the near field interactions between the NSMM and sample under study. Here, we will consider a lumped element method that develops equations for the height-dependent coupling capacitance between the tip and sample. This method will be tailored to our NSMM's circuit in Section 2.7, but many of the concepts introduced here still apply. We will also investigate work completed on full wave simulations regarding similar microscopes. These efforts, with mixed success, all seek to quantitatively understand NSMM measurements.

Imtiaz relied on a lumped element model based off of a resistance-inductance-capacitance (RLC) resonator[26, 28]. A complete transmission line model could be avoided while still maintaining accuracy due to the limited bandwidth of interest for particular measurements. Furthermore, the lumped element model provided the opportunity to develop material-property-dependent equations that afforded insight into quantitative changes in the microwave signal during measurement. As depicted in Fig. 1.6, the NSMM resonator was modeled as a resistor R_0, an inductor L_0, and a capacitor C_0 all in parallel. An additional parallel term for the sample properties is included with

its own resistance R_x and capacitance C_x in series[14, 29]. As is also true the NSMM presented in Chapter 2, a change in the sample inductor L_x element can be safely ignored as it is not relevant in the frequency regime of interest.

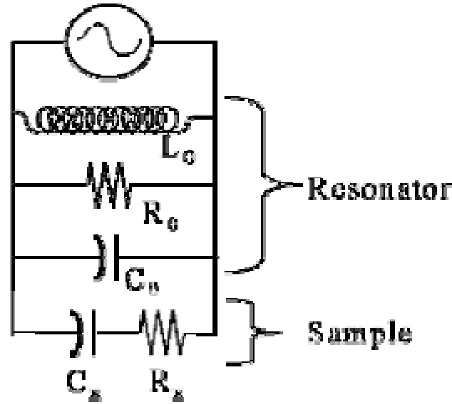

FIG. 1.6. The circuit diagram of the lumped element model where L_0, R_0, and C_0 are in parallel and represent a single resonance of the resonator. The sample is added as a series R_x and C_x in parallel to the resonator and RLC circuit. Figure from reference[26].

The total impedance of the simple circuit from Fig. 1.6 can be calculated as follows:

$$Z_T = \frac{1}{\frac{1}{i\omega L_0}+\frac{1}{R_0}+i\omega C_0+\frac{1}{Z_{sample}}}, \tag{1.8}$$

where Z_{sample} is given by:

$$Z_{sample} = R_x + \frac{1}{i\omega C_x}. \tag{1.9}$$

By expanding the first equation, the new RLC circuit elements can be calculated in the form

$$Z_T = \frac{1}{\frac{1}{i\omega L}+\frac{1}{R}+i\omega C}, \tag{1.10}$$

with L, C, and R now defined by:

$$L = L_0 \tag{1.11}$$

$$C = C_0 + \frac{1}{1+(\omega C_x R_x)^2} \tag{1.12}$$

$$R = R_0 \frac{1+(\omega C_x R_x)^2}{(1+(\omega C_x R_x)^2 + \frac{R_0}{R_x}(\omega C_x R_x)^2)} . \tag{1.13}$$

We can now step back and give the equations governing the quality factor (Q), the resonant frequency (*f*), and the resonant frequency shift (Δf):

$$Q = R\sqrt{\frac{C}{L}} \tag{1.14}$$

$$f = \frac{1}{2\pi\sqrt{LC}} \tag{1.15}$$

$$\Delta f = f - f_0 \tag{1.16}$$

where $f_0$is the initial resonant frequency before changes due to sample properties and/or tip-sample height.

In this model, we can further break down the sample capacitance C_x into two parts: capacitance due to sample material properties C_{sample} and capacitance due to the tip-sample height and geometrical properties $C_{coupling}$. During height profile measurements where the tip-sample distance is slowly increased while measuring changes in Q and Δf, the $C_{coupling}$ capacitance is responsible for the majority of changes in the RLC resonant model. Gao developed a means by which to calculate this capacitance as a function of height using the method of images[7, 26, 30]. The use of this quasi-static model is possible because measurements are taken in the near-field regime. The NSMM probe is represented by a sphere of radius R_0 and initial potential V_0. The sphere is held over a conducting plane that extends infinitely in the radial direction with zero potential (in practice, our NSMM reverses these biasing conditions but the end result is the same). The charge, initially located at the origin of this sphere, is given by

$$q = 4\pi\varepsilon_0 R_0 V_0 \ , \tag{1.17}$$

where ε_0 is the permittivity of free space. Using the method of images, the conducting plane can be removed and the initial charge balanced with an image charge of $-q$, thus reestablishing zero potential at the infinite plane. This new image charge disrupts the equipotential surface at the spherical boundary of the first sphere, requiring a new charge located within the sphere to once again establish V_0 (Fig. 1.7). This process is repeated until the electric field distribution and $C_{coupling}$ converge to an acceptable limit.

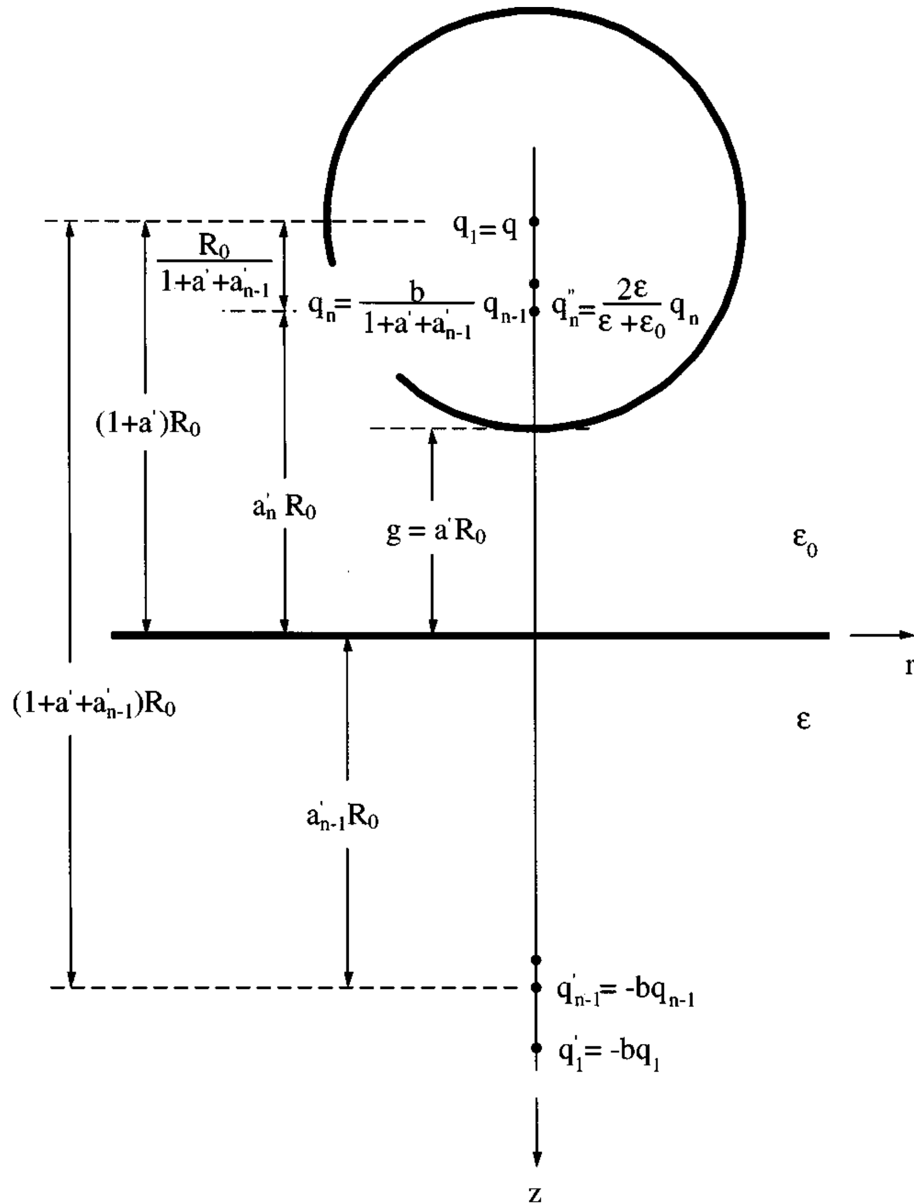

FIG. 1.7. Image charges distribution for the configuration with an air gap between a thick sample and tip. Figure from reference[7].

Using the cylindrical coordinate system defined by r and z in Fig. 1.7, the nth image charge is given by

$$q_n = \frac{q_{n-1}}{1+a_0+a_{n-1}} \tag{1.18}$$

$$a_n = 1 + a_0 - \frac{1}{1+a_0+a_{n-1}} \qquad 1.19$$

$$a_0 = \frac{g}{R_0} \qquad 1.20$$

where g is the gap between the sphere and the infinite plane. The resulting field distribution and $C_{coupling}$ are then

$$E_s = \frac{2}{4\pi\varepsilon_0}\sum_{n-1}^{\infty} q_n \left\{\frac{r.\hat{r}+(z+a_nR_0)\hat{z}}{(r^2+(z+a_nR_0)^2)^{\frac{3}{2}}} - \frac{r.\hat{r}+(z-a_nR_0)\hat{z}}{(r^2+(z-a_nR_0)^2)^{\frac{3}{2}}}\right\} \qquad 1.21$$

$$C_{gap} = \left(\sum_{n-1}^{\infty} q_n\right)/V_0 \, . \qquad 1.22$$

This capacitance converges to the following equation:

$$C_{gap} = r\pi\varepsilon_0 R_0 \sinh(\alpha) \sum_{n-1}^{\infty} \frac{1}{\sinh(n\alpha)} \qquad 1.23$$

$$\alpha = cosh^{-1}(1 + \frac{h}{R_0}) \, . \qquad 1.24$$

Gao used this relation to calculate frequency shifts as a function of $C_{coupling}$ and the fitting parameter A which is dependent on the geometry of the NSMM resonator [30]

$$\frac{\Delta f}{f_0} = -A\{C_{gap}(a_0)\} \, . \qquad 1.25$$

This general approach has been used to determine changes in resonant frequency and quality factor as a function of tip-sample height, enabling modeling of experimental data on bulk, homogeneous samples (Si and fused silica)[31]. Fig. 1.8 illustrates $\Delta f/f_0$ plotted as a function of Q/Q_0 as the tip was retracted away from the sample over a 0.1 – 1000 µm range. To provide an ideal fit using the RLC lumped element model with image charge capacitance calculations, four fitting parameters were used: tip radius r_0, tip geometry D, sample permittivity ε_s, and sample conductivity σ[8]. r_0 was assumed to be smaller than the 40 µm radius of the tungsten wire used for the probe and was

held at 30 μm. Published values for Si provided $\sigma_{Si} = 50\ S\ m^{-1}$ and $\varepsilon_s = 11.9$, leaving D to be varied. Similarly, fused silica values of $\varepsilon_s = 3.85$ and $tan\delta = 1.0 \times 10^{-4}$ were fixed. The best fits in Fig. 1.8 were found by setting $D = 1.35$ and $D = 2.25$. With Dr_0 representing the effective tip geometry, the difference in values between the two samples describes their ability to concentrate the electric field under the tip during scanning. Meanwhile, the sample conductivity partially determines the sample's capacitance due to its dependence on complex permittivity. This becomes important for photovoltaic measurements by NSMM as changes in photoconductivity provide different fits to height profile measurements completed under different illumination conditions.

$$\varepsilon^*(\omega) = \varepsilon_s + \frac{i\sigma}{\omega} \tag{1.26}$$

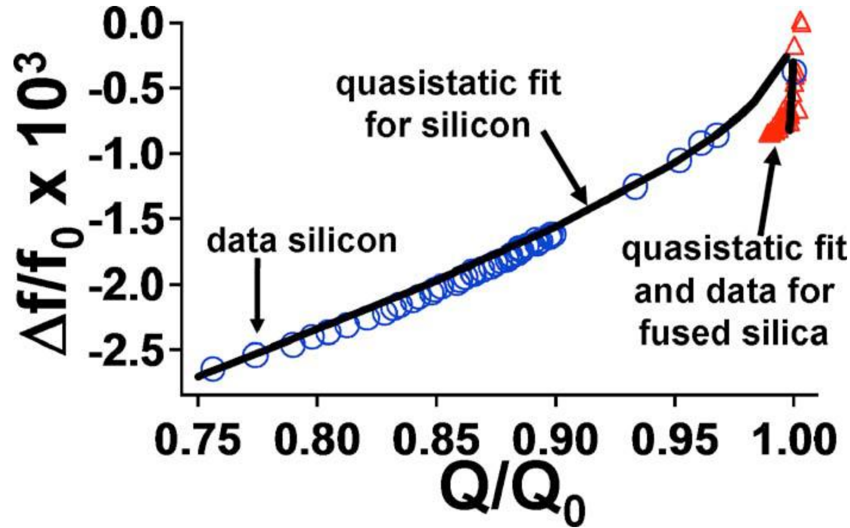

FIG. 1.8. $\Delta f/f_0$ vs Q/Q_0 plotted for the Si and fused silica. The y axis is sensitive to C_x to first order, and the x axis to the materials' loss. Both materials fit well with the conventional quasi-static models. The measurement was performed at heights from 0.1 to 1000 μm. Figure from reference[31].

Analytical models are powerful in their ability to provide insight into fundamental relations between NSMM response, tip geometry, tip-sample distance, and sample material properties.

However, complicated multilayer samples (such as third-generation photovoltaics) quickly complicate calculations and stretch the limits of bulk, homogeneous material assumptions. To help tackle this problem, full wave simulation programs such as ANSYS High Frequency Structure Simulator (HFSS), Ansoft Maxwell 2D (M2D), and COMSOL Multiphysics have been explored. These programs are capable of examining quasi-static capacitance calculations, visualizing field concentrations between the tip and sample, as well as providing full frequency sweeps to determine microwave coefficients dependent on changing measurement conditions. However, these programs require detailed understanding of the boundary conditions prescribed and can be limited in computational accuracy due to the large aspect ratios involved in a full NSMM model.

We will briefly examine one pertinent computational COMSOL model of the NSMM used to study Si solar cells that will be discussed in further detail in Section 2.5. It consists of a microwave cavity with a thin metal rod protruding through a small hole on one side (Fig. 1.9)[32]. A metallic loop on one side of the rod serves to couple it to the cavity while the tip of the rod is held in close proximity to the sample under study. A vector network analyzer provides microwave signal and measures the microwave reflection coefficient S_{11} via a transmission line. Length scales within this model range from < μm (tip geometry and tip-sample distance) to cm (microwave cavity), thus presenting a challenging meshing problem. Qualitatively, S_{11} amplitude and frequency shifts as a function of tip-sample distance accurately mirrored experimental results (Fig. 1.10). However, quantitatively, the model's sensitivity to sample permittivity changes was a factor of four too large while frequency shifts were approximately 10 % higher than expected. These errors can be largely attributed to the computational necessity which restricted tip dimensions to 1 mm, as opposed to the experimental values of 50 μm. Improvements in meshing technique, as well as increased computational power, will continue to refine these results, but currently, full-wave computational simulation of an NSMM's frequency dependence remains qualitative in nature.

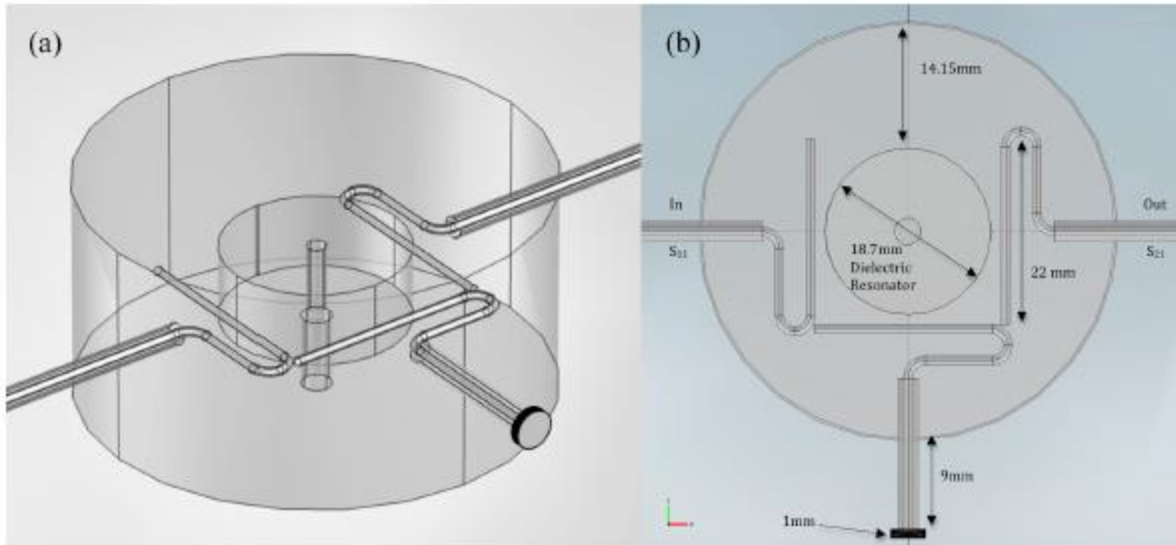

FIG. 1.9. Geometry of the NSMM. (a) Model as it appears in the COMSOL interface. The surrounding sphere is not shown. (b) Horizontal 2D cross Section through the center plane of the cavity. The central conductor (inner cylinder) of the coaxes enters and leaves the cavity from the left and right, respectively. Only the inner conductor of the coaxes enters the cavity; the outer cylinder inside the cavity is a false boundary. The outer cylinder of the probe (the lower hook) is everywhere a false boundary. The 50 μm layers of the sample are not resolved in the figure. Figure from reference[32].

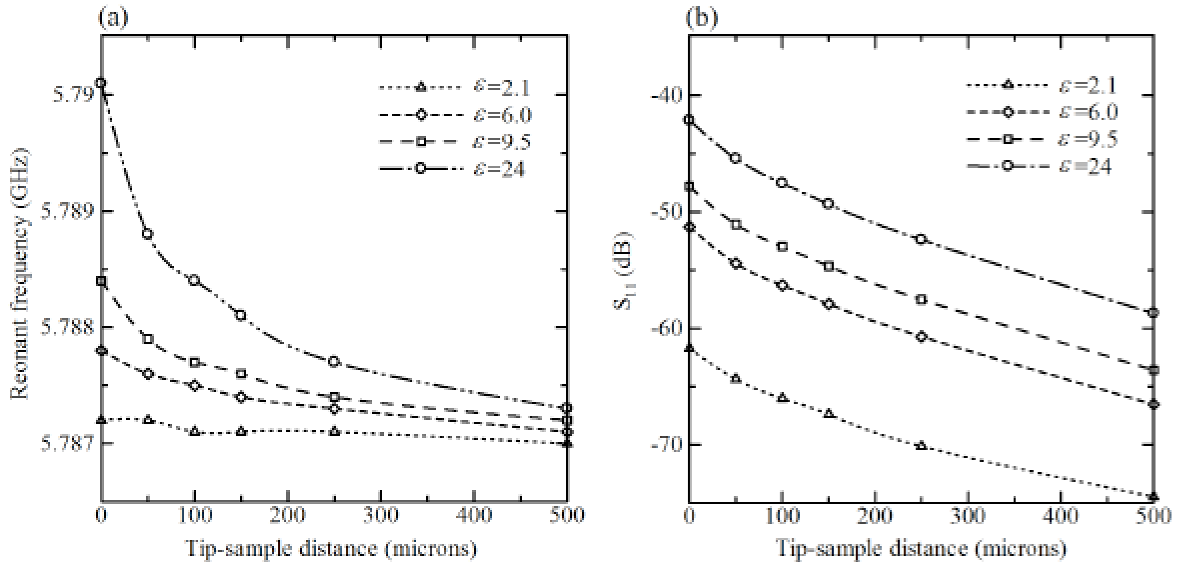

FIG. 1.10. (a) Resonant frequency and (b) reflection coefficient minimum S_{11} vs. probe-sample distance. Dielectric constants are $\varepsilon = 2.1, 6, 9.5, 24$ and probe-sample distances range from 0 to 500 μm. The sample is 50 μm thick. Figure from reference[32]

1.3.3 Photovoltaic Technologies

The direct conversion of incident light into electric energy by use of a p-n junction is known as the photovoltaic effect. While understood for many years, it was not until a breakthrough with Si solar cells in 1954 that the phenomenon became the foundation for a viable renewable energy technology[33]. Initial development was driven with the realization that solar energy provided a useful means by which to power remote structures in off-the-grid locations including satellites, weather monitoring stations, and communications equipment[34]. Advances brought photovoltaic applications into other industries including consumer electronics and utilities. Today, research continues to push thin film third-generation photovoltaic technologies that merge low production cost with high operating efficiencies.

Before delving into material specifics, it is useful to examine the fundamental physics behind photovoltaic operation. Section 1.4 will cover a series of traditional measurement techniques as well as new microscopy-based methods used to characterize photovoltaic performance. However, we will begin by defining terms relevant to photovoltaic carrier concentrations as well as discussing absorption, recombination, the p-n junction, and solar cell efficiency[35]. Figure 1.11 provides a simplified energy band diagram for a direct bandgap semiconductor showing the presence of electrons in the conduction band (E_C) and holes in the valence band (E_V) at thermal equilibrium. The density of states of each band can be found by the following equations:

$$g_C(E) = \frac{m_n^*\sqrt{2m_n^*(E-E_C)}}{\pi^2\hbar^3} cm^{-3}eV^{-1} \quad 1.27$$

$$g_V(E) = \frac{m_p^*\sqrt{2m_p^*(E_V-E)}}{\pi^2\hbar^3} cm^{-3}eV^{-1} \quad 1.28$$

where m_p^* and m_n^* represent the effective mass of the holes and electrons respectively.

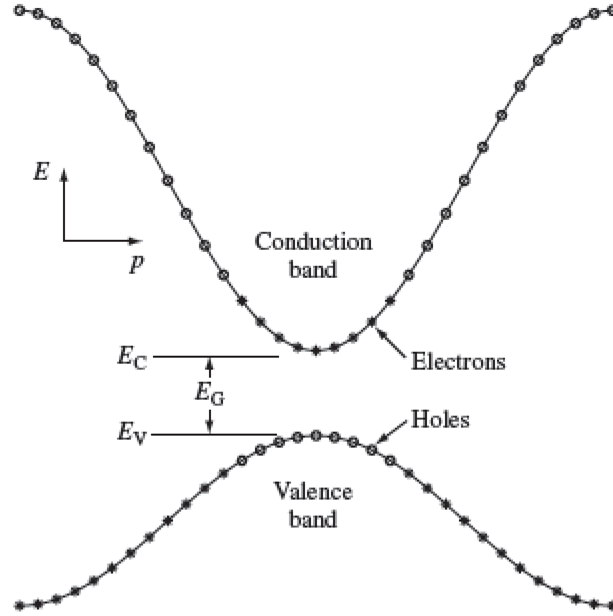

FIG. 1.11. A simplified energy band diagram at T > 0 K for a direct bandgap (E_G) semiconductor. Electrons near the maxima in the valence band have been thermally excited to the empty states near the conduction-band minima, leaving behind holes. The excited electrons and remaining holes are the negative and positive mobile charges that give semiconductors their unique transport properties. Figure from reference[35].

The density of states can be used to calculate the equilibrium electron and hole concentrations (#/cm^{-3}) with the introduction of the Fermi function:

$$f(E) = \frac{1}{1+e^{(E-E_F)/kT}} \qquad 1.29$$

where E_F is the Fermi energy, k is the Boltzmann's constant, and T is the temperature in Kelvin. The Fermi function provides the ratio of filled states to available states for each energy level at thermal equilibrium (at constant temperature with no external injection or carrier generation). The electron and hole concentrations are now given as:

$$n_o = \int_{E_C}^{\infty} g_C(E) f(E) dE = \frac{2N_C}{\sqrt{\pi}} F_{\frac{1}{2}}(\frac{E_F-E_C}{kT}) \qquad 1.30$$

$$p_o = \int_{-\infty}^{E_V} g_V(E)[1 - f(E)]dE = \frac{2N_V}{\sqrt{\pi}} F_{\frac{1}{2}}(\frac{E_V - E_F}{kT}) \quad 1.31$$

where $F_{\frac{1}{2}}(\xi)$ is the Fermi-Dirac integral of order ½ and is given by

$$F_{\frac{1}{2}}(\xi) = \int_0^{\infty} \frac{\sqrt{\xi'} d\xi'}{1+e^{\xi'-\xi}} . \quad 1.32$$

The conductive and valence band densities of state are calculated as:

$$N_C = 2(\frac{2\pi m_n^* kT}{h^2})^{3/2} \quad 1.33$$

$$N_V = 2(\frac{2\pi m_p^* kT}{h^2})^{3/2} \quad 1.34$$

In a nondegnerate semiconductor (E_F is $> 3kT$ from either band edge), the carrier concentrations can be approximated as[36]:

$$n_o = N_C e^{(E_F - E_C)/kT} \quad 1.35$$

$$p_o = N_V e^{(E_V - E_F)/kT} \quad 1.36$$

For an intrinsic semiconductor, the electron and hole carrier concentrations are equivalent and equal to the intrinsic carrier concentration:

$$n_i = \sqrt{n_o p_o} = \sqrt{N_c N_V} e^{-E_G/2kT} . \quad 1.37$$

The Fermi Energy for the intrinsic semiconductor is given by:

$$E_i = \frac{E_V + E_C}{2} + \frac{kT}{2} \ln(\frac{N_V}{N_C}). \quad 1.38$$

The conductivity of a semiconductor can be controlled through the introduction of donor and acceptor impurities. The former donates additional electrons to the conduction band while the latter accepts electrons and leaves behind holes. These impurities lead to the development of new

localized electronic states (E_D for donors and E_A for acceptors), often within the forbidden energy range between E_C and E_V (Fig. 1.12). These donors serve to create n- and p-type semiconductors, with the number of ionized donors and acceptors given by:

$$N_D^+ = \frac{N_D}{1+g_D e^{(E_F-E_D)/kT}} \quad 1.39$$

$$N_A^- = \frac{N_A}{1+g_A e^{(E_A-E_F)/kT}} \quad 1.40$$

where g_D and g_A are donor and acceptor site degeneracy factors. If the donors and acceptors are assumed to be completely ionized, we can write $n_o = N_D$ and $p_o = N_A$. This enables calculation of the Fermi energy for extrinsic n-type and p-type semiconductors to be found as:

$$E_F = E_i + kTln\frac{N_D}{n_i} \quad 1.41$$

$$E_F = E_i + kTln\frac{N_A}{n_i}\,. \quad 1.42$$

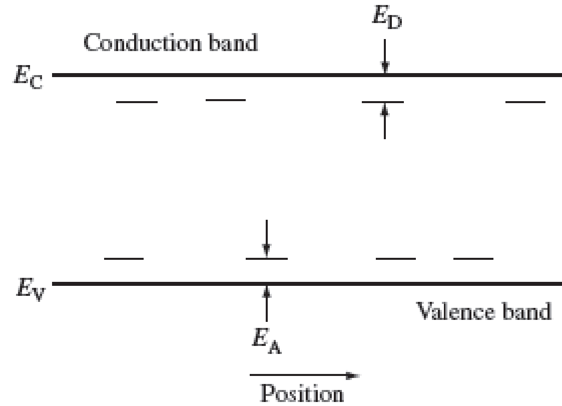

FIG. 1.12. Donor and acceptor levels in a semiconductor. The nonuniform spatial distribution of these states reinforces the concept that these are localized states. Figure from reference[35].

We will now turn our attention to the absorption of photons by direct and indirect bandgap photovoltaics. If the incident photon energy is greater than the bandgap energy, the absorption coefficient will be given by[37]:

$$\alpha(hv) \propto \sum P_{12} g_V(E_1)\, g_C(E_2) \qquad 1.43$$

where P_{12} is the probability of the transition of an electron from initial energy E_1 to final energy E_2 and the summation includes all possible transitions where $E_2 - E_1 = hv$. During photon absorption for a direct bandgap material, electron momentum and crystal momentum are preserved, and the equation above can be simplified to

$$\alpha(hv) \approx A^*(hv - E_g)^{1/2} \qquad 1.44$$

where A^* is a constant specific to the semiconductor. For an indirect bandgap semiconductor (such as Si), there exists a difference in crystal momentum between the valence-band maximum and conduction-band minimum. Lattice vibrations represented by phonons are absorbed and emitted during photon absorption and the resulting coefficients are given by:

$$\alpha_a(hv) = \frac{A(hv - E_G + E_{ph})^2}{e^{E_{ph}/kT} - 1} \qquad 1.45$$

$$\alpha_e(hv) = \frac{A(hv - E_G + E_{ph})^2}{1 - e^{-E_{ph}/kT}}\,. \qquad 1.46$$

With the sum providing the total absorption:

$$\alpha(hv) = \alpha_a(hv) + \alpha_e(hv). \qquad 1.47$$

Figure 1.13 plots the absorption coefficients as a function of photon energy for both Si (indirect bandgap) and GaAs (direct bandgap). For much of the photon energy range, the absorption coefficient for Si is noticeably lower. This is a result of its absorption process being dependent on the availability of phonons in addition to empty final electron states. This requirement causes light

to penetrate more deeply into indirect bandgap semiconductors and necessitates thicker solar cells for successful electron-hole pair generation. It should be noted that direct transitions in an indirect bandgap become possible (no phonon needed) at higher energies, as is shown above 3.3 eV for Si. The absorption coefficient relation calculated earlier can then be used to determine the rate of creation of electron-hole pairs (# of electron-hole pairs per cm^3 per second) as a function of position within the solar cell:

$$G(x) = (1-s)\int\big(1-r(\lambda)\big)f(\lambda)\alpha(\lambda)e^{-\alpha x}d\lambda \qquad 1.48$$

where s is the top grid-shadowing factor, $r(\lambda)$ is the reflectance, $\alpha(\lambda)$ is the absorption coefficient, $f(\lambda)$ is the incident photon flux, and the sunlight is incident at $x = 0$.

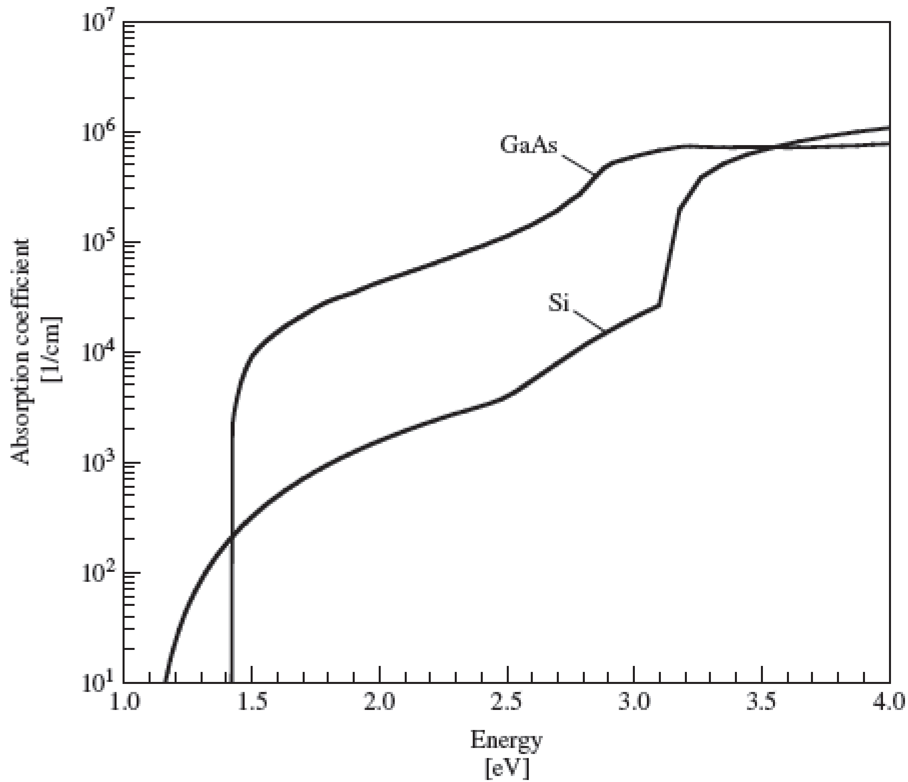

FIG. 1.13. Absorption coefficient as a function of photon energy for Si (indirect bandgap) and GaAs (direct bandgap) at 300 K. Their band gaps are 1.12 and 1.4 eV, respectively. Figure from reference[35].

When a solar cell leaves thermal equilibrium due to photon absorption, excited electrons tend to fall out of the conduction band and back to the valence band via a relaxation process. These electrons recombine with holes to eliminate free carriers and reduce current collection within the cell. In addition to surface recombination, there are several recombination mechanisms that take place within the cell, and three common ones will be briefly covered here. The first is known as Shockley-Read-Hall recombination (R_{SLT}) and is caused by traps due to defects. Electrons and holes recombine between the valence and conduction bands, resulting in the emission of a phonon. The second type is known as radiative or band-to-band recombination (R_{λ}) and results in energy transfer from an electron to a radiated photon (basis for operation of lasers and LEDs). The third type is termed Auger recombination (R_{Auger}). It parallels radiative recombination, but with the energy given to another carrier which in turn relaxes thermally by emitting phonons. These processes are outlined in Fig. 1.14 and their total recombination rate is given by[36]:

$$R = [\sum_{traps\ i} R_{SLT,i}] + R_{\lambda} + R_{Auger}\ . \qquad 1.49$$

The resultant minority-carrier lifetime at low-level injection can then be calculated by:

$$\frac{1}{\tau} = [\sum_{traps\ i} \frac{1}{\tau_{SLT,i}}] + \frac{1}{\tau_{\lambda}} + \frac{1}{\tau_{Auger}}\ . \qquad 1.50$$

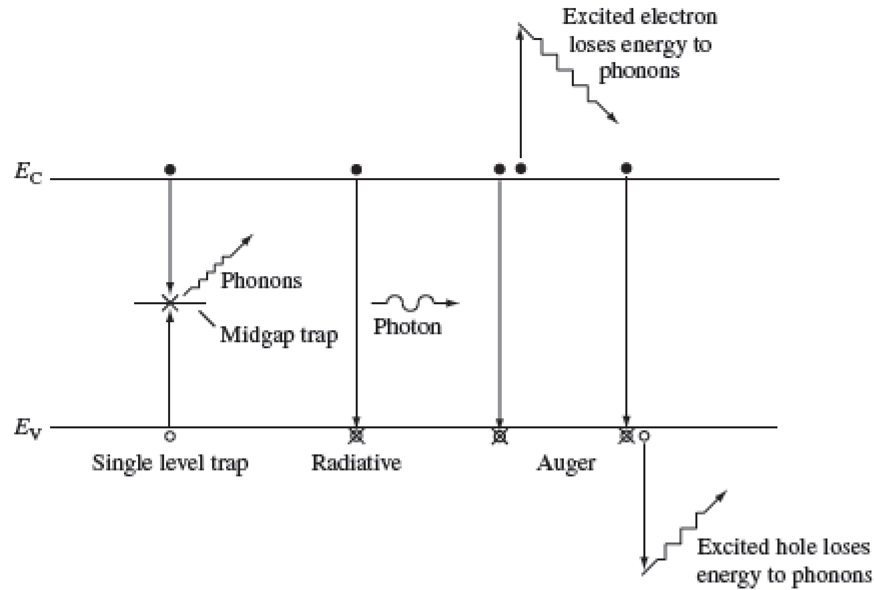

FIG. 1.14. Recombination processes in semiconductors. Figure from reference[35].

While many complicated variations now exist, the basic structure of a photovoltaic consists of a junction formed between p and n type material with front and back contacts for current collection[38-39]. Contact between the p and n region causes some electrons to drift to the p region while holes drift to the n region. Positively/negatively charged ions are left exposed in the n/p region creating an internal electric field that serves to naturally drive electrons/holes to the n/p region. A depletion region devoid of free charge arises at the junction as a result (Fig. 1.15). If photon absorption leads to the formation of free carriers within the depletion region, or within the minority carrier diffusion length from the edge of the depletion region, they become separated by the electric field and driven through a load via the electrical contact[40].

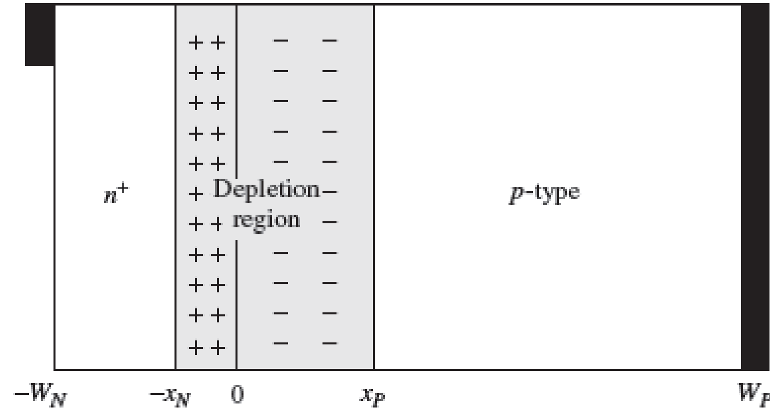

FIG. 1.15. Simple solar cell structure used to analyze operation. Free carriers have diffused across the junction (x=0) leaving a space-charge or depletion region practically devoid of any free or mobile charges. The fixed charges in the depletion region are due to ionized donors on the n-side and ionized acceptors on the p-side. Figure from reference[35].

The depletion width for the p-n junction with an externally applied voltage V can be found by:

$$W_D(V)=x_N+x_P=\sqrt{\frac{2\varepsilon}{q}\left(\frac{N_A+N_D}{N_A N_D}\right)(V_{bi}-V)} \qquad 1.51$$

$$V_{bi}=\frac{kT}{q}\ln\left[\frac{N_D N_A}{n_i^2}\right]. \qquad 1.52$$

We can now step back and examine a current–voltage (I-V) curve for a Si photovoltaic to understand how solar cell efficiency is determined experimentally. The rectangle in Fig. 1.16 is defined by the open circuit voltage (V_{OC}) and short circuit current (I_{SC}) and provides a means by which to define a maximum power point of the solar cell. The fill factor (FF) is, in turn, a measure of the squareness of the I-V curve and is given by:

$$FF=\frac{P_{MP}}{V_{OC}I_{SC}}. \qquad 1.53$$

The solar cell efficiency can then be determined by:

$$\eta = \frac{V_{OC} I_{SC} FF}{P} \quad 1.54$$

where P is the power of solar radiation incident.

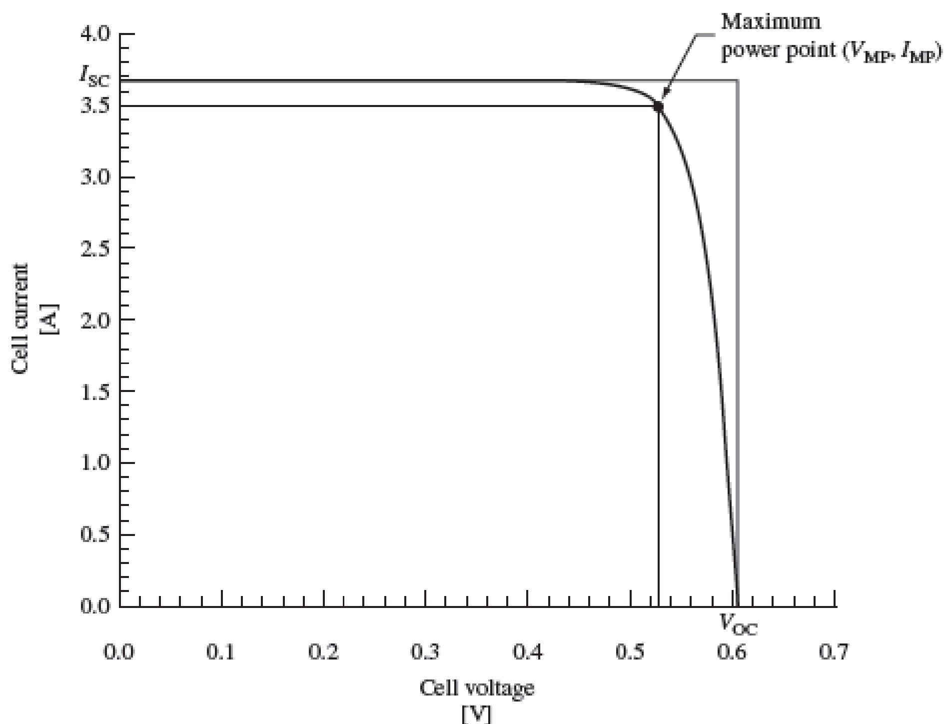

FIG. 1.16. Current-voltage characteristic of a Si solar cell. Figure from reference[35].

We will conclude this section with a brief review of several photovoltaic technologies pertinent to this research. Si is the first such material and has dominated the photovoltaic market since Chapin first demonstrated a 6 % efficient crystalline Si solar cell in 1954[33]. We will start by looking at crystalline Si, which requires high purity feedstock to create efficient cells. Over the last several decades, this has enabled the PV industry to largely rely on the microelectronics industry for supply[41]. The classic monocrystalline Si structure is shown in Fig. 1.17 where a p-type wafer has n-type phosphorous impurities diffused into it to create a p-n junction. Silver contacts are added to the top while an aluminum back contact completes the circuit and serves to reflect minority carriers

back towards the junction[42]. Lithography has replaced screen printing in the fabrication of the top contacts as part of an effort to decrease contact resistance and reduce shielding from the sun. Etching of the Si surface has been used to expose the <111> surface and increase the angle of light refraction into the absorber.

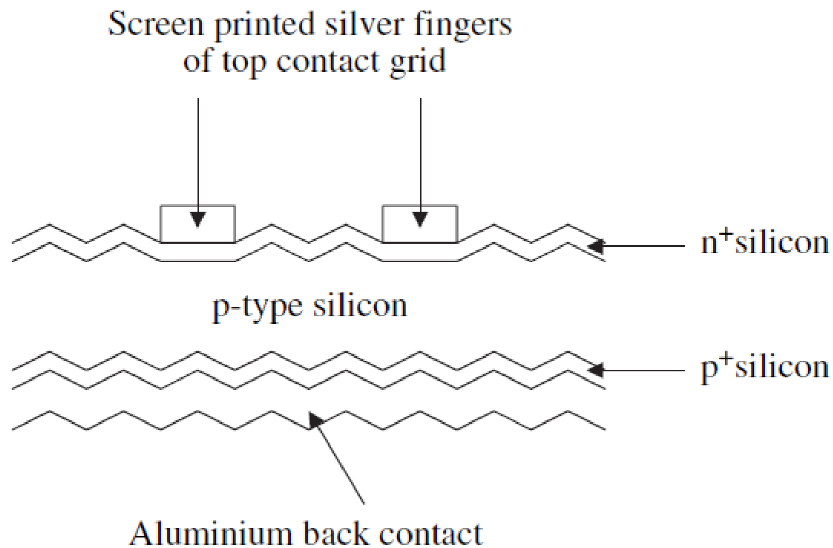

FIG. 1.17. Schematic cross-sectional view of a Si solar cell with screen printed contacts. Figure from reference[41].

III-V compounds have been developed as an alternative to Si photovoltaics for their potential as high efficiency, thin film solar devices. Unlike monocrystalline Si, III-V compounds are characterized by their direct bandgaps and subsequent high absorption coefficients[34]. In their pure, single crystalline forms, this is paired with high minority carrier lifetimes and mobilities, allowing successful diffusion to the depletion region. The market has largely been dominated by indium phosphide (InP) and gallium arsenide (GaAs) compounds with the latter a subject of testing with the NSMM reported here. InP and GaAs have close to optimal bandgap energies with values of 1.34 eV and 1.424 eV respectively. While progress was initially made using liquid phase epitaxy (LPE) and metalorganic chemical vapor deposition (MOCVD) techniques, increases in fabrication

costs have largely offset any monetary benefit of using a cheaper substrate. This has led to the push to develop multijunction devices[43-44]. The basic idea, also applied to chalcopyrite compound photovoltaics, is to optimize photon energy capture while minimizing loss in the form of heat to the crystal lattice. This can be accomplished by combining many bandgaps specifically tuned to the range of photon energies available. By stacking different junctions, from highest to lowest bandgap, a greater array of photons can be absorbed and the overall conversion energy increased. Fig. 1.18 outlines an example two-junction GaAs design which achieved 27.3 % efficiency[34]. Several design challenges must be overcome, including current matching from each junction, creating transparent interconnects, and bandgap engineering different chemical compounds to reduce interfacial stress and resultant defects. Due to their complexity, multijunction photovoltaic modules are not competitive with Si technologies under normal radiation intensities. However, their cost per watt can be lowered by 2 – 3 orders of magnitude using concentrator systems that provide the equivalent intensity of as much as 1000 suns of solar radiation with state of the art research efficiencies now reaching 44 %[45].

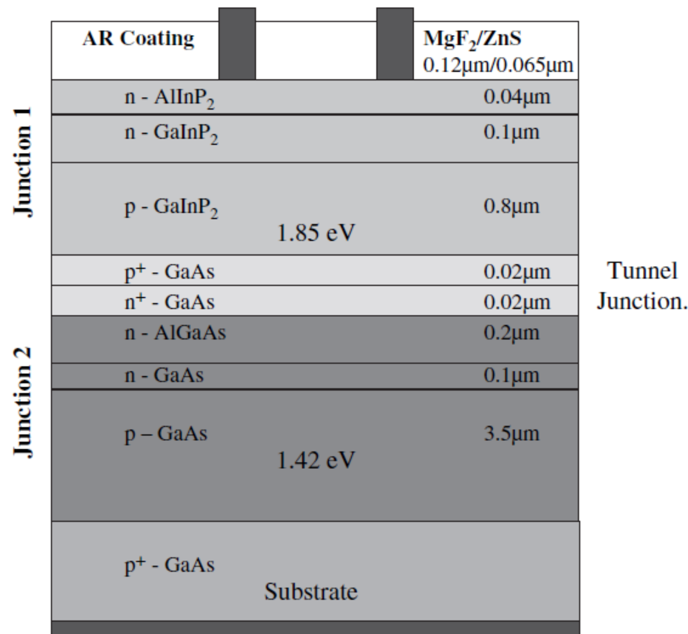

FIG. 1.18. Schematic cross-sectional view of the 27.3 % (AM1.5) monolithic $GaInP_2/GaAs$ tandem cell grown on a GaAs substrate. Figure from reference[34].

Chalcopyrites are a group of photovoltaic cells of particular interest to this research. These cells rely on I, III, and VI elements to form direct bandgap junctions with high absorption coefficients[34]. They are typically comprised of copper indium disulphide ($CuInS_2$), copper indium diselenide ($CuInSe_2$), and copper gallium indium diselenide ($CuGa_{1-x}In_xSe_2$). The latter, which has shown the most promise as a photovoltaic candidate, is commonly known as CIGS and is the material used in the 2-D scanning measurements shown in Section 2.6. In addition to improving its crystalline structure, Ga doping has helped tune the bandgap energy and enabled vertical grading of the bandgap through variable Ga concentrations in the absorber. The majority of CIGS samples exhibit a bandgap of 1.25 eV in an effort to balance photon absorption with the higher sample resistivity from Ga doping. Three different fabrication techniques have been used to create chalcopyrite samples: co-evaporation of elements, selenisation/sulphidisation of elemental precursor layers, and stacked elemental layer processing. The co-evaporation technique was first

used in 1981 to develop high efficiency $CuInSe_2$ cells and has recently been improved upon to create > 20 % efficient CIGS cells (and the CIGS cells presented in this work)[46-50]. A basic layout of a CIGS cell is given in Fig. 1.19[34]. As we will see in Section 2.6, CIGS performance is highly dependent on grain boundary passivation due to sodium and oxygen diffusion during the formation of the passivation layer[51].

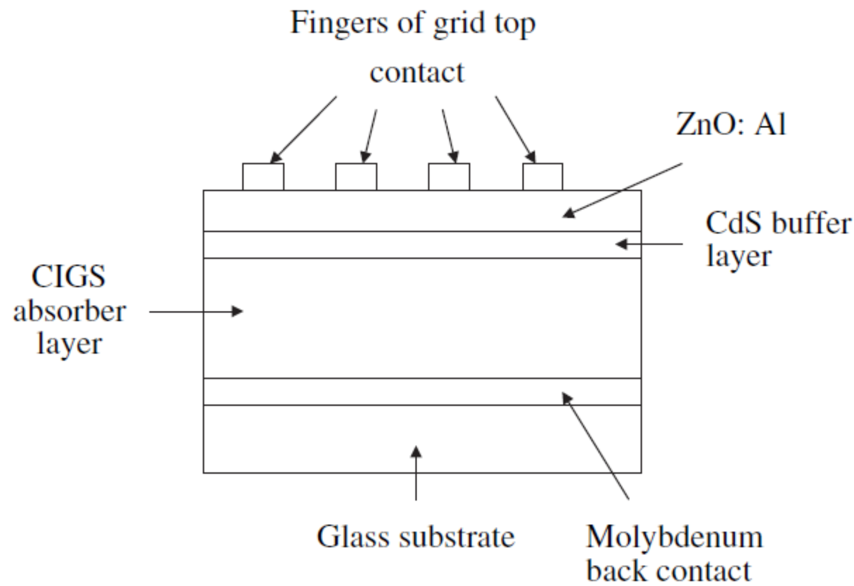

FIG. 1.19. Schematic cross-sectional view of a "substrate configuration" chalcopyrite device structure. Figure from reference[34].

Figure 1.20 provides a map containing state of the art research-cell efficiencies published by NREL. The term "research-cell" indicates that these devices are of small size (several cm) and have not been completed into a commercial module with this performance. Over recent decades, it is apparent that efficiency gains in traditional photovoltaic materials, such as Si, have largely leveled off. However, third generation photovoltaic materials such as multijunction GaAs continue to experience yearly efficiency progress.

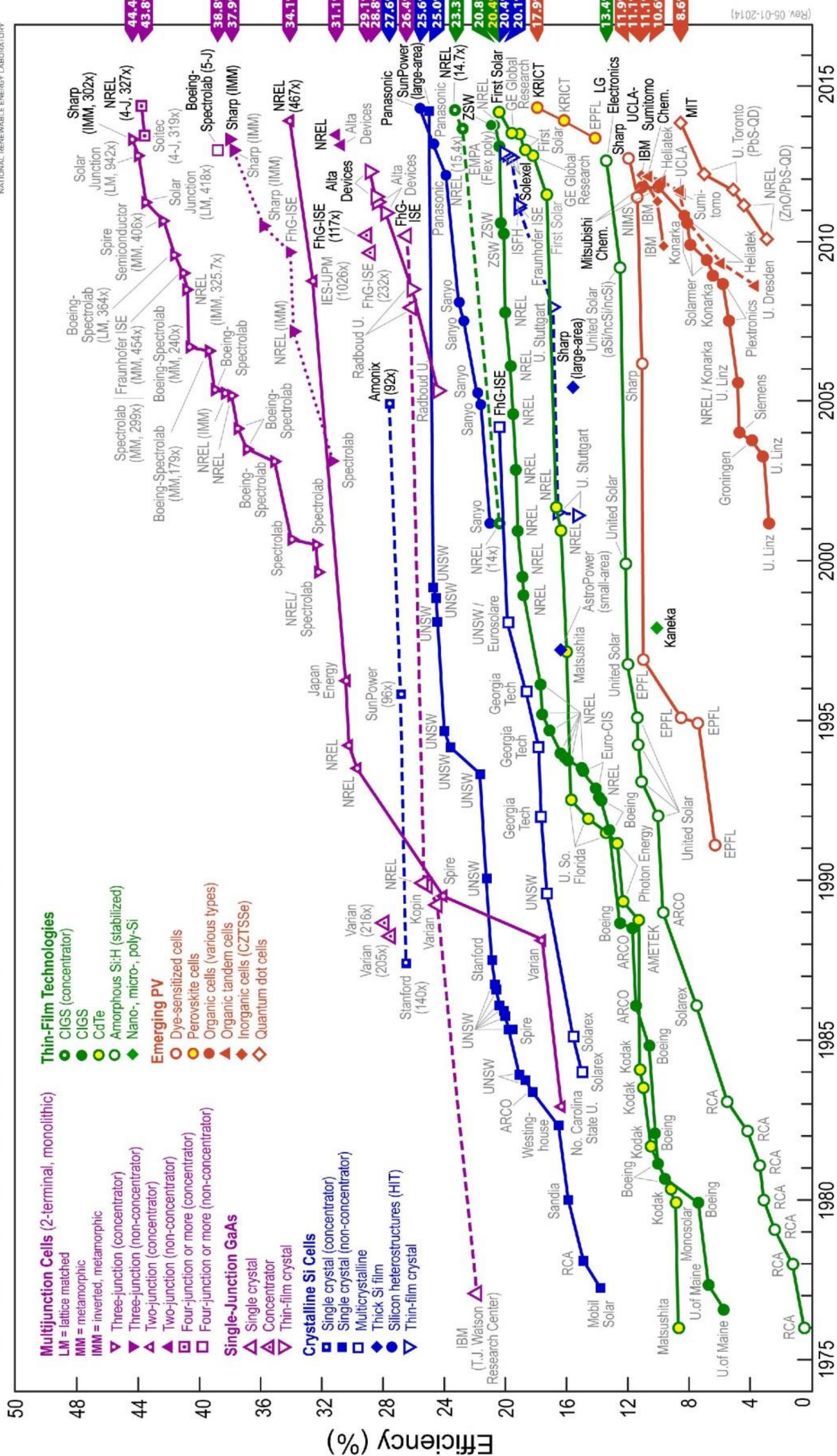

FIG. 1.20. Progress in research-cell efficiencies. Figure from reference[52].

1.3.4 Alternative Tools for Analyzing Photovoltaic Performance

Traditional photovoltaic analysis has relied on macroscale tools to study both carrier generation and carrier-lifetime. While important for quality monitoring in high throughput, industrial applications, these techniques have been adapted or replaced to facilitate measurement of the small scale physics important in understanding novel third generation photovoltaics. We will provide a brief overview here.

Light-beam-induced current (LBIC) relies on focused light to generate electron-hole pairs within the solar cell. It is nondestructive and capable of imaging solar cell arrays on the large scale or investigating features down to the micrometer scale (as determined by the far-field limit)[53]. Unlike electron beam scanning, which utilizes comparatively high energies, each photon from LBIC generates, at most, a single electron-hole pair. The internal field caused by the p-n junction within the cell produces a current in an external circuit that can be spatially tracked. However, each measurement point is made up of many carrier collection events and thus results attributed to individual defects can be difficult to interpret. LBIC remains a powerful tool in determining minority carrier diffusion length and recombination velocity as a function of illumination wavelength and intensity.

Photoconductive decay (PCD) is one of several techniques capable of determining minority carrier lifetimes and continues to be used extensively with single crystalline wafers and amorphous Si cells[54]. A short photon (light-emitting diode, tunable laser, broadband source) pulse with energy tuned to excite excess minority carriers deep in the semiconductor is used. The voltage across the solar cell is then monitored with an oscilloscope enabling tracking of its drop off proportional to the density of excess minority carriers as a function of time. Higher voltage levels indicate a longer decay time and subsequent increased carrier lifetimes within the solar cell.

A similar methodology relies on microwave absorption to determine carrier concentration[55-56]. A sample is irradiated with microwaves, but as opposed to NSMM, these are in the far field limit. At the same time, a tunable laser is used to excite excess minority carriers. The total microwave reflected power increases as a function of sample conductivity, and the resulting carrier lifetime can be evaluated. One limitation for this technique is in thin film photovoltaics, where surface recombination plays a significant role due to the large surface-to-volume of the material.

Photoluminescence (PL) decay (setup shown in Fig. 1.21) largely reverses the processes described for PCD, and can be used to study films too thin for microwave absorption[57-59]. A pulsed, tunable laser is used to excite a PL signal which is then radiated from the solar cell, collected with a separate lens, and focused onto the input slit of a spectrometer. A photomultiplier tube enhances the small signal attributed to emitted photons and enables useful detection. To record minority carrier lifetimes on the nanosecond range, a beam splitter and photodiode are used to sample a portion of the excitation laser. When the laser is pulsed, the electronics are triggered to enable a time-to-amplitude converter. This trigger is in turn disabled by the photon signal from the photomultiplier. This measurement is repeated for each laser pulse and allows a picture of carrier lifetime to form.

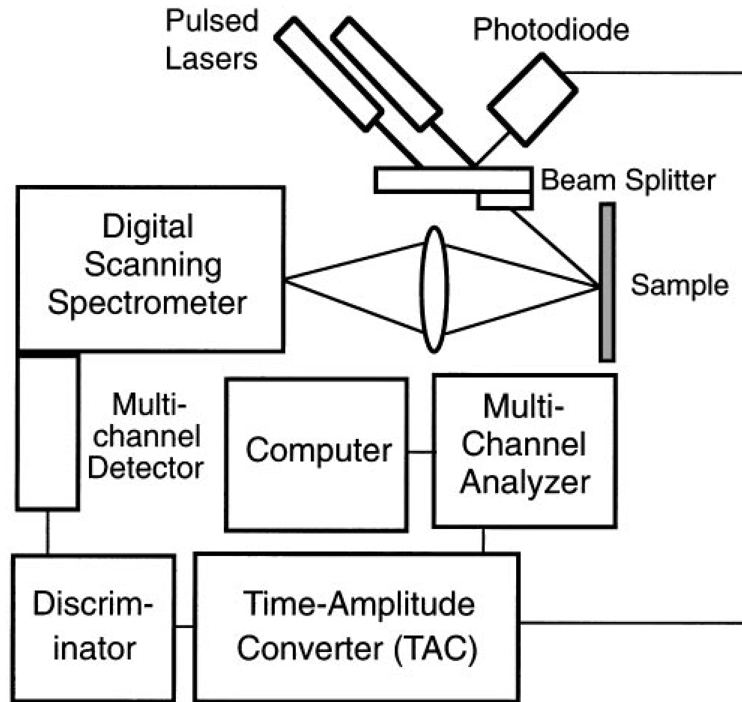

FIG. 1.21. Schematic representation of the photoluminescence decay method for determining minority-carrier lifetimes. Figure from reference[60].

To build on the previous technologies discussed, a wide range of advanced scanning probe microscopy techniques have been developed and enhanced over the last several decades to study various microscale material properties. With the rise of novel photovoltaic structures reliant on sub-micron scale engineering, they serve an important role in complimenting traditional measurement techniques. This section details a list of microscopes which have helped advance the photovoltaic field in addition to other new energy materials.

The STM was developed in 1981 to image conducting and semiconducting surfaces at an atomic level[15]. A bias voltage between the tip and sample allows electrons to tunnel through the separating vacuum. The resulting quantum mechanical tunnel current decays exponentially as a function of tip-sample height, enabling atomic scale imaging on suitable samples[61]. The magnitude of this resulting current is dependent upon the local density of states (LDOS) of the sample among other features, allowing detection of individual surface atoms. This ability has recently been used

to gain insight into the operation of several different photovoltaic structures. CIGS films are characterized by grains and corresponding boundaries that give rise to differing elemental compositions and defect densities. In traditional polycrystalline Si solar cells, these boundaries serve as recombination centers and thus reduce the overall efficiency of the cell. While the initial consensus was that a similar effect would be observed in CIGS, STM studies have shown a reduced DOS at the boundary compared to the grain surface[62]. These measurements indicate the presence of less recombination activity at the boundaries, opening up new paths towards the optimization of the CIGS structure.

The AFM was first developed in 1986 and has since become a powerful tool in the nano-scale world[63]. Its ability to image and manipulate materials with sub-nanometer resolution makes it ideal for analyzing the morphology of novel photovoltaics. The advent of conductive-atomic force microscopy (c-AFM) has expanded its usefulness and enabled simultaneous electrical characterization of materials. One such study on $CuInSe_2$ (CIS) and CIGS found that currents (both dark and illuminated) pass primarily through grain boundaries at low bias and primarily through grains at high bias[64]. The authors concluded that electrical and chemical gradients combine to create high carrier mobilities and electron-hole separation at the grain boundaries, leading to higher efficiencies. There has also been success in establishing an ohmic contact between the AFM tip and sample, resulting in quantitative measurements of charge carrier mobility with resolution on the order of 150 nm[65]. However, establishing an ohmic contact between a c-AFM tip and a photovoltaic surface (particularly an organic solar cell) can prove difficult. Furthermore, AFM feedback systems typically rely upon laser beam bounce off of the oscillating cantilever to maintain height control. As will be detailed in Sections 2.3 and 2.4, this design limits their inherent usefulness with photovoltaics and other light-sensitive materials.

Photoconductive-atomic force microscopy (pc-AFM), c-AFM with the presence of external illumination, provides material scientists with an additional means by which to visualize carrier

transport in photovoltaics. In CIGS, it has shown that a large electrical potential enables current to travel through both grains and their boundaries simultaneously, thus enhancing cell efficiency by overcoming band bending at the boundaries[64]. Additional studies on inorganic photovoltaics have successfully mapped out local photocurrents with 20 nm resolution in regions with no measurable topographical variation[66]. These photocurrents were found to vary between domains within the sample, suggesting that superior morphology control during device processing could improve operating efficiency. A final study focuses on processing conditions of polymer nanowire-based solar cells provides. The authors used pc-AFM in conjunction with c-AFM to study the dark and illuminated open circuit voltage and short circuit current density of samples after different deposition and drying times [67]. It was found that short drying times led to a higher voltage but sacrificed current density while longer drying times reversed this trend. By scanning a variety of nanowire densities due to varying processing times, an optimized nanowire cell could be developed.

Kelvin probe force microscopy (KPFM) is a noncontact variant of traditional AFM techniques that was developed in 1991[68]. A DC bias applied to the AFM cantilever functions as a reference electrode allowing the potential offset between the tip and sample under study to be measured. Rather than being mechanically driven at its resonant frequency by a piezoelectric motor, an AC voltage at a similar frequency is applied. The energy of the capacitor formed between the probe and sample by these combined AC and DC voltages causes the cantilever to oscillate. This oscillation is detected through traditional AFM feedback techniques while a nullifying voltage is used to minimize the resulting vibration. Recording this nullifying voltage as a function of position enables mapping of the work function and provides subsequent information on chemical potentials and energy levels across the sample. Many KPFM studies in the area of photovoltaics have focused on examining grain boundaries in inorganic solar cells. One group resolved grains with different crystallite orientations in CGS by tracking changes in work function with 50 nm

resolution[69]. Electrical activity in the CGS sample was induced via 675 nm light which was found to create an overall increase in work function until saturation at higher illumination intensities. A particularly enlightening study for CIGS fabrication focused on environmental conditions during passivation layer deposition[70]. When deposited in an oxygen rich environment, the cadmium sulfide (CdS) passivation layer did not diffuse into the main CIGS absorber layer (Fig. 1.22). This was blamed on the formation of an oxide layer at the interface, effectively capping the absorber grain boundaries. However, deposition of the CdS layer in a vacuum on a clean CIGS substrate led to diffusion of Cd and S deep into the CIGS grain boundaries. This effect enhances carrier collection by effectively creating a 3D p-n junction at the CIGS/CdS interface. These results were initially determined through changes in work function at grain interfaces via KPFM measurements and later verified through x-ray spectroscopy[71].

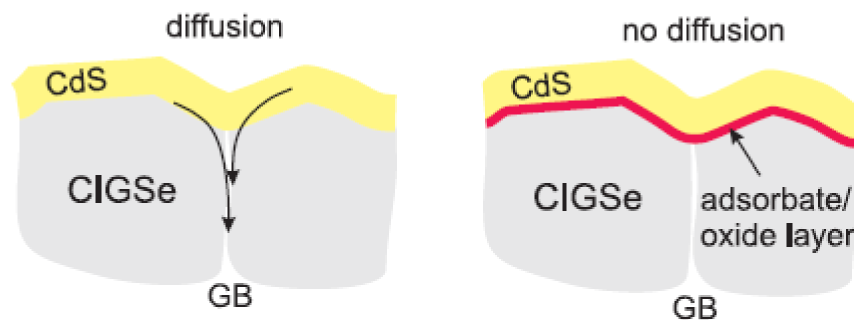

FIG. 1.22. Schematic representing the diffusion process along the grain boundaries for the clean (Se-decapped) and oxidized (air-exposed) CIGS surface. The diffusion process for the air-exposed surface is hampered by an oxide/adsorbate layer. Figure from reference[72].

A final AFM-based microscopy technique that is becoming important for understanding temporal electrical changes in photovoltaics is time-resolved electric force microscopy (tr-EFM). Traditional steady-state EFM uses a tip bias to draw local photogenerated charges in a sample near the tip and increase the tip-sample capacitance. This capacitance change is detected by a subsequent change in the cantilever oscillation frequency. This measurement can be moved into

the temporal regime by use of frequency-shift feedback whereby the charge buildup can now be time resolved on the order of 100 μs time scale[73]. In organic solar cells, this technique has been used correlate cell charging time with short circuit current to provide a new avenue for performance characterization. It has also helped illuminate degradation in organic solar cells due to charge trapping, one of the primary efficiency restrictions in this class of photovoltaics that has been poorly understood[74]. When compared to standard KPFM measurements, tr-EFM was found to identify local trap formation with much greater sensitivity and correlate more closely to measured device quantum efficiency. Recent work in the field of tr-EFM has continued to push the state of the art by studying perturbation of feedback-free cantilever oscillation, enabling time-resolved measurements down to 100 ns[75].

NSOM draws many parallels to NSMM in that it exploits evanescent waves to break the far field resolution limit that hinders traditional optical microscopes. As with NSMM, the important operating principle is that the microscope's design, both in terms of its probe diameter and sample/probe distance, is much smaller than the wavelength of illumination. Light is typically carried to the sample by either focusing through a hollow tip in an AFM probe (Fig. 1.23) or through the use of nano-scale fiber optic cables. As this technology has developed, it has found a variety of uses in the photovoltaic field. In regards to CIGS, NSOM has been used to map out local bandgaps on lateral scales approaching 200 nm, below the illumination wavelength of 632.8 nm[76]. These variations in bandgap were derived from photoluminescence images and could be correlated to fluctuations in absorber thickness across the cell. Time resolved NSOM has also been used to study polymer-blend solar cells to track the cause of efficiency variations across different compositions[77]. The authors were able to image fluorescence decay lifetime and subsequently calculate charge-carrier generation. Uniformity of charge-carrier generation across cells with varying efficiencies indicated that carrier extraction, rather than generation, what the limiting factor in device performance. While NSOM has proved to be a powerful technique and continues to be

improved upon, it remains limited by costly, complicated tip design which is easily damaged by any sample contact during scanning. Apertureless scanning which utilizes a more traditional AFM tip continues to be developed and may help solve these shortcomings.

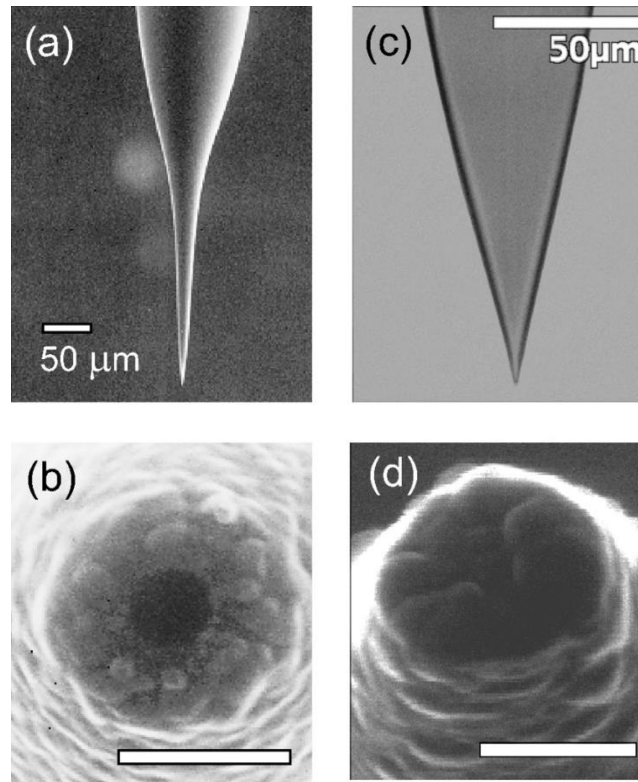

FIG. 1.23. Aluminum-coated aperture probes prepared by pulling (a), (b) and etching (c), (d): (a), (c) macroscopic shape, SEM and optical image. (b), (d) SEM close-up of the aperture region, scale bar corresponds to 300 nm. Figure from reference[78].

Chapter 2

Near-Field Scanning Microwave Microscopy Measurements on Photovoltaics

CONTENTS

2.1 Overview 49

2.2 NSMM Application to Photovoltaics from Literature 50

2.3 Design and Layout of NSMM 56

2.4 NSMM Redesign 61

2.5 Height Profile Measurements 67

2.6 Imaging of Photovoltaics 77

2.7 Modeling the NSMM 85

2.1 Overview

In this chapter, we discuss the design of our NSMM and its application towards measuring a variety of photovoltaic materials, including Si, GaAs, and CIGS. The dark-state capable feedback system implemented here is a modification of an existing tuning fork setup from the literature. By further improving upon the microwave circuitry, we report on nanoscale imaging of multilayer, inhomogeneous photovoltaics. In addition, by measuring changes in microwave frequency as the sample was pulled away from the tip at a single point, we were able to extract the carrier concentration of solar cells.

2.2 NSMM Application to Photovoltaics from Literature

In Section 1.3.1, we covered the historical development of near-field scanning microwave microscopy from initial theory to a range of experimental verifications. In Section 1.3.3, we reviewed a range of photovoltaic materials seeking to provide a high efficiency, renewable energy source for both industrial and consumer applications. The expansion of increasing complexity in the solar cell market has been closely followed by a host of new microscopy techniques (Section 1.3.4) capable of both performing bench line efficiency measurements and revealing how parameters such as fabrication conditions and doping levels lead to changes in defect concentration and carrier recombination. With its inherent ability to detect changes in local capacitance of semiconductors with high resolution, it may be somewhat surprising that little prior work exists in the literature applying NSMM techniques to photovoltaics. In fact, previous studies can be largely credited to one group from South Korea that has used their system to investigate illumination changes on Si samples[11-12]. We will cover their work in more detail here.

Their NSMM relies on a high resolution $\lambda/4$ coaxial resonator with a tunable resonance cavity to achieve high reflection coefficient S_{11} sensitivity (see Fig. 2.1). A stainless steel wire with diameter of 50 μm and tip radius between 1 – 5 μm was used for the tip. The tip was connected directly to a coupling loop in the dielectric resonator, allowing microwave signal interaction with the sample. Unlike AFM based NSMM systems which require laser illumination for optical feedback, this microscope relied on a tuning fork feedback system, allowing operation in the dark state[19, 79]. This is a beneficial step when studying photovoltaics as it allows electrical characterization in both illuminated and truly dark conditions. Shear force distance control was demonstrated in both air (for studying photovoltaic samples) and water (for studying biological samples). Unmounted, the tuning fork has a resonant frequency at 32.758 kHz with a Q of 3639. When glued vertically to the NSMM tip, the increased mass of the mechanical resonating system

decreased the resonant frequency to 32.358 kHz and the Q to 514. With an AC voltage modulating the attached tuning fork, height control connected to a piezoelectric stage enabled distance control down to 10 nm. We will present an improved glue-free tuning fork setup developed for our NSMM in Section 2.4.

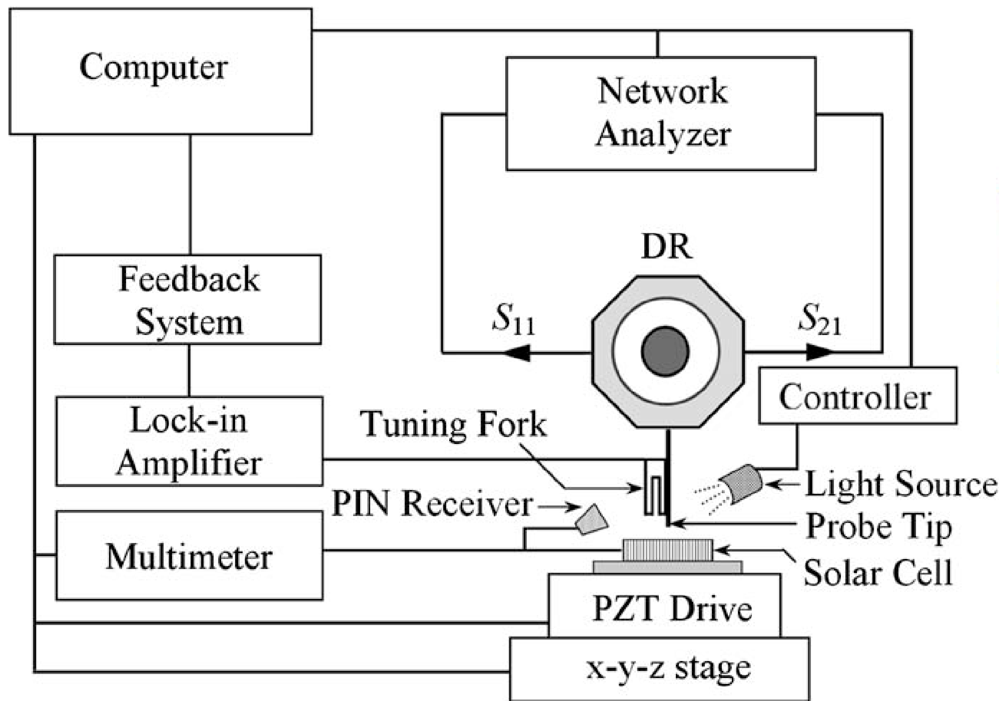

FIG. 2.1. Experimental setup of the NSMM system. Figure from reference[11].

Measurements were conducted on a Si photovoltaic consisting of a p-n junction, a TiO_2 layer on the top antireflective coating, and a back Al contact layer (Fig. 2.2). The cell was finished with 0.1 mm thick Ag electrodes over the TiO_2 layer. Transmission line theory was used to analytically model tip/sample interaction as a result of various illumination conditions. High sensitivity required impedance matching via a tuning screw controlling the position of a dielectric resonator inside the cavity. The microscope and sample system was described as two impedance matched

(mismatched under illumination) microwave lines: Z_0 for the probe line and Z_{in} for the solar cell line. The microwave reflection coefficient S_{11} was then determined by:

$$S_{11} = 20log\left|\frac{Z_{SC}^R - Z_0}{Z_{SC}^R + Z_0}\right| \quad 2.1$$

where Z_0 is the probe tip impedance and is defined as 50 Ω and Z_{SC}^R is the real part of the solar cell impedance. The full complex impedance of the Si solar cell was then defined as:

$$Z_{SC} = Z_n \frac{Z_{sub} + jZ_n K_n t_n}{Z_n + jZ_{sub} K_n t_n} \quad 2.2$$

where Z_n, k_n, and t_n are the impedance, wave vector, and thickness of the n-type Si layer. The p-type Si and Al layers could be characterized as a single, semi-infinite substrate as their electrical properties are independent of illumination intensity and the Al thickness being much greater than skin depth at measurement frequency (4.1 GHz). The complex impedance of this substrate could then be estimated as:

$$Z_{sub} \cong jZ_a k_a t_p \quad 2.3$$

where Z_a is the impedance of air (377 Ω), k_a is the wave vector of air (87 m^{-1} at 4.1 GHz), and t_p is the thickness of the p-type Si. The solar cell complex impedance can now be expanded as:

$$Z_{SC} = Z_a^2 k_a^2 t_p^2 t_n \sigma_n + jZ_a k_a t_p \quad 2.4$$

where σ_n is n-type Si photoconductivity defined by:

$$\sigma_n = (\eta q_e \mu_n \times \frac{\tau_n}{t_n})(\frac{I}{hv}) \quad 2.5$$

where η is the solar cell quantum efficiency (17 %), q_e is the charge on an electron, τ_n is the carrier lifetime (2.5 X 10^{-3} s), μ_n is the carrier mobility (1500 cm^2/V s), I is the illumination

intensity, and $h\nu$ is the photon energy. The above theory predicts an increase in S_{11} as illumination intensity and wavelength increase due to an increase in photoconductivity.

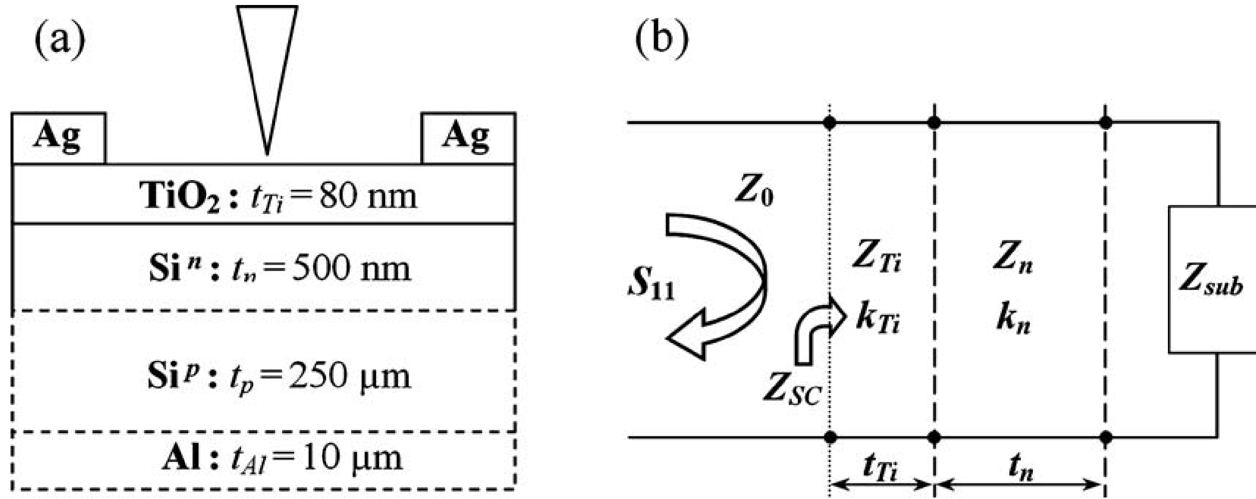

FIG. 2.2. (a) Schematic structure and (b) equivalent model of the probe tip-solar cell system. Figure from reference[11].

Four different LEDs were set up 2 cm away at each corner of the solar cell. They had wavelengths of 625 nm, 590 nm, 526 nm, and 460 nm, allowing the authors to track S_{11} sensitivity to wavelength as well as light intensity. As predicted, increased light intensity led to a greater impedance mismatch and subsequently larger shift in S_{11} (Fig. 2.3). Images were normalized against the Ag traces which are independent of illumination conditions. Full wave Ansoft simulations were also conducted showing that increased carrier concentration, due to photoconductivity, decreased the electromagnetic field in the solar cell while subsequently increasing it in the air. This mirrored the experimental impedance mismatch seen. For this Si solar cell, conversion efficiency was found to be highest at the 526 nm wavelength, leading to the largest shift in S_{11} (Fig. 2.4). This work provides an important foundation for our research both as an experimental validation of the NSMM's ability to track microwave reflection coefficient changes due to photoconductivity in a solar cell and as a precursor to feedback control in a truly dark state.

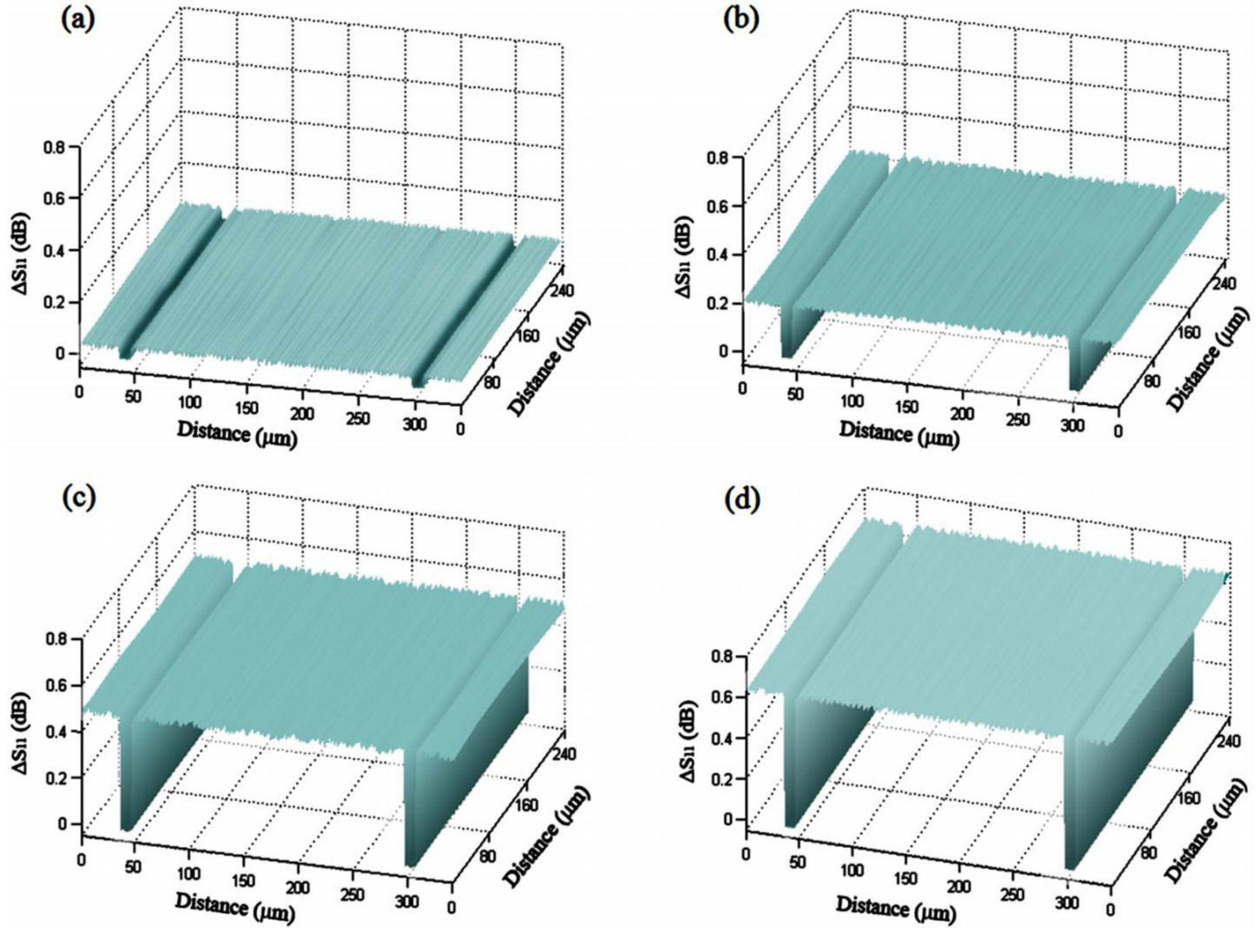

FIG. 2.3. 3D NSMM images of microwave reflection coefficient changes of solar cells dependence on the incident white light intensities with the scan area of 340 x 240 μm^2 at 4.1 GHz. Here $\Delta S_{11} = S_{11}^{i} - S_{11}^{0}$, where S_{11}^{0} is the reflection coefficient for dark condition and $i = 1,2,3,4$ indicates the incident light intensities at (a) 122 mW cm^{-2}, (b) 146 mW cm^{-2} (c) 163 mW cm^{-2}, and (d) 166 mW cm^{-2}. Figure from reference[11].

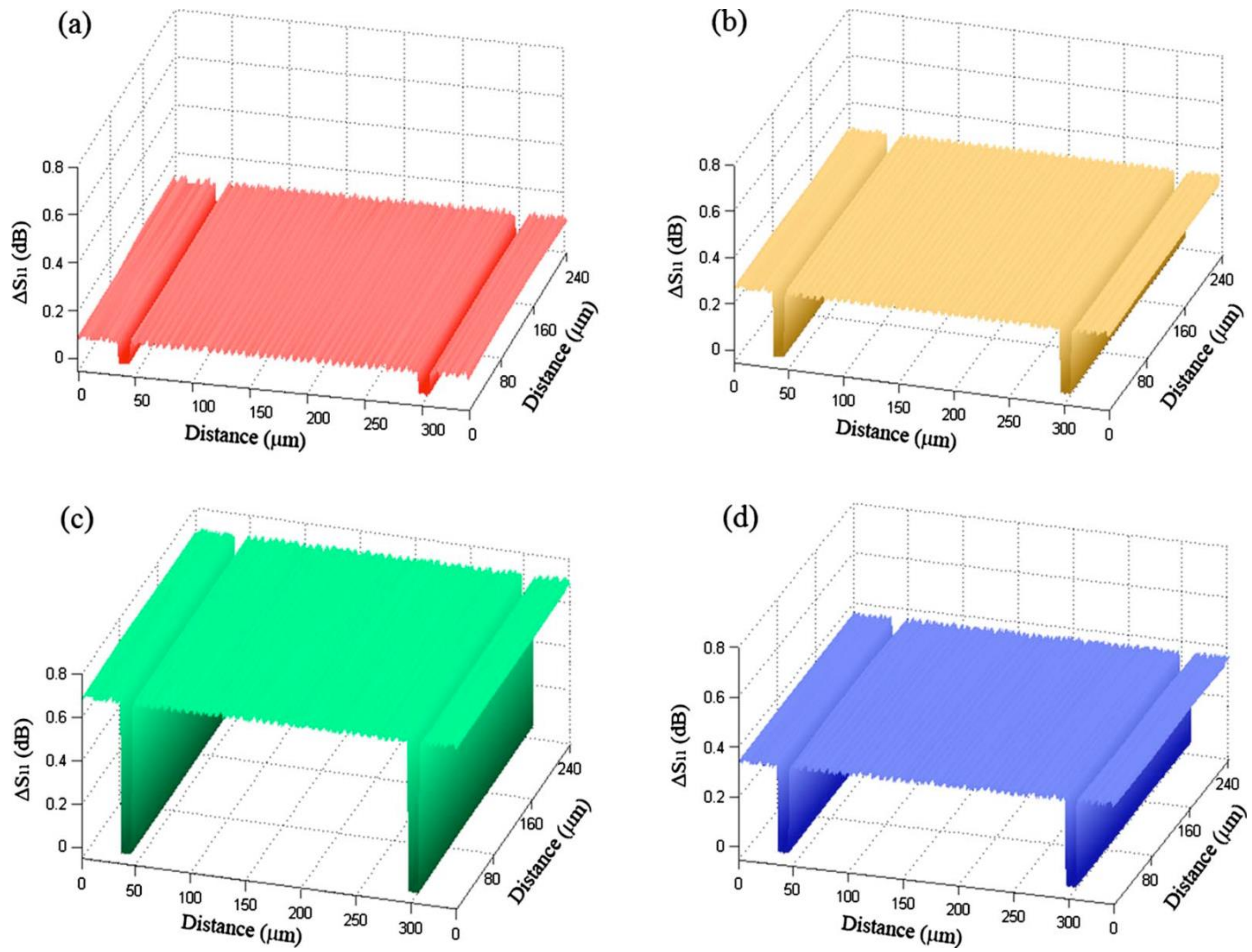

FIG. 2.4. 3D NSMM images of microwave reflection coefficient changes of solar cells dependence on the incident light wavelengths with the scan are of 340 x 240 μm^2 at 4.1 GHz. Here $\Delta S_{11} = S_{11}^{i} - S_{11}^{0}$, where S_{11}^{0} is the reflection coefficient for dark condition and $i = 1,2,3,4$ indicates the incident light wavelengths at (a) 625 (red), (b) 590 (yellow), (c) 526 (green), and (d) 460 nm (blue). Figure from reference[11].

2.3 Design and Layout of NSMM

When I began my work at NIST, the first inception of the NSMM, similar in design to that presented in Atif Imtiaz's thesis, had been completed and was being used to take height measurements on various semiconducting and conducting samples[26]. We will investigate these early measurements in Section 2.5 after detailing the initial NSMM design, as well as the improvements we have made to enable high resolution 2-D scanning. Figure 2.5 shows the original radio frequency (RF) circuit with an enlarged view of the tip-sample interaction. The RF circuit begins and ends with the Anritsu 37397C vector network analyzer (VNA) which is used to both source and analyze the microwave signal. The VNA is connected to a three-port circulator which links the phase matching circuit to the NSMM tip. The circulator is a nonreciprocal device utilizing a biasing static magnetic field to direct RF energy, without major loss, from port 1 → port 2, port 2 → port 3, and port 3 → port 1. The circulator used in the experiment has a bandwidth of 2.3 – 7.5 GHz, limiting the microwave signal available for measurement. A phase shifter (bandwidth: 1 GHz – 5 GHz) and mechanical tuning circuit are connected to another port on the circulator. They serve to adjust the length of the transmission line and tune the RF resonance frequency under study, thereby enhancing sensitivity to impedance and capacitance changes. The final port of the circulator is connected to the NSMM tip and its coaxial housing, and the signal from this port represents the measured properties of the material. The mechanically cut Pt-Ir tip used for measurements is 3 mm long with a diameter of 0.2 mm and a tip radius of 100 nm (Fig. 2.6). The tip is first formed by shearing the end of a Pt-Ir wire with wire cutters. It is then inserted into a copper tube of matching inner diameter, effectively replacing the center conductor of a coaxial cable (Fig. 2.7). This inner copper tube is housed within the Teflon dielectric of the coaxial cable, which is in turn encased in the outer copper conductor (inner diameter of 1.6 mm and outer diameter of 2.2 mm). This configuration creates a tip socket that enables convenient tip replacement. This coaxial housing connects to a bias tee (bandwidth: < 26 GHz) that separates AC

and DC signals. The bias tee contains two pathways with a capacitor in one and an inductor in the other. The capacitor serves to block DC voltage, allowing only RF signal to return to the circulator and then to VNA for detection. The inductor serves to block AC voltage, allowing DC tunneling current between the tip and sample to be detected by a pre-amplifier and read out with a lock-in amplifier. A bias voltage (typically 2 V) is applied to the sample and current is on the order of nA. Even though the VNA encompasses a range of 40 MHz – 65 GHz, the original RF circuitry limited studying samples in the significantly narrower 2.3 – 5 GHz bandwidth.

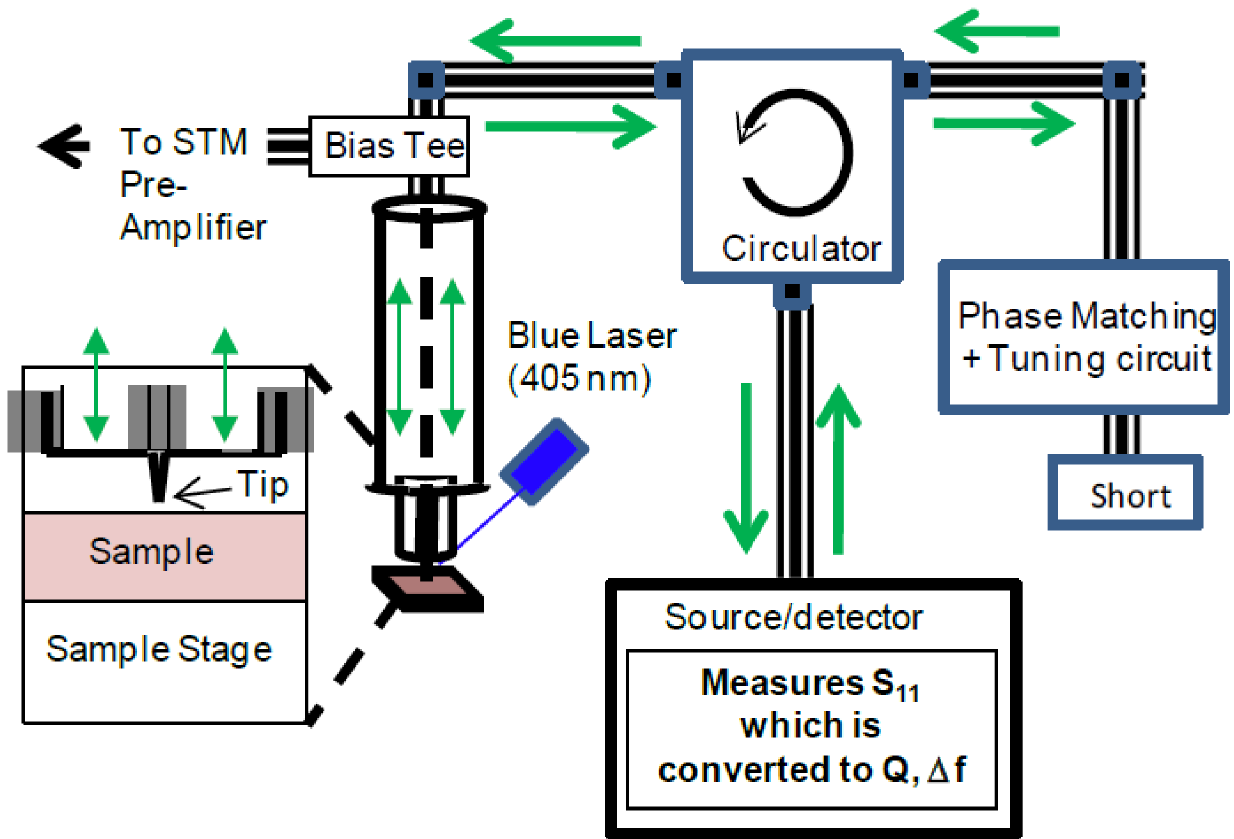

FIG. 2.5. Schematic of the NSMM system. Green arrows indicate microwave power flow.

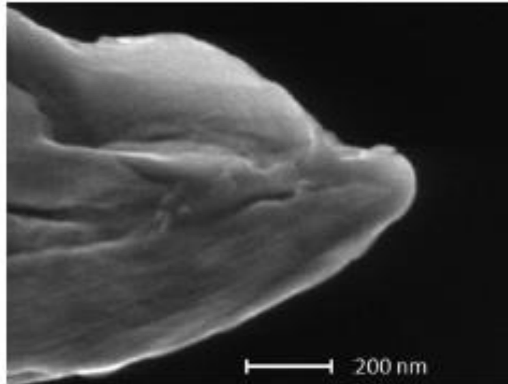

FIG. 2.6. SEM image of mechanically cut, Pt-Ir tip with radius roughly 100 nm.

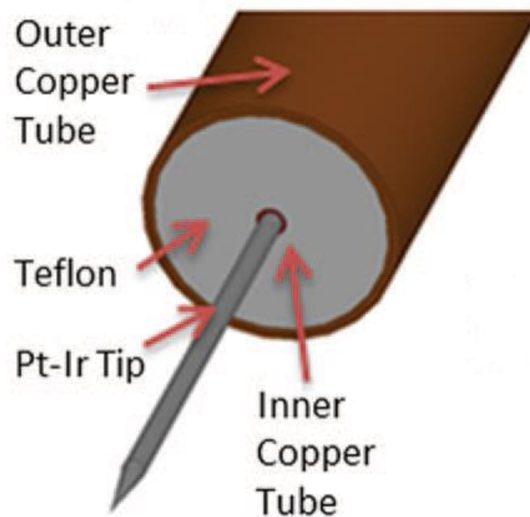

FIG. 2.7. Schematic of probe tip construction with cut Pt-Ir tip inserted into a coaxial cable.

The tip motion is controlled with two different motors for coarse and precision tip-sample approach. A Thorlabs DC servo motor with 12 mm range drove the tip assembly near the sample under study while coarse position was viewed using a magnified video feed. At this point, the approach process consisted of monitoring the DC tunneling current while a piezoelectric-tube with

4 μm range moved the tip closer in 10 nm increments. Measurement-ready position was achieved when DC current was established. Using software written by Thomas M. Wallis, this DC current also served as height feedback through minute adjustments to the piezoelectric-tube position. The sample was mounted onto a closed-loop nPoint C.300 DSP Controller x-y stage with 100 μm range and 2 nm resolution in each direction. For illumination of photovoltaic samples, a continuous wave, broad-area diode-laser light source at wavelength 405 nm and approximate intensity of 0.160 W cm^{-2} was mounted 5 cm from the sample. The sample, tip housing, diode-laser, and positional stages were all mounted on an active pneumatic isolation table, while the isolation table and pre-amplifier were housed within a dark box.

Initial work with this system focused on demonstrating sensitivity to photoconductivity changes as well as height measurements on different samples. These will be covered in more detail in Section 2.5. The primary goal of this NSMM was to enable 2-D imaging of complex photovoltaic samples akin to those recorded on Si by Kim, et al. The results in Fig. 2.8 demonstrate the earliest attempt at achieving this goal on a high efficiency CIGS sample from NREL. Due to the DC current's limited ability to maintain feedback on a semiconducting sample with large spatial variations, we were forced to suspend feedback during the measurement. Furthermore, a relatively small 1 x 1 μm^2 sample area was scanned in an effort to limit imaging time (~1 hr). Because CIGS grains are often on the order of 1 μm, these image dimensions are clearly insufficient to properly elucidate material changes under illumination. However, even with the above limitations, an overall shift in the reflection coefficient S_{11} amplitude was recorded. Images on the right show the same data with expanded color scales (note the range difference) to help bring out any spatial variations. While the dark image showed clear tip drift and/or sample tilt as a function of position, the illuminated image provides possible features on the order of a CIGS grain. Although promising, the NSMM required several important upgrades to improve image resolution.

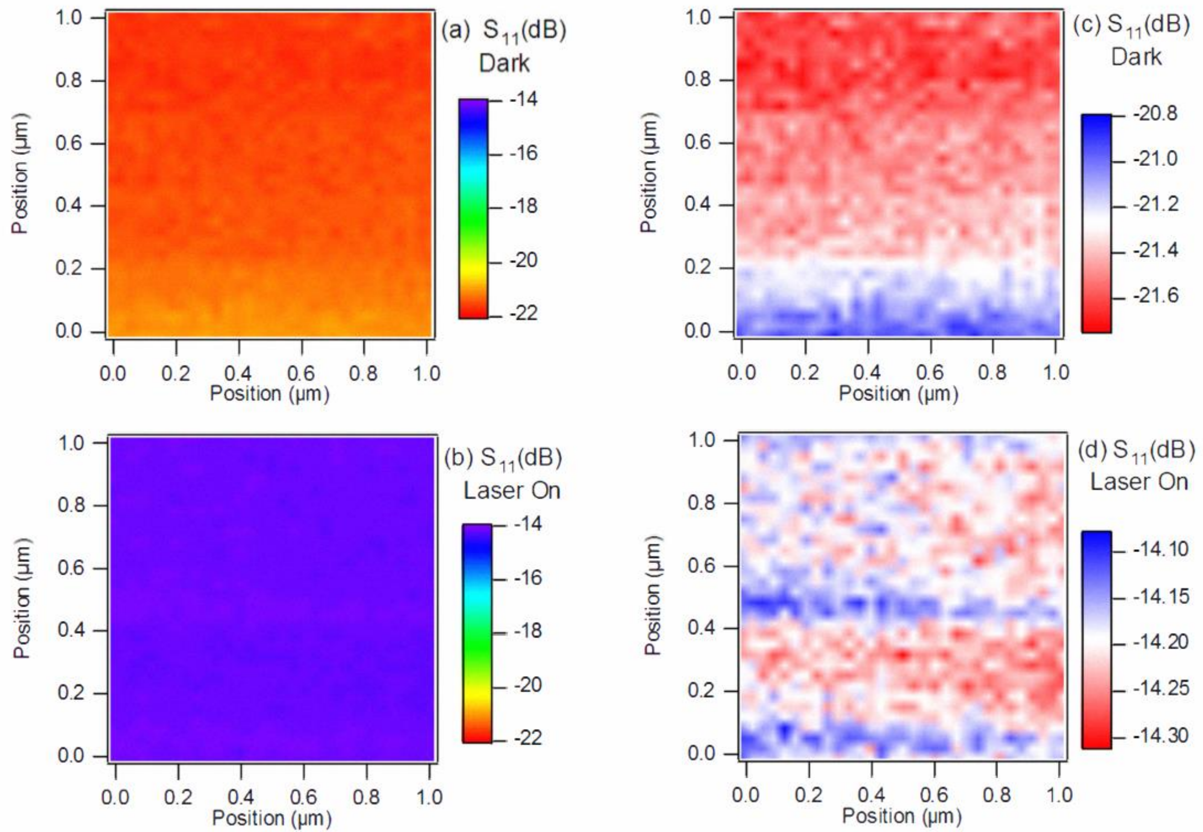

FIG. 2.8. S_{11} two-dimensional scan for sample CS99. (a) and (b) show the large change in absolute value of S_{11} by plotting data on the same color scale for the dark (a) and the illuminated (b). (c) and (d) show the same data with expanded color scales (note range difference) to bring out fine structure. Fine structure under illumination (d) is similar in size to that of the grain structure observed from AFM scans.

2.4 NSMM Redesign

The modifications on the NSMM can be broken down into three main sections: RF circuitry and noise dampening, feedback system, and laser illumination and safety. As we have seen in the preceding section, our accessible range of microwave frequency for testing was severely limited due to bandwidth restrictions on both the circulator and phase shifter. This first problem was solved by removing the mechanical tuner, allowing the phase shifter to directly connect the VNA to the coaxial with embedded Pt-Ir tip. This expanded the lower frequency range down to 1 GHz and enabled the measurements in the 2 GHz range which are reported in Section 2.6. Recently, a new phase shifter was added that expanded the upper range to 20 GHz, opening the possibility for frequency dependent tuning to various doping levels as was recently reported in Si calibration samples[80]. To further reduce mechanical vibrations negatively affecting stability of both the RF circuit as well as the height feedback system, the black box was floated on an optical table. The phase shifter was also moved inside the black box to minimize disturbances due to air currents. Meanwhile, the arm holding the tip assembling and coarse alignment was rebuilt to increase its overall stiffness and reduce susceptibility to mechanical vibrations not fully damped by the optical table or active anti-vibration table. With the mechanical tuner removed, overall improvements in microwave reflection coefficient S_{11} stability enabled frequency response to be tuned down to -78 dBm. Figure 2.9 shows the effect of phase shifter tuning with a 2.3° change resulting in a 20 dBm increase in $|S_{11}|$.

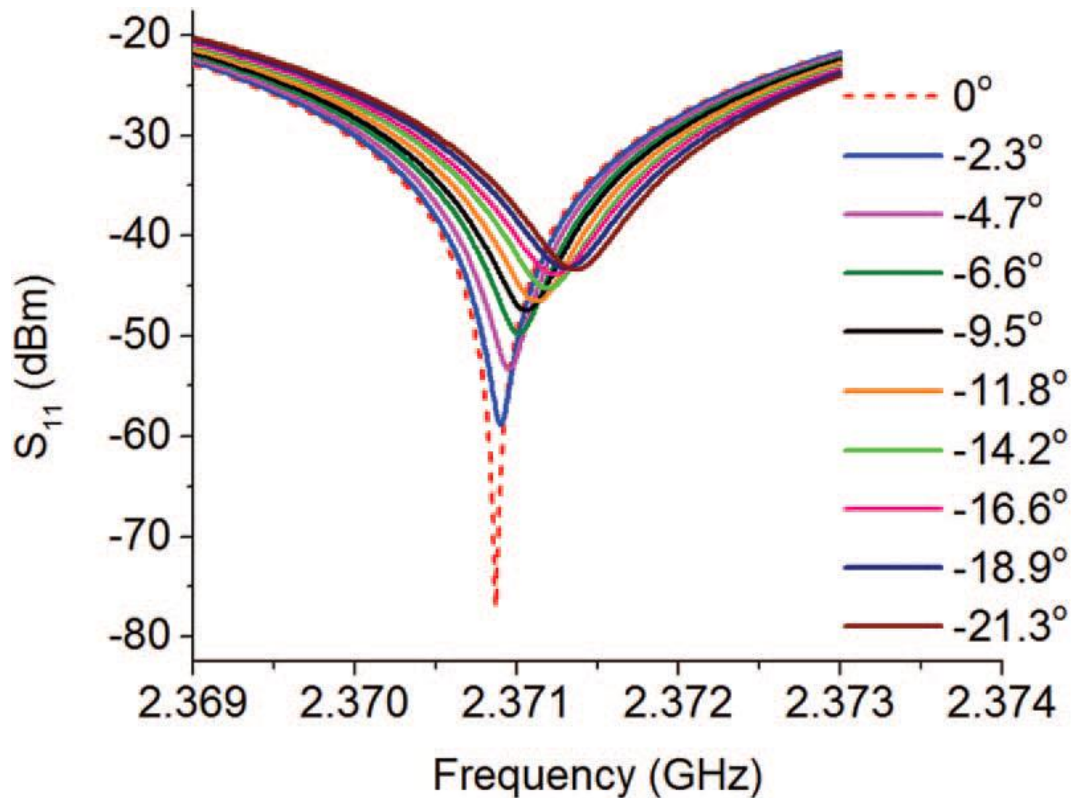

FIG. 2.9. Typical reflection frequency response with minimum tuned to -78 dBm and a normalized phase shifter setting of 0° is shown by a dashed line (sharpest dip). Small variations in the phase shifter highlight sensitivity of $|S_{11}|$ to the microwave phase-tuning circuit.

The DC current feedback system provided an early method of height control but was ultimately limiting in several key ways. First, it used a piezoelectric tube attached to the tip to provide height response with a maximum 4 μm range. Due to the high sensitivity of RF frequency sweeps to coaxial cable tension, even a small shift of several μm by the tip created artifacts in the RF signal. This also limited height variations to 2 μm in either direction during scanning, restricting study to relatively smooth samples with limited topographical variation. Second, the design was based on the STM feedback that typically requires high vacuum, low temperature environments for optimal tunneling between tip and sample. Ambient conditions greatly restricted tunneling sensitivity, particularly on semiconducting materials, and thus made it difficult if not impossible to maintain feedback for the long time periods necessitated by high resolution imaging. Finally, DC feedback

prevents studying samples with insulating surface layers. While this is not typically an issue in the field of photovoltaics due to the presence of a front-side conductive contact, it can become a problem with the presence of thick oxide layers or other compositions that impede carrier movement.

To resolve these issues, we implemented a tuning fork feedback system for precise height control. A custom Rexolite holder (Fig. 2.10) was used to clamp the quartz tuning fork perpendicularly against the tip, while a thin insulating layer of glue prevents the fork's driving signal from interfering with the NSMM's DC readout. A set screw provided incremental control of contact torque between the tip and the tuning fork. By avoiding the traditional method of gluing the tuning fork to the probe tip, we can replace tips without replacing or modifying the tuning fork and maintain a higher Q during feedback[79, 81]. Fig. 2.11 shows the mechanical frequency response of the tuning fork both in and out of contact with the NSMM tip. In contact, the tuning fork has a resonance frequency of 32.16 KHz, with Q = 1000 (shown in solid in Fig. 2.11). The free, undamped tuning fork yields an expected higher resonance frequency of 32.58 kHz with a Q > 2000 (shown in dashed in Fig. 3.7)[82]. The commercial tuning fork feedback controller requires a Q near 1000 for phase-locked loop operation and feedback control. Fig. 2.12 shows the effect of the tuning fork on the microwave circuit by examining the S_{11} response with the tuning fork in and out of contact with the tip. The S_{11} frequency response was initially tuned by use of the phase-matching circuit with the fork in contact with the tip (shown in solid in Fig. 2.12). Upon removal of the tuning fork from contact, the load seen by the microwave circuit changed, resulting in an increase in the S_{11} amplitude of 29 dBm, and a shift of the minimum by 0.35 MHz (shown in dashed in Fig. 2.12). This measurement illustrates the importance of tuning the S_{11} frequency response under measurement conditions, in order to optimize sensitivity.

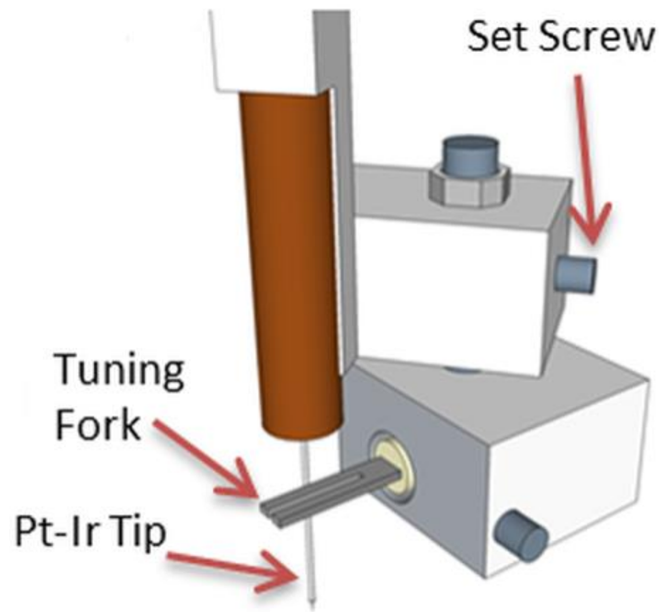

FIG. 2.10. Model of tuning fork holder with set screw that provides variable torque between the tuning fork and the probe tip.

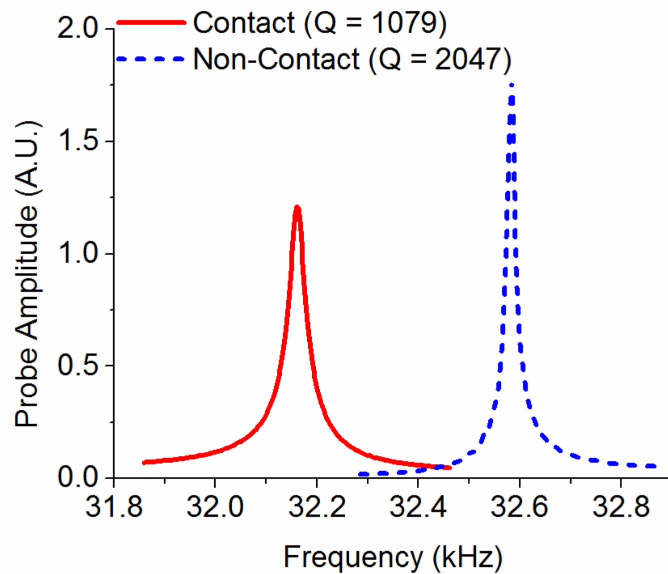

FIG. 2.11. Tuning fork probe amplitude as a function of frequency, showing typical responses of the tuning fork in contact (solid) and out of contact (dashed) with the NSMM tip. Contact results in roughly halving the measured Q and decreasing the resonant frequency by 0.42 kHz.

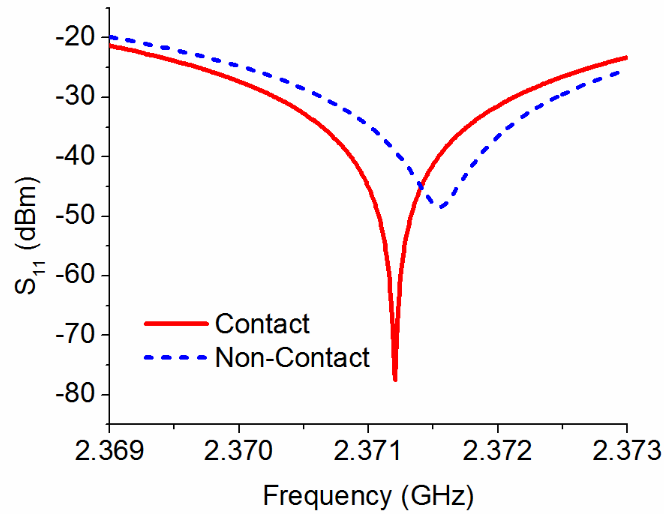

FIG. 2.12. Microwave reflection magnitude (S_{11}) versus frequency with the tuning fork in contact (solid) and out of contact (dashed) with the NSMM tip. Removing the tuning fork resulted in an increase in both the reflection minimum of 29 dBm and shift in position by 0.35 MHz.

The tuning fork feedback system works in conjunction with a Mad City Labs Nano-Drive 85 piezoelectric-activated z-stage which provides a scan range of 25 μm and theoretical resolution down to 0.2 nm. Operating resolution is closer to 10 nm, easily capable of discerning ≥ 100 nm height variations between CIGS grain boundaries. This z-stage was mounted on the x-y stage with the sample holder attached, eliminating unwanted coaxial cable movement during scanning. With this feedback improvement, we were able to take high resolution images of photovoltaic CIGS with large scan areas (up to 30 x 30 μm^2) and long scan times (4 hours).

The final important design change centered on the illumination system used to investigate the photoconductive effect and provide contrast to dark state images. We will show published results on illuminated CIGS using the previously mentioned 405 nm diode-laser from Section 2.3, but for now we will discuss several limitations to the setup. The first is that its wide area of illumination (on the order of 1 cm^2 caused significant heating of the tip-sample interface. This was detected with the feedback system as the sample was pulled away to prevent crashing into an elongated tip.

Because the power level of the diode could not be easily controlled, turning it on added noise to the height control signal. This was remedied by pulling the sample 5 μm away from the tip before switching between dark and illuminated scanning conditions. However, this also resulted in shifts in both the x and y directions of several microns from the original measurement point. The second limiting feature was the restriction to a single wavelength of illumination for studying solar cells that are traditionally operated under broadband illumination (i.e. the sun). This has been improved upon with the installation of a Thorlabs multi-channel fiber-coupled laser source with parameters give in Table 2.1 below. To minimize the risk of laser exposure to the NSMM operator and other researchers in the lab, the new laser source has been coupled to a powered safety relay which is connected to a non-contact magnetic switch on the black box doors. When the doors on the black box housing the NSMM are open for any reason, the circuit is open and power to the laser source severed. To enable alignment of the laser with the door shut, an x-y stage controlled by two Thorlabs DC servo motors has been added with a 12 mm range of motion in each direction. Future work will involve illumination via a broadband light source with a class A spectrum developed at NIST by Tasshi Dennis[83]. This system utilizes spectral shaping to mimic solar intensity as a function of wavelength and provide a new standard in light sources used for photovoltaic testing.

TABLE 2.1. Spot size and intensity values for various wavelengths of the Thorlabs multi-channel fiber-coupled laser source.

	405 nm	**635 nm**	**808 nm**	**980 nm**
Spot size (cm^2)	0.071	0.013	0.018	0.01
Intensity (W/cm^2)	0.25	2.40	0.49	4.70

2.5 Height Profile Measurements

We will break the measurements down into two different sections: height profiles and image scans. Height studies are used to track changes in the frequency of the microwave reflection coefficient S_{11} minimum as a function of tip-sample distance. These scans have been completed using both the earlier STM feedback and the newer tuning fork feedback. In both cases, the measurement methodology has been the same. Under illumination from the 405 nm diode laser, the tip is brought to within ~10 nm of the sample (early NSMM design required movement of the tip while redesign only moves the sample). Upon entering feedback, the phase shifter in the RF circuit was tuned to achieve a large $|S_{11}|$ minimum thereby increasing sensitivity to small frequency shifts of the resulting peak. The tip-distance was then increased to 3 μm over the span of 100 steps with time-averaged frequency sweeps conducted by the VNA at each step. The minimum was calculated from each of these sweeps and its change in frequency divided by the initial minimum frequency ($\Delta f/f_o$) was plotted against the tip-sample distance. Upon completion of the illuminated scan, the tip and sample were brought back into feedback with the laser turned off. The measurement was repeated with no changes made to the tuning of the RF circuit, providing a contrast in measured frequency shift dependent upon generated minority charge carriers. Figure 2.13 provides an example frequency shift of the S_{11} minimum for a GaAs sample measured in the dark. It can be seen that the center frequency is near 4.5 GHz (used for all height measurements), within the bandwidth of the original NSMM design, and that Δf is on the order of 0.1 MHz. As predicted by our RLC circuit model, the coupling capacitance decreases at greater tip-sample distance, resulting in an increase in the frequency peak.

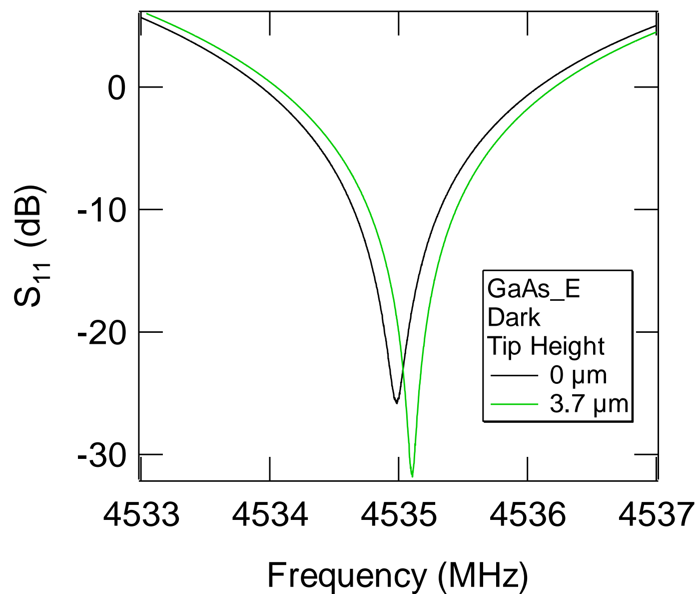

FIG. 2.13. Examples of microwave reflectance resonance curves for sample GaAs at two different tip heights in the dark.

Through the aid of analytical work by Pavel Kabos and Atif Imtiaz, we are attempting to extract carrier concentrations and conductivity changes using these height measurements. Details of fitting these curves are provided in Section 2.7 as well as an explanation of how full wave simulations are helping to reduce the number of unknown parameters. However, owing to the complex nature of photovoltaic samples and the penetrating properties of microwaves, these height profiles are still largely qualitative in nature. This is important to consider as we present modeled profiles on several semiconducting samples.

The first sample we will look at is a copper plate which provided a control for height profile measurements. As a conductor, the conductivity of copper is insensitive to light. Thus, any measured changes between the dark and illuminated state could likely be attributed to temperature affects from the laser diode heating the tip and sample. Figure 2.14 illustrates that the differences in dark and illuminated data were negligible, indicating that an increased temperature does not affect the microwave measurements.

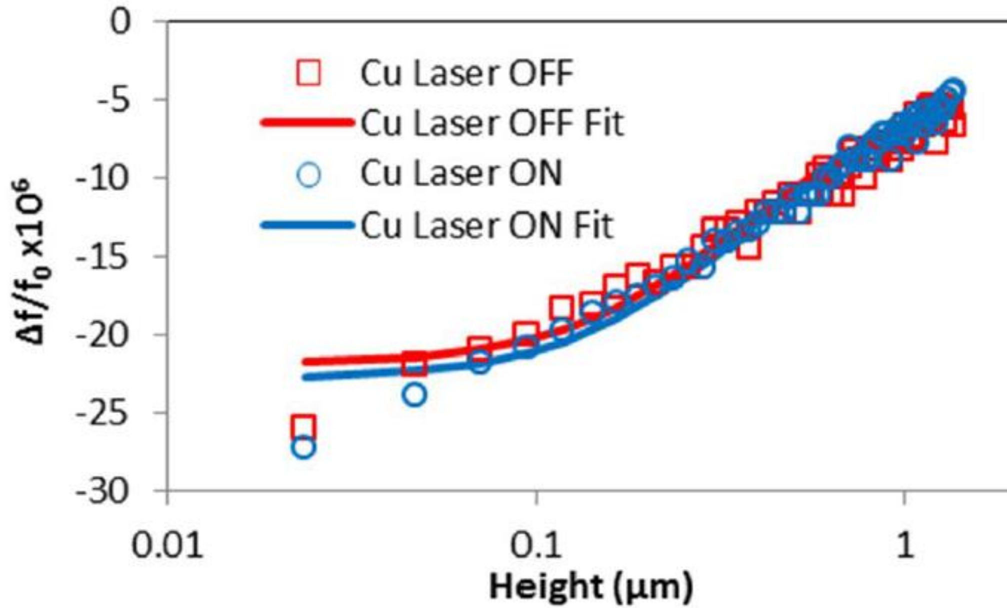

FIG. 2.14. Copper height-dependent frequency shifts fitted with model for dark and illuminated states. Overlapping data indicates negligible temperature effects from laser diode.

The next sample is a GaAs photovoltaic sample provided by Daniel Friedman at NREL. The completed photovoltaic has the device structure and dopant concentrations shown in Table 2.2 below, with the top passivation layer removed to expose the main GaAs layer for measurements. The bulk GaAs layer also has known carrier mobility (μ = 7000 cm^2 V^{-1}s^{-1}) and resistivity (ρ = 2.1 – 3.3 E7 Ωcm). As is shown in Fig. 2.15, a greater frequency shift was found in the illuminated state indicating a higher conductivity. The model required a ~2 % increase in carrier concentration to account for the greater frequency drop, comparable to reported values[84]. Deviations between the fit and the experimental data were attributed to the large skin depth of the GaAs sample. Microwaves were able to penetrate to the copper sample holder and subsequently altered bulk properties. A follow up study (Fig. 2.16) was conducted on the same sample to investigate spatial dependence of the height profiles for both illuminated and dark conditions. Each position is 1 μm apart and results in varying conductivity shifts. This is attributed to possible variation in sample

properties and/or sample contamination and demonstrates the need for high resolution imaging over large sample areas.

TABLE 2.2. GaAs sample properties.

Layer Function	Material	Thick -ness (μm)	Dopant and Carrier Concentration (cm^{-3})
Front Passivation	GaInP	0.5	Si, 1.6 x 10^{18}
Main Layer	GaAs	2	Si, 1 x 10^{18}
Back passivation	GaInP	0.05	Si, 1.6 x 10^{18}
Substrate	GaAs	~ 400	Si, n+

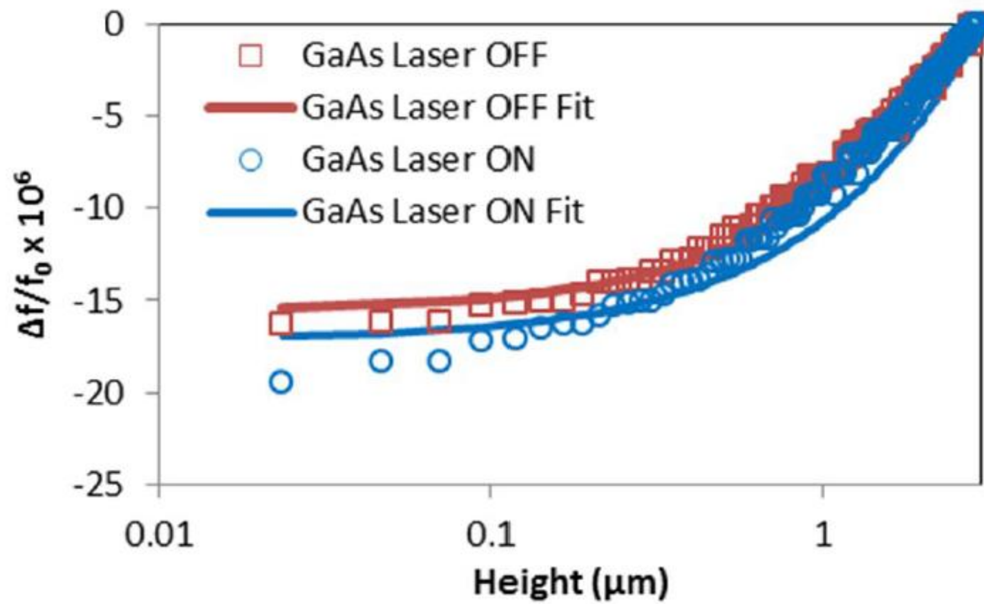

FIG. 2.15. GaAs height-dependent frequency shifts fitted with model for dark and illuminated states. Large skin depth at low conductivities enables microwaves to penetrate to the metal sample stage. This is accounted for by shifting the entire fitted curve vertically.

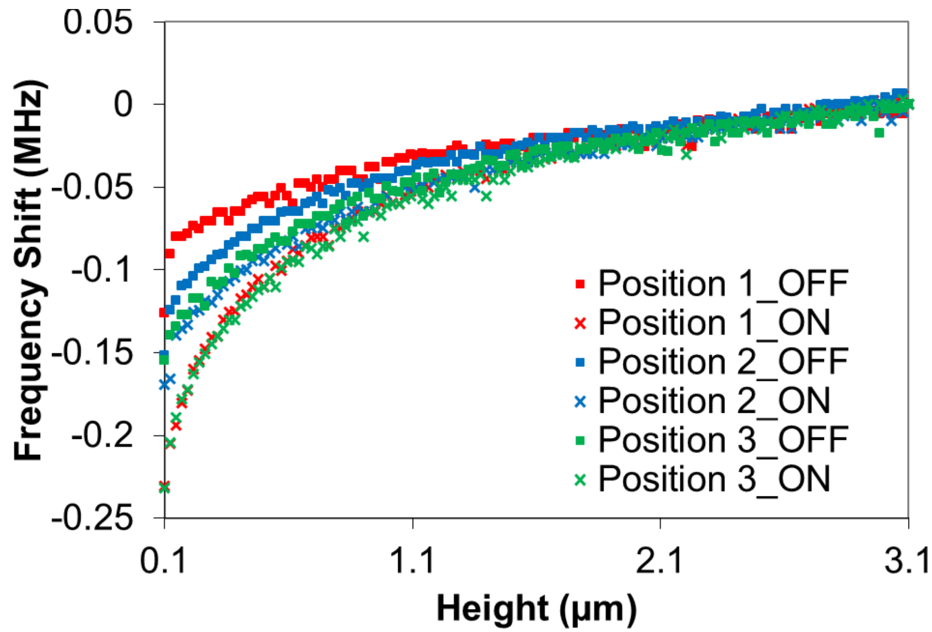

FIG. 2.16. Spatial dependence of height profile measurements on GaAs sample. Measurements were taken 1 μm apart and indicate possible changes in sample properties or sample contamination.

A bulk Si sample (no p-n junction present) with resistivity between 1 – 20 Ωcm and ~250 μm thick was also measured and resulted in a large frequency shift (Fig. 2.17). The higher conductivity in the illuminated state caused a large change in the complex permittivity value for the Si sample. This led to the change in concavity between the dark and illuminated experimental data, with the illuminated state exhibiting a concave downwards trend. The model required a ~500 % increase in carrier concentration to account for this change, which may be feasible for a Si sample with such low resistivity[85].

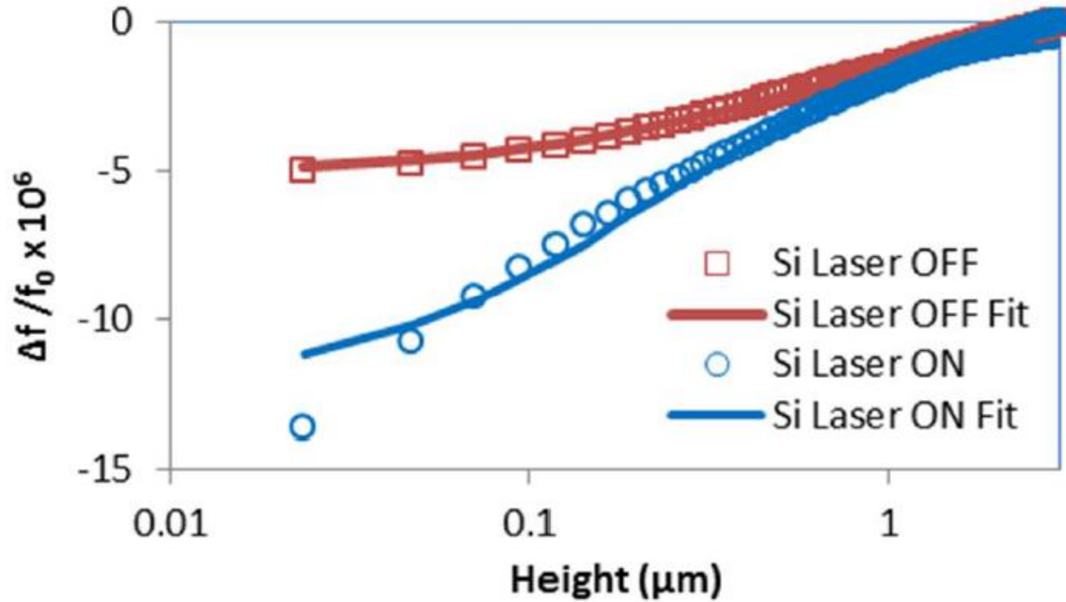

FIG. 2.17. Si height-dependent frequency shifts fitted with model for dark and illuminated states.

The final height profile study which will be discussed in this section focused on frequency shifts in CIGS at the four wavelengths provided by the Thorlabs multi-channel fiber-coupled laser source. The two CIGS samples used were fabricated using NREL's three-stage process[46-50, 86]. Deposition temperature for the main absorber layer was ~600 °C. The absorbers were then finished into devices using the standard passivation and contact layers (CdS, ZnO bi-layer, contact grids), however, an anti-reflective coating was not applied. Once current density-voltage measurements were taken for characterization, 50 % HCl by volume was used to remove the ZnO bilayer and CdS passivation layer, exposing the bare CIGS absorber beneath. Table 2.3 provides the Ga mole fraction, absorber thickness, and solar efficiency of the two samples studied. Figure 2.18 shows the J-V curves taken by Lorelle Mansfield at NREL and AFM scans taken by Atif Imtiaz to further characterize the sample. CS30 is the more efficient photovoltaic (16.8 %) with more uniform grain sizes recorded across its surface.

TABLE 2.3. Parameters for CIGS samples.

Sample	Ga mole fraction	Run No.	CIGS thickness (μm)	Avg. Efficiency (%)
CS30	0.3	C2554	2.0	16.8
CS70	0.7	C2553	1.8	12.8

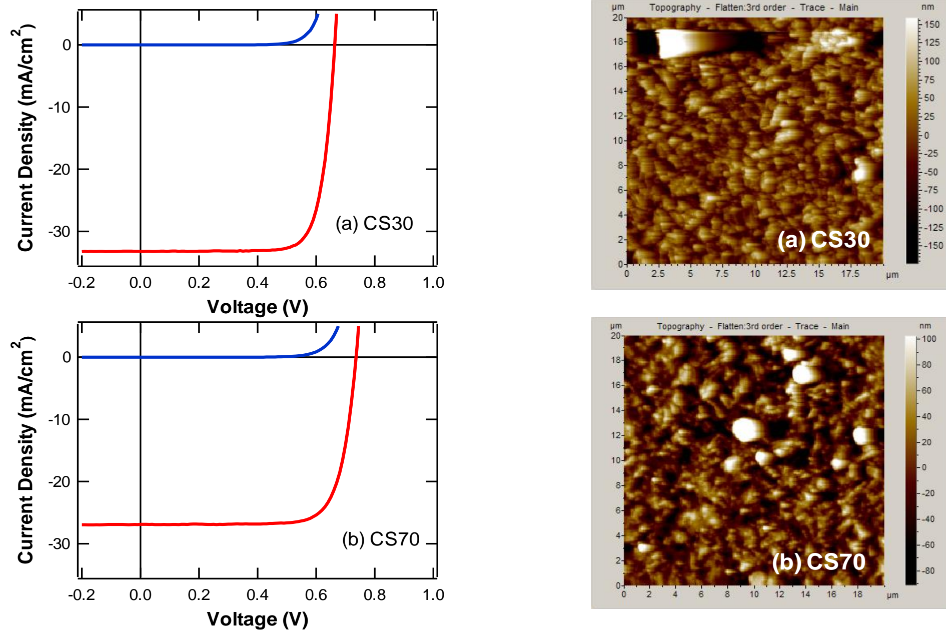

FIG. 2.18. Current density vs. voltage and topography from AFM scans for CS30 and CS70 CIGS samples.

We varied the methodology for this experiment in order to better determine the spectral response of the CS30 and CS70 CIGS cells as well as examine the measurement repeatability. To eliminate any height dependent effects, the NSMM tip was brought into contact with the sample under illumination at the wavelength in question. The resonance frequency was recorded prior to turning off the light source. At this point, the frequency shift due to the change in charge carriers was also

recorded. This measurement was conducted five times at each wavelength at the same spot on each sample to provide the data points and respective standard deviation shown in Fig. 2.19. It can be seen that the more efficient CS30 sample had a statistically significant greater frequency shift at all wavelengths except for 635 nm. As shown in Table 2.1, the spot diameters and subsequent intensities at each wavelength vary. However, this can be accounted for by comparing the difference in frequency shifts between CS30 and CS70 at each wavelength with the difference in spectral-dependent quantum efficiency values (Fig. 2.20) as we've shown in Fig. 2.21. The frequency and quantum efficiency differences were plotted on separate axes and had their maximum values normalized to one another. Here, the respective differences follow roughly similar trends indicating that the two measurements track each other relatively well. The exception occurred at 405 nm where a much greater than expected frequency shift was found. This occurred because the quantum efficiency data was recorded with the top passivation layer intact while the measurements had it etched away. The passivation layer absorbs wavelengths shorter than 490 nm thus the actual quantum efficiency response for unpassivated samples is unknown.

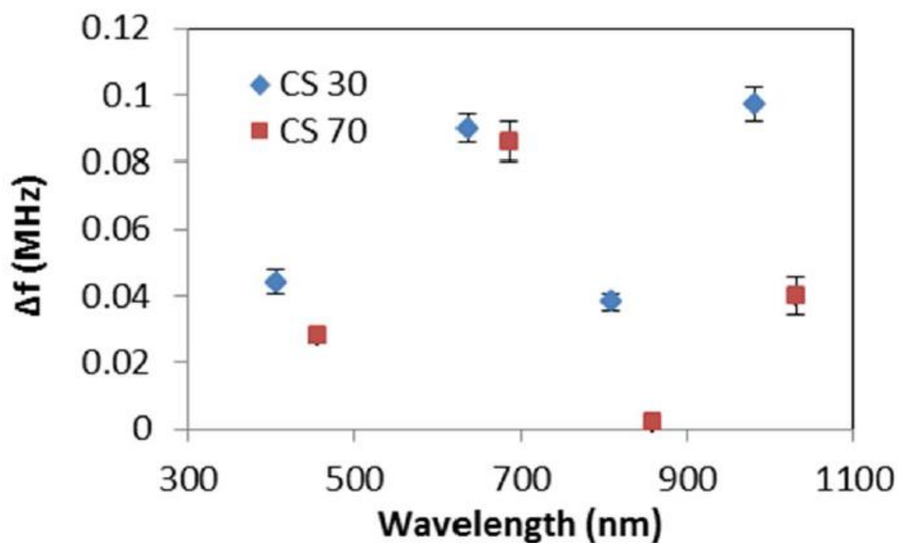

FIG. 2.19. Frequency shifts for CS30 and CS70 at 405 nm, 635 nm, 808 nm, and 980 nm. For viewing clarity, CS70 data has been shifted 50 nm along the x-axis.

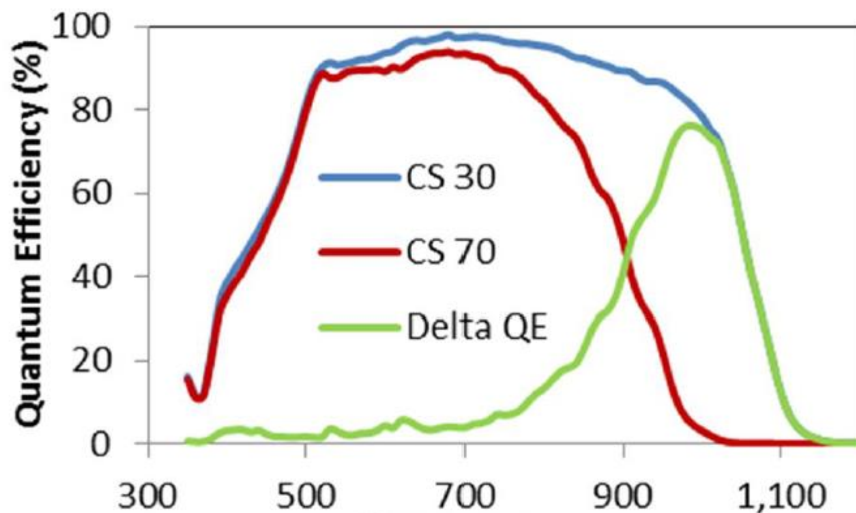

FIG. 2.20. Spectral dependence of the quantum efficiency for CS30 (blue), CS70 (red), and the difference between the two (green).

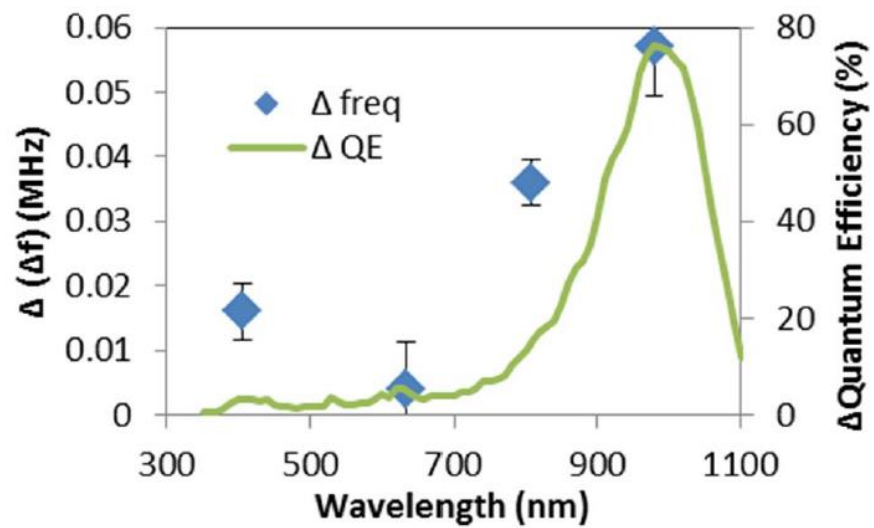

FIG. 2.21. Difference in frequency shifts plotted against difference in quantum efficiency as a function of wavelength.

2.6 Imaging of Photovoltaics

At the end of Section 2.3, we provided a preliminary image for topography and microwave reflection coefficient S_{11} data over a 1 x 1 μm^2 area on a CIGS sample. There existed an observable shift in $|S_{11}|$ between dark and illuminated states likely convoluted with tip drift and/or sample tilt. Furthermore, possible features in the S_{11} signal were detected in the illuminated state corresponding to grain boundary size. With the addition of a tuning fork feedback system capable of providing height control down to 10 nm over extended time periods and varied sample topographies, we can now present high resolution NSMM images with submicron detail.

Prior to testing the NSMM on a photovoltaic sample, some baseline measurements were performed to verify the functionality of the tuning fork feedback system. For this purpose, a test sample consisting of Au lithographically patterned onto a quartz substrate was imaged over a 7.5 x 7.5 μm^2 area. The exposed quartz trench was 5 μm wide with a nominal depth of ~220 nm. A 5 V bias was applied to the Au on the right side of the trench, while the left side remained electrically isolated. As seen in Fig. 2.22(a), the topography scan revealed the expected trench width of 5 μm and a larger than expected depth of ∼350 nm. The line-to-line variations were attributed to tip drift. Fig. 2.23(b) provides a simultaneously acquired S_{11} amplitude image illustrating changes between the biased Au, the floating Au, and the bare quartz regions. The dependence of the S_{11} amplitude on the bias voltage applied to the gold surfaces was attributed to contaminants in the tip-sample gap, e.g. a thin water film, that display voltage-dependent electromagnetic properties. A horizontal topography trace (Fig. 2.24) was used to estimate the sample tilt relative to the scanning plane of the tip. A height variation of 1 μm for every 50 μm of horizontal displacement was noted. This effect can be removed through image processing. Furthermore, the measured trench depth of ~350 nm was clearly distinguished from its gold surroundings. This suggested that the tuning fork

feedback system should be able to effectively track sub-micrometer-scale variations in height between grain boundaries in typical CIGS material[87-89].

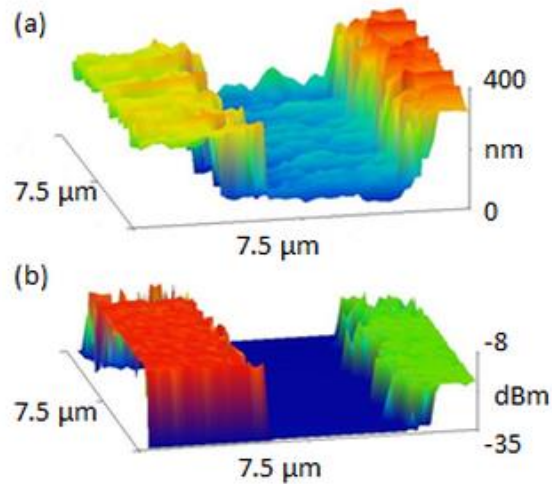

FIG. 2.22 (a) Sample topography showing 5 µm wide trench with side walls of roughly 350 nm in height. (b) Sample S_{11} amplitude at 2.26 GHz with evident distinction between the grounded gold region (left), exposed quartz trench (center), and biased gold region (right).

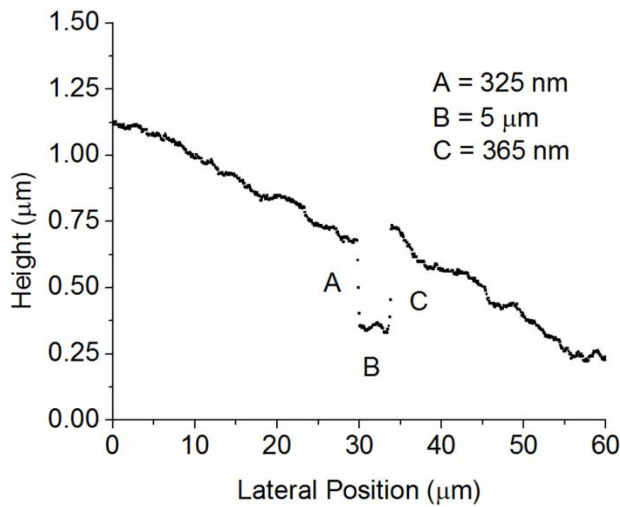

FIG. 2.23. Single horizontal topography scan across the test sample showing the 5 µm quartz trench with sample tilt of 1 µm for every 50 µm laterally.

To optimize sensitivity to S_{11}, the phase shifter was used to tune the microwave response above the CIGS substrate. Once the microwave response was tuned, a working continuous wave (CW) frequency was selected. Note that in order to avoid confusion in the interpretation of the data, the optimum working frequency is not equal to the matching frequency (minimum of frequency sweep). Variations in local capacitance and resistance may result in either positive or negative shifts of the resonance frequency. By operating on the side of the resonance curve rather than the minimum, the direction of the frequency shift is unambiguous. For the imaging data presented in this paper, an operating frequency with a -0.04 MHz offset from the resonance was chosen to minimize variability and avoid confusion over S_{11} amplitude shifts.

We verified photovoltaic performance based on a measurement of the CIGS sample provided by Lorelle Mansfield at NREL. This sample had the same device structure as the CS30 and CS70 samples described in Section 2.5, but in this case, the passivation and top contact layer were left intact. Its current density-voltage (J-V) response (Fig. 2.24) revealed an efficiency of 17 %. Silver paste was used to establish an electrical contact to the sample surface in order to apply a 2 V bias relative to the tip. The surface of a CIGS material is typically characterized by grains on the order of 1 μm laterally with differing material composition and resultant electrical characteristics found along the grain boundaries. This provided an ideal platform for testing the NSMM's ability to track local changes in capacitance due to changing material properties during scanning.

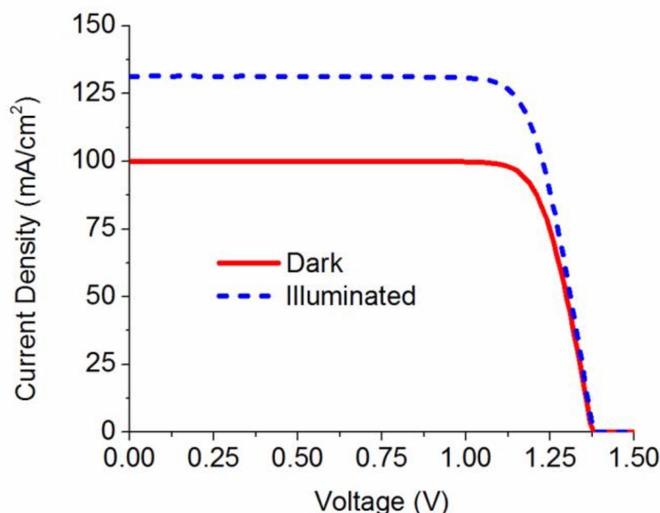

FIG. 2.24. Measured current density versus internal voltage for CIGS. The measurements revealed a 75 % fill factor and 17.125 % efficiency (ratio of the maximum power point to the incident light power density). Both the dark state current density (solid) and the illuminated state (dashed) are shown. Data for figure provided by Lorelle Mansfield.

Figure 2.25 presents the scanning results on the CIGS sample in both dark and illuminated (405 nm laser-diode) states. The NSMM was initially set up in the dark state while a 2 V bias was applied between the CIGS sample and probe tip. The sample was raised towards the tip at a rate of 8.3 nm/s, while the tuning fork was operated in phase-locked-loop mode. Once the distance between the sample and tip became sufficiently small (< 10 nm), a ~5 Hz decrease in the tip/tuning fork contact resonant frequency was detected, and the tuning fork feedback loop was engaged. This tip-sample distance was maintained throughout both scans. The phase shifter was then tuned to 1.43^o, and a CW operating frequency of 2.37 GHz was chosen. Topography, S_{11} amplitude, and DC images over an area of 30 x 30 μm^2 were acquired and are shown in Fig. 2.25. The scanning speed was fixed at 0.5 $\mu m\ s^{-1}$.

Increased thermal and mechanical noise inherent when operating in ambient conditions necessitated the use of image processing provided by Kevin Coakley at NIST. For each scan line in the image, a one-dimensional (1-D), smoothly-varying trend was estimated with a robust

implementation of the local regression method known as LOCFIT[90]. This trend, which accounts for possible tip drift and sample tilt within a scan line, was subtracted from the observed scan to produce a 1-D residual scan. 1-D residual scans were aggregated to form a residual image which was then denoised by the Adaptive Weighs Smoothing (AWS) method [91]. In the AWS method, a local-likelihood model was fit to a neighborhood centered about each pixel where the neighborhood size and associated weights were adaptively determined for each pixel. The AWS method suppresses additive noise while preserving edge features associated with grain boundaries. For topography, denoised residual images are shown where the minimum value of each image is 0 μm. However, for the DC and S_{11} amplitude, we determined the mean of the associated trend images from the LOCFIT analysis and added these means to the respective denoised residual images.

Fig. 2.25(a) depicts the surface topography with micrometer-sized grains in evidence across the surface. Expected height variations on the order of 1 μm are observed between grain boundaries. The clearly distinguished linear step edge seen to the left of the image will be discussed in more detail at the end of this section. Fig. 2.25(b) provides simultaneously recorded DC data across the same region with a 2 V bias applied to the sample relative to the tip. Good correlation between the conductivity and topography data for larger grains, which are typically a characteristic of higher efficiency CIGS[87, 92], is observed, indicating that these grains represent regions of lower conductivity. Fig. 2.25(c) illustrates strong correlation between the topography and S_{11} variations and demonstrates sub-micrometer spatial resolution of the reflected microwave signal. To minimize an observed tip drift due to thermal fluctuations, the sample had to be pulled back ~5 μm from the tip before the laser diode was turned on. Upon re-approach, the sample was again scanned under the same frequency and phase-shifter settings, but with the sample now illuminated by 405 nm light. Fig. 2.25(d) shows topographical data over the same area. While a small (< 3 μm) displacement is seen in the x and y directions due to thermal drift, the primary grain features

are once again located with height variations on the order of 1 μm, indicating that illumination does not induce excessive thermal drift or significantly disrupt the tuning-fork feedback system. Fig. 2.25(e) depicts the corresponding DC data, where the effects of the less conductive grains have become minimized. Finally, Fig. 2.25(f) provides the S_{11} response in the illuminated state. As with the DC data, the grain effects become less pronounced in the illuminated state, resulting in a more uniform image overall. While many of the larger grains remain present, less detail is retained and smaller grain boundaries become undefined (altered features present in both topography scans are highlighted in the image with an enhanced view of the solid box shown in Fig. 2.26). This result is attributed to photoexcited charge becoming trapped in the vicinity of grain boundaries and modifying the local depletion[87, 93-94]. NSMM is sensitive to these fluctuations in localized capacitance resulting in a change in measured S_{11}. While the true cause of these depletion regions and their impact on CIGS' efficiency are not currently well understood, KFM measurements have shown comparable results when contrasting dark and illuminated conditions[95]. Defect type and density play a significant role in carrier concentrations at grain boundaries and help explain the variation across individual grain boundary response to illumination. Quantitative analysis and modeling of spatially broadened DC current and S_{11} data in the illuminated state are avenues for further study.

A linear step edge, parallel to the y-axis, is apparent on the left side of both of the topography scans. This transition is also easily seen in both S_{11} images, while a faint trace is visible in the DC images. Because electrical characteristics appear continuous on either side of the line, the abnormality is believed to be a step in topography produced during fabrication rather than the presence of a local collection grid.

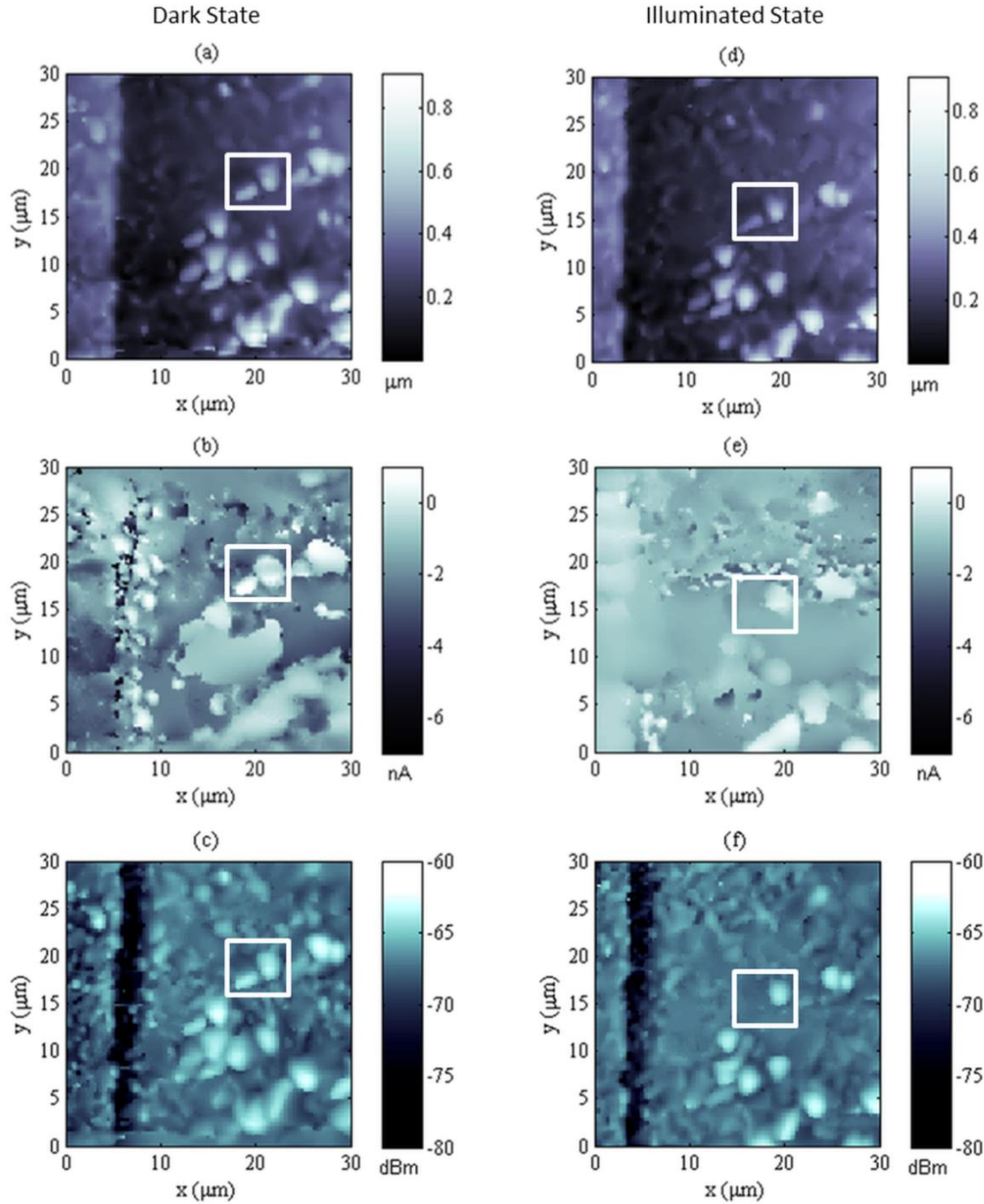

FIG. 2.25. Processed CIGS data with fixed tip-sample height across a 30 x 30 µm^2 scan area. (a) Topography in the dark state showing grains several micrometers across with height variation on the order of 1.5 µm. (b) DC data in the dark state with low absolute values corresponding to concentrations of raised grains. (c) S_{11} data in the dark state with sharp contrast likely corresponding to variation in depletion due to trapped charge localized at or near grain boundaries. (d) Topography in the illuminated state. Prominent grains can be matched with those of the dark state indicating that illumination does not substantially affect tuning-fork feedback response. (e) DC data in the illuminated state with less contrast at grain boundaries due light-generated charge reducing depleted regions. For both the dark and illuminated current images, quenching of the data occurred as current values periodically saturated the preamplifier. (f) S_{11} data in the illuminated state with decreased contrast at the grain boundaries; once again caused by light-generated charge reducing depleted regions and contrast in local capacitance. The square area enclosed by the solid lines corresponds to the area magnified in Fig. 2.26.

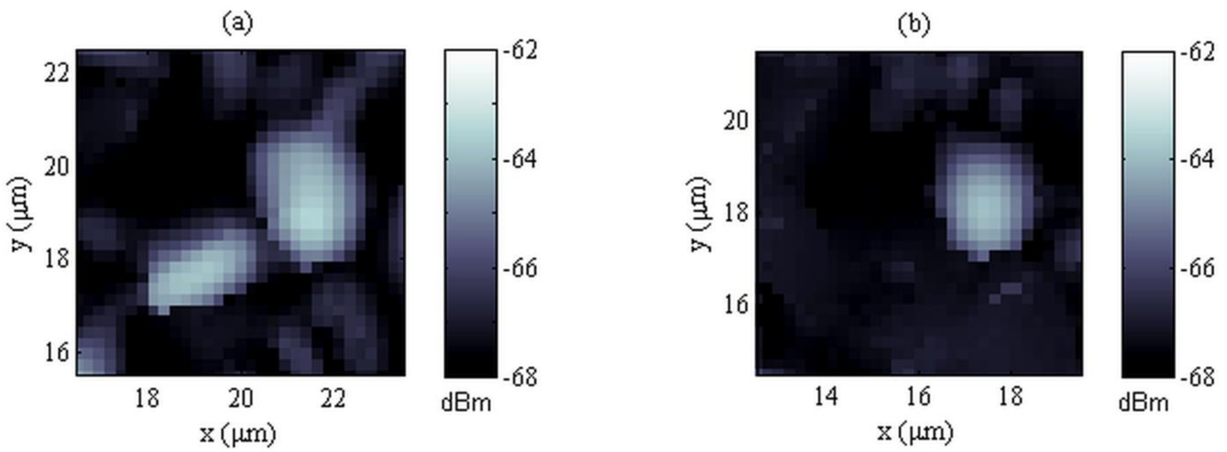

FIG. 2.26. Zoomed in S_{11} images from solid, highlighted region in FIG 3.21. 3.22(a) S_{11} data in the dark state showing two grains also found in the topography. 3.22 (b) S_{11} data in the illuminated state with one grain having disappeared. Because this feature is still present in the illuminated topography scan, its absence is attributed to a reduction in local depleted regions at the grain and a subsequent loss in capacitance contrast.

2.7 Modeling the NSMM

One of the ongoing goals of this project is to obtain quantitative, spatially dependent carrier concentration measurements from an image scan on a photovoltaic sample. In Section 2.2, we discussed progress that had been made in this area on bulk samples. Photovoltaics, in particular third generation designs, are inherently more complex to model due to their inhomogeneity and multilayered structure. While we can currently offer qualitative contrasts between images under different illumination conditions, we must first build on modeling the height profile measurements from Section 2.5. We begin by updating the RLC model to reflect out tip sample interaction (Fig. 2.27)[26, 28, 96-97]. The model resistance (R_{sample}) and capacitance (C_{sample}) of the photovoltaic sample are in series with the parallel coupling capacitance ($C_{coupling}$) and resistance ($R_{coupling}$) between the tip and the sample. This coupling capacitance is dependent upon changes in both tip-sample distance (held constant by the tuning fork feedback) as well as local electromagnetic material variations (detected by changes in resonant frequency and S11 amplitude). $R_{coupling}$ accounts for the thin water film typically found on samples in ambient conditions. At the operating frequencies, $R_{coupling} \gg 1/\omega C$ and can be neglected. The capacitance between the outer conductor and the sample (C_{out}) can be ignored as it is very large compared to C_{sample}. Finally, L is only important for superconducting samples in this frequency regime and is left out of the model.

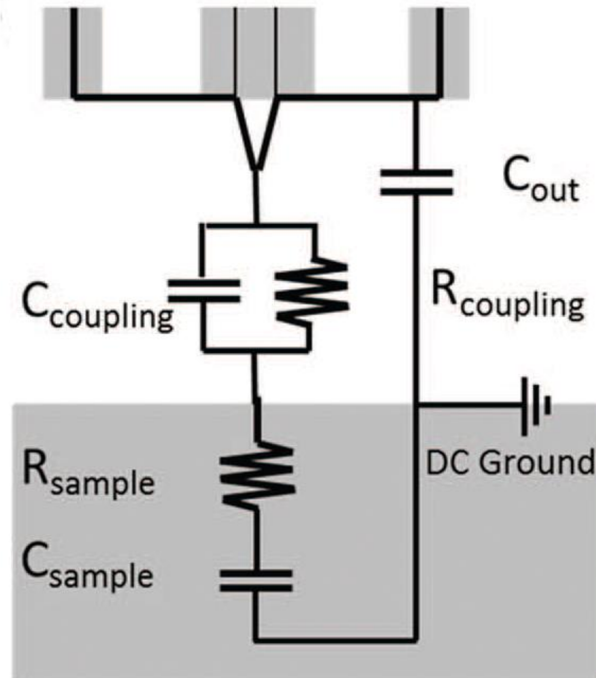

FIG. 2.27. RLC model of NSMM tip-sample interaction. Analytical and COMSOL models presented in this section attempt to model $C_{coupling}$, which is dependent upon tip geometry, tip-sample distance, and local electromagnetic material variations.

Frequency shift was plotted as a function of tip-sample distance; a change largely dependent on $C_{coupling}$ between the tip and sample. Electrostatic imaging methods developed by Gao provide one means by which to estimate this capacitance. However, this model remains unfixed allowing effective tip geometry, coupling capacitance, and sample conductivity to all serve as fitting parameters. This leads to variation in predicted photoconductivity values with small changes in the model, restricting its usefulness as a quantitative tool. In an effort to combat this problem, we have used COMSOL to create full field simulations of the coupling capacitance. COMSOL is ideal in that our tip geometry can be modeled as 2-D axisymmetric, allowing for a high mesh density to be calculated relatively quickly (< 1 min for a single geometry). Furthermore, parameterization of the model enables factors such as tip-sample distance, sample permittivity, and tip geometry to be

readily changed without reconstruction of the model. We will cover one implementation of COMSOL here and how simulated $C_{coupling}$ compares to different analytical approaches.

COMSOL's strength lies in its ability to perform quasi-static calculations on a 2-D axisymmetric geometry before interpreting the results in a 3-D environment. We will focus on modeling the tip as a simple disk held above a metal-backed Si sample. The close up geometry shown in Fig. 2.28 is rotated around the z-axis at r=0 to form the 3-D model. The disk (tip) is made of Pt-Ir and has a radius of 0.5 μm and a thickness of 0.1 μm. It is initially held 20 nm above a Si sample ($\sigma = 1 \times 10^{-12}$ S m^{-1}, $\varepsilon_r = 11.7$) with a radius of 50 μm and a thickness of 250 μm. This is then backed by a Cu layer of radius 50 μ and thickness 10 μm. The top of the Cu layer has a 2 V bias applied while the tip is held at ground. The entire model is surrounded by a zero charge air boundary.

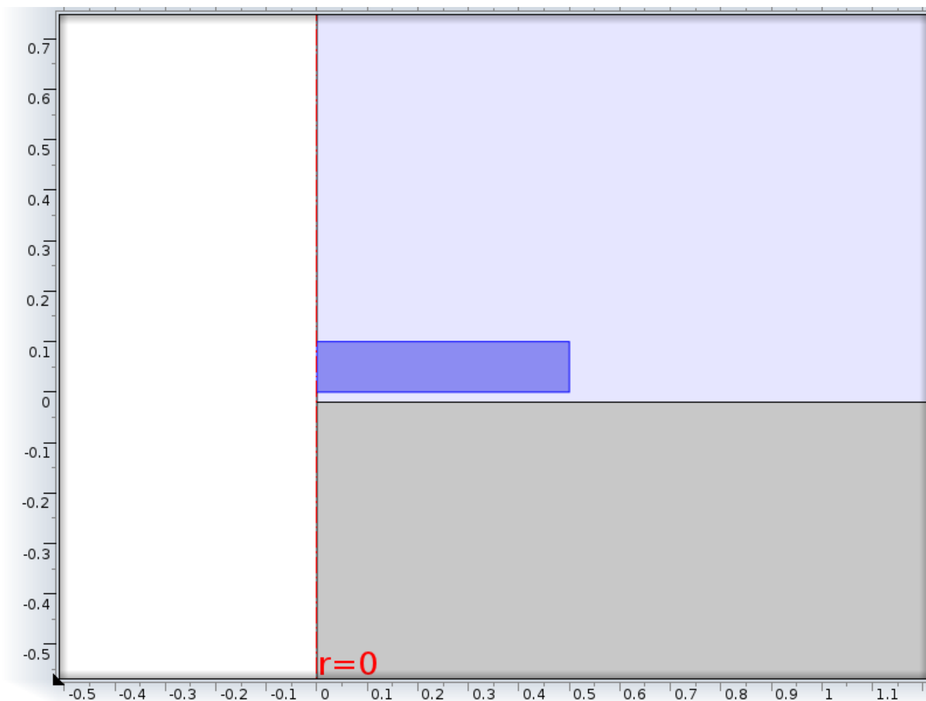

FIG. 2.28. Close up of 2-D axisymmetric COMSOL model showing tip disk (blue) suspended 20 nm over Si sample. The geometry shown is rotated around r = 0 to form a 3-D model.

Figure 2.29 demonstrates the computational advantage gained by modeling a 3-D structure in 2-D. Dimensions for the entire geometry range between 20 nm (tip-sample gap) and 250 μm (Si layer thickness). The full view of the geometry presents a relatively fine mesh across the structure, while the zoomed in region showcases COMSOL's ability to automatically seed high-aspect ratio features to enhance accuracy. A consumer grade computer (2.40 GHz quad-core with 4 GB RAM) can solve this 17,000 element mesh to calculate $C_{coupling}$ and the resultant electric field in 30 s. This, in turn, allows for 100 tip-sample height calculations to be computed within a reasonable time frame and compared with analytical solutions developed by Pavel Kabos and Atif Imtiaz.

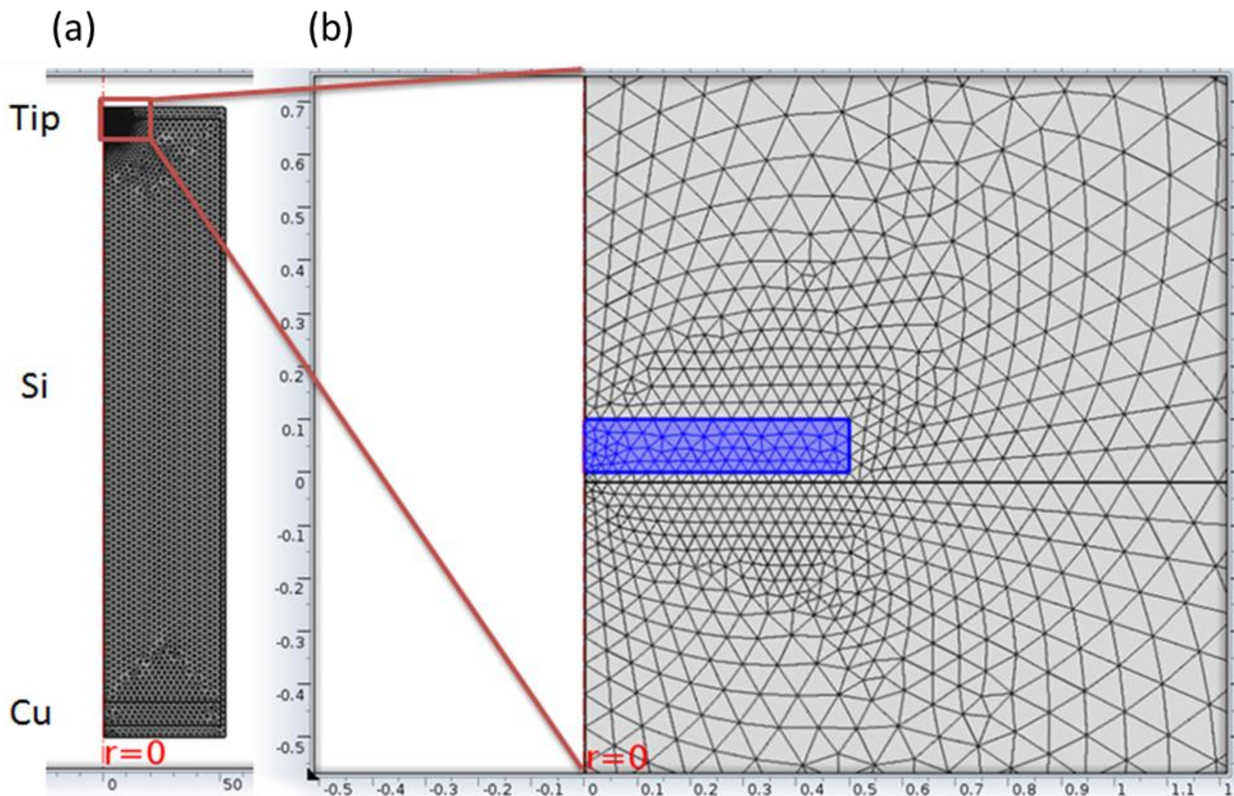

FIG. 2.29. (a) Full view of meshed COMSOL model showing ~17,000 elements and thick Si layer over backing. (b) Close up of tip-sample area demonstrating model's ability to finely mesh high aspect ratio designs.

We have already covered image sphere method of calculating $C_{coupling}$ developed by Gao in Section 1.2. This model will be used to plot capacitance of the tip over a metal sample (C_{Metal}) and a dielectric sample ($C_{Dielectric}$) as a function of height. In addition, we will briefly describe two additional analytical models that have been used to simulate microscope probe-sample interaction. The first is the parallel plate model with a fringe capacitance added in. Parallel plate capacitance (C_{PPC}) can be calculated using the following relation:

$$C_{PPC} = \frac{\varepsilon_r \varepsilon_0 A}{d} \tag{2.6}$$

where ε_r is the relative permittivity of the dielectric between the two plates, ε_0 is the permittivity of free space, A is the area of the plates, and d is the distance between the two plates. We can add to this equation a term for fringe capacitance correction developed by Kirchhoff [98]:

$$C_{fringe} = 1 + \frac{b}{\pi} \ln\left(\frac{16\pi}{b} - 1\right) \tag{2.7}$$

where b is the aspect ratio

$$b = \frac{d}{R} \tag{2.8}$$

and d is the disk separation and R is the disk radius. A fourth analytical model can be taken from Gomila's work modeling nanoscale capacitance microscopy on thin film dielectrics using an AFM probe[99]. Our NSMM tip is likened to the AFM probe shown in Fig. 3.28, allowing the capacitance (C_{AFM}) to be calculated using the following relation:

$$C_{AFM} = 2\pi\varepsilon_0 R ln\left[1 + \frac{R\cdot(1-\sin\theta_0)}{z+h/\varepsilon_r}\right] \tag{2.9}$$

where h is the thickness of the film, z is the distance between the tip apex and film, R is the effective tip radius, and θ_0 is the cone angle of the tip (Fig. 2.30).

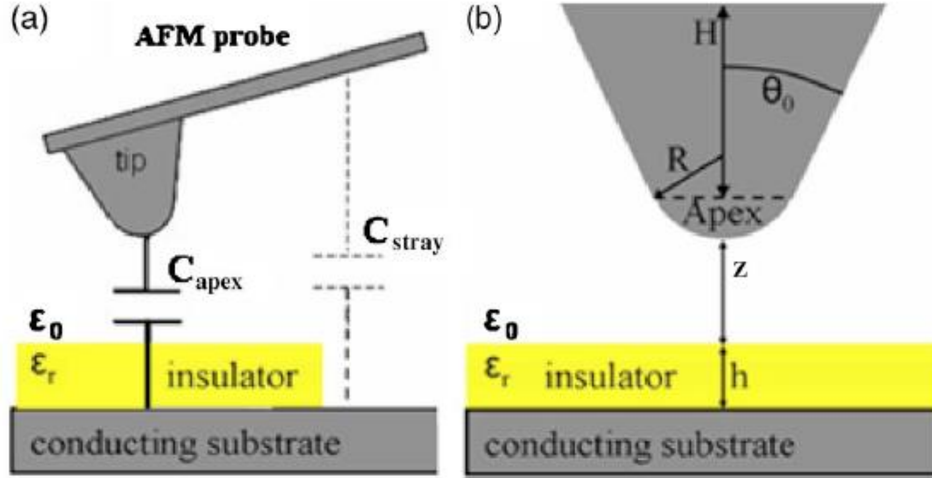

FIG. 2.30. Schematic representation of (a) a nanoscale capacitance measurement and (b) the tip-sample system as modeled in the analytical calculations. Figure from reference[99].

The four analytical models are plotted against the capacitance calculated from COMSOL (C_{sim}) as a function of tip-sample distance (20 nm – 3.02 μm) (Fig. 2.31). Both axes are plotted on a logarithmic scale to highlight differences between overall trends in each model. The parallel plate model with fringe capacitance (C_{PPC}) predicts the highest $C_{coupling}$ at small distances before falling away rapidly as a function of $1/d$. As expected, the two sphere models based on Gao's work, C_{Metal} and $C_{Dielectric}$ track each other closely across the height range. The dielectric model calculates a lower capacitance as its presence of the dielectric effectively increases the distance between the tip and ground. Finally, C_{AFM} and C_{Sim} closely match each other across the height range, with only a small offset capacitance needed to account for the difference. As was shown in Section 2.5, variations on the C_{AFM} model have been used to accurately model height-dependent frequency changes in photovoltaics. Due to its close similarities, our preliminary COMSOL C_{sim} modeling results make it a viable replacement for analytical techniques, removing the need to use tip geometry as a fitting factor. In Section 3.3.2, we will develop a separate analytical approach capable of modeling interactions between a NW probe and sample that also eliminates probe

geometry as a fitting factor. This reduction in unknown experimental variables contributes towards the quantification of microwave measurements on unique material systems.

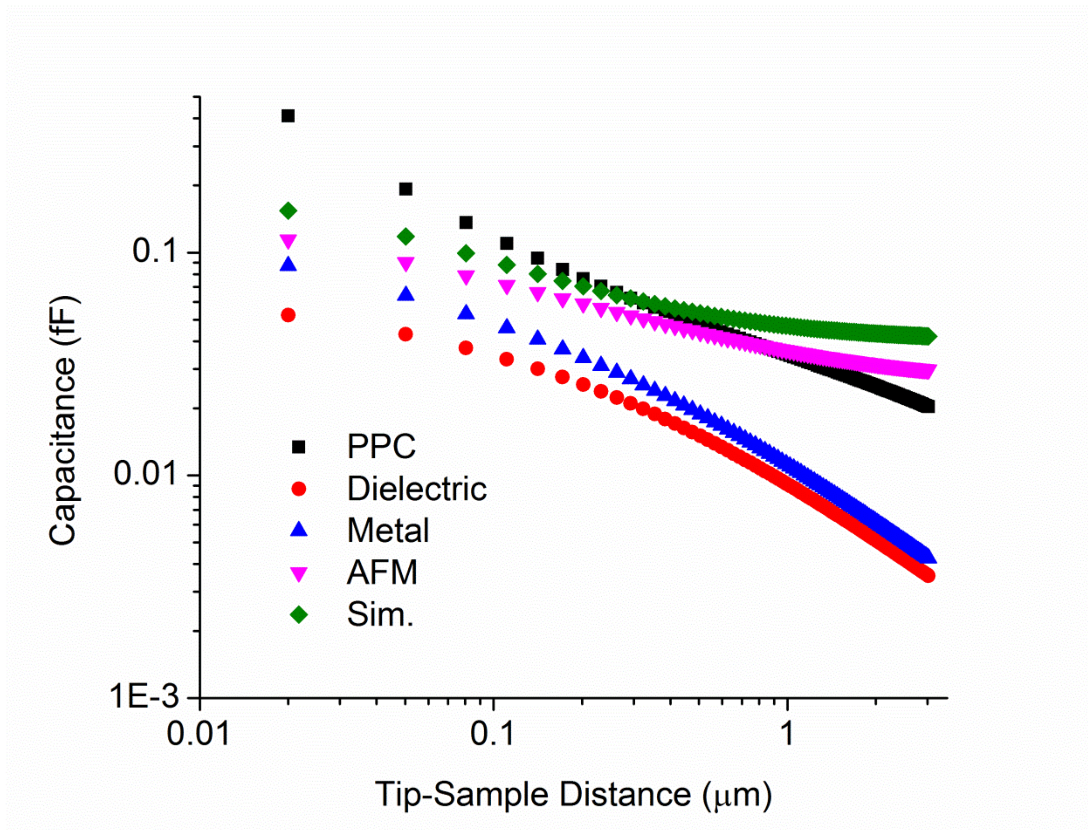

FIG. 2.31. Capacitance as a function of tip-sample distance plotted on a logarithmic scale. Four analytical models (developed by Pavel Kabos and Atif Imtiaz) are compared to a simulated COMSOL model, with C_{AFM} indicating the closest fit.

Chapter 3

GaN Nanowire Probe for Near-Field Scanning Microwave Microscopy

CONTENTS

3.1 Overview 93

3.2 Fabrication and Testing of Ti/Al NW Probe 94

3.2.1 Fabrication 94

3.2.2 Microcapacitor Calibration Sample 96

3.2.3 Microwave Results 98

3.2.4 Topography and Mechanical Wear Results 104

3.3 Fabrication and Testing of W-ALD NW Probe 107

3.3.1 Fabrication 107

3.3.2 Microwave Results and Testing 111

3.3.3 Imaging MoS_2 Sample 116

3.1 Overview

The push to better characterize advanced materials at the nanoscale has precipitated the development of a multitude of scanning probe microscopes. With measurement resolution and repeatability dependent upon both the probe's dimensions and material properties, careful attention to its design has proven imperative in pushing state-of-the-art imaging techniques. The advent of well-controlled nanostructures, including nanoparticles, nanotubes, and nanowires, has provided new avenues for fabricating probes capable of exploiting their unique architecture in order to obtain enhanced measurement precision. While this field was initially dominated by carbon nanotube-based atomic force microscopy tips[100-102], new studies have expanded their applications to tip-enhanced Raman spectroscopy[103], scanning tunneling microscopy[104], near-field optical microscopy[105], and scanning electrochemical microscopy[106], among many others. In this paper, we put forth a NW-based probe well suited for near-field scanning microwave microscopy (NSMM). Furthermore, the probe's robust, high-aspect ratio design makes it an ideal platform for use in alternative scanning probe microscopes.

3.2 Fabrication and Testing of Ti/Al NW Probe

3.2.1 Fabrication

Previous advances in NSMM probes have sought to improve their microwave sensitivity through the addition of micro-transmission lines and waveguide structures[107-111]. Separate work on AFM probes has incorporated nanotubes and nanowires (NWs) into traditional Si cantilevers in an effort to improve topographical resolution and mechanical robustness[112-115]. Here, these two research thrusts have been combined, resulting in the development of a mechanically robust, GaN NW NSMM probe.

GaN NWs were chosen for this project due to their ideal mechanical, chemical, and electrical properties. The NWs are grown at NIST by use of catalyst-free molecular beam epitaxy[116-119]. The NWs form a wurtzite (hexagonal) structure with differences in surface energies, diffusion coefficients, and sticking coefficients driving growth predominantly along the c-axis, as opposed to the NW sidewalls. High-temperature and ultrahigh-vacuum growth conditions, as well as the use of a catalyst-free substrate and a slow growth rate, result in the creation of essentially defect-free NW structures. GaN NWs are typically grown on a Si <111> substrate with an AlN buffer layer to prevent nitridation of the wafer and interdiffusion of Ga and Si.

The probe is assembled by modifying a commercial contact-mode Si cantilever (12 kHz CLR-10 tip by VISTAprobes) using a focused ion beam (FIB). As shown in Fig. 3.1 (a), the ion beam is used to shear off the Si tip prior to boring a hole 5 μm deep. The OmniProbe Nanomanipulator housed within the FIB is used to remove a single NW from a GaN forest located on a separate sample (b). The NW is inserted 1-2 μm in the hole and then Pt-bonded to ensure stability (c). The

entire cantilever and chip body were coated with evaporated Ti (20 nm)/Al (200 nm) layers to provide a conductive pathway for improved microwave signal propagation all the way to the end of the NW tip (d). The cantilever is inserted into an Agilent 5400 NSMM. Once inserted, a spring-loaded clip serves as the center conductor for a coaxial cable and sources microwave power from the vector network analyzer (VNA) down to the chip body and onto the NW tip, which is in contact with the device under test (DUT) (Fig. 3.2). During imaging, the NSMM acquires a contact-mode topographic image while simultaneously recording the amplitude of the complex reflection coefficient S_{11}[120]. A circuit identical to that described in[80] was employed to tune the system such that $Z_L \approx Z_0$, minimized microwave reflection during measurement.

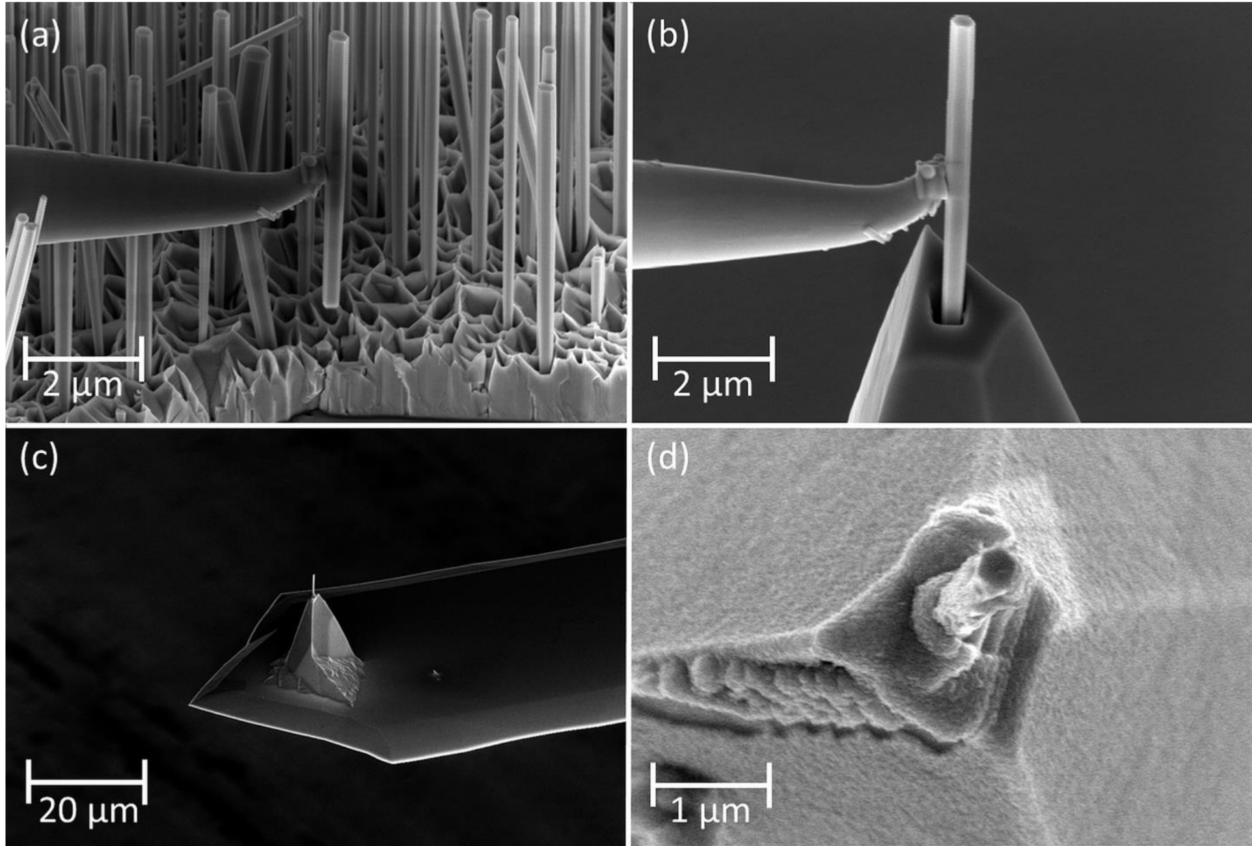

FIG. 3.1 (a) GaN NW forest with single NW being removed via the nanomanipulator. (b) NW placed inside hole cut into tip of Si AFM probe. (c) View of GaN NW probe. Pt bond is used to secure the NW perpendicular to cantilever. (d) Evaporated Ti/Al coating covers NW, cantilever, and chip body to provide a metal pathway for the microwave signal.

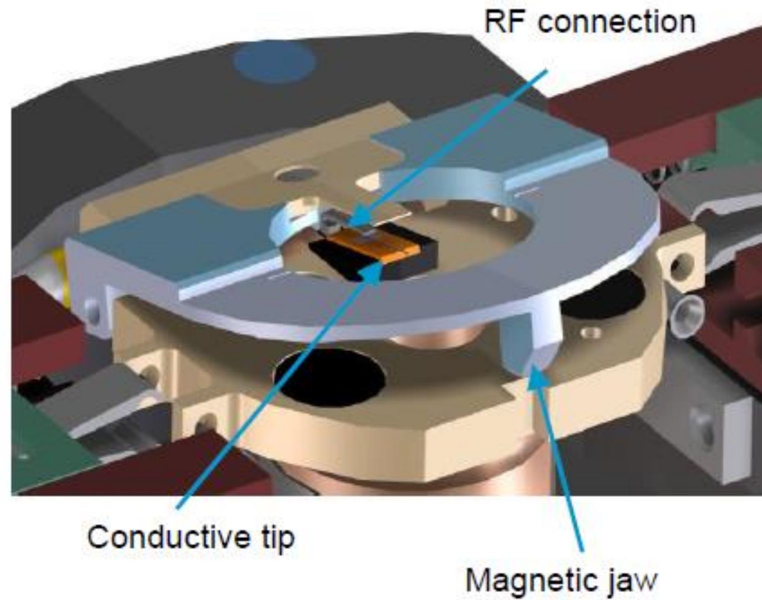

FIG. 3.2 Agilent microwave nose cone and probe holder. RF connection highlights clip which contacts top metal pad. Figure from reference[121].

3.2.2 Microcapacitor Calibration Sample

A sample consisting of arrays of microcapacitors deposited onto a SiO_2 staircase over Si served as the DUT and was used to test the effectiveness of the NW probe as an NSMM tip[120] (Fig. 3.3). The DUT was fabricated by depositing a 40 nm SiO_2 layer via plasma-enhanced chemical vapor deposition onto the polished side of a Si <100> wafer (resistivity ~0.005 Ω cm). Alternating photolithographic patterning and reactive ion etching created a series of four steps with 10 nm SiO_2 step heights. Four microcapacitors with diameters ranging from 1 µm – 4 µm were deposited on each step by electron-beam evaporation of Ti (20 nm)/Au (200 nm). The DUT dimensions were chosen to fit within a 50 µm x 50 µm scan.

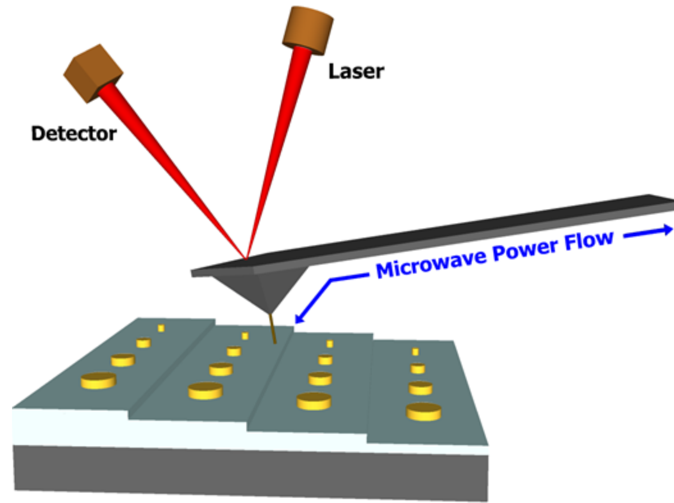

FIG. 3.3 Model of GaN NW probe scanning over the microcapacitor calibration sample. Laser-bounce feedback is used to maintain constant force during scanning.

In order to understand the contribution of the microcapacitors to the load impedance Z_L, each microcapacitor is modeled as an ideal parallel plate capacitor, C_{diel}, with the Si wafer and Ti/Au caps serving as the two plates and the SiO_2 layer as the dielectric. Because the SiO_2 layer is considerably thinner (10 nm - 40 nm) than the diameter of the plates (1 μm - 4 μm), edge effects are ignored. A second, stray capacitance between the DUT and AFM cantilever (C_{cant}) is also present and is in parallel with C_{diel}. The total capacitance encountered by the probe is thus:

$$C_{tot} = C_{diel} + C_{cant} \tag{3.1}$$

$$C_{diel} = \frac{A\varepsilon}{d}, \tag{3.2}$$

with A being the area of the Ti/Au caps, Ɛ being the dielectric constant of SiO_2, and d being the SiO_2 layer thickness. Images presented below show relative measurements of $|S_{11}|$ of the microcapacitor compared against that of the background SiO_2 film. C_{cant} was effectively constant during imaging, leaving variation in C_{diel} as the dominant contribution to changes in Z_L and the dominant contrast mechanism in the $|S_{11}|$ images.

3.2.3 Microwave Results

Four different probe types were chosen to analyze the performance of the GaN NW tip: (1) Ti/Al coated NW, (2) NW without a metal coating, (3) standard Si tip (same model as was used to make the NW probes), and (4) a commercial Pt tip (10 kHz 25Pt400A Rocky Mountain Nanotechnology) (Fig. 3.4). Each probe was scanned over the same area to allow a direct comparison of their microwave and topographical sensitivity. Before scanning, a phase tuner was used to set a $|S_{11}|$ minimum to -45 dBm near 2.5 GHz, for each tested probe. The measurement frequency was then selected to be 64 kHz greater than this minimum. By tuning the minimum for each probe to the same $|S_{11}|$, we were able to ensure that a quantitative comparison could be made. Fig. 3.5 (a) depicts an image of the change in $|S_{11}|$ across the microcapacitor array for the Ti/Al coated NW probe. The bottom right microcapacitor is clearly present and represents the smallest capacitance on the sample with a value of 0.7 fF. The bottom left microcapacitor is unexpectedly faint by comparison. This is likely due to contact issues during this portion of the scan or poor metal adhesion of this metal pad during fabrication. Fig. 3.5 (b) depicts the $|S_{11}|$ image for the bare NW probe. As can be seen, the bottom row of microcapacitors is not visible, indicating that the probe sensitivity has been reduced to 3 fF without the Ti/Al signal pathway. This is further shown via the reduction in $|S_{11}|$ contrast between the larger microcapacitors and the SiO_2 background compared to the Ti/Al-coated NW probe. Fig. 3.5 (c) depicts the $|S_{11}|$ image for the commercial Si cantilever. A continued reduction in sensitivity is seen with the smallest capacitance recorded at 6 fF. Finally, Fig. 3.5 (d) depicts the $|S_{11}|$ image for the commercial NSMM Pt tip. It also recorded all values of microcapacitors and is sensitive down to at least 0.7 fF. From these results, we conclude that the addition of a GaN NW to the Si probe and subsequent Ti/Al coating produce a probe with microwave sensitivity comparable to the commercial NSMM Pt tip.

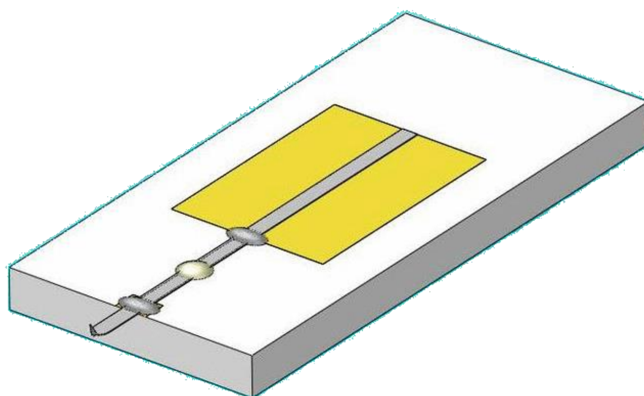

FIG. 3.4 Schematic of microwave probe from Rocky Mountain Nanotechnology and used with Agilent 5400 system. Cantilever is made of platinum and conductively epoxied to the gold pad. Image from reference[122].

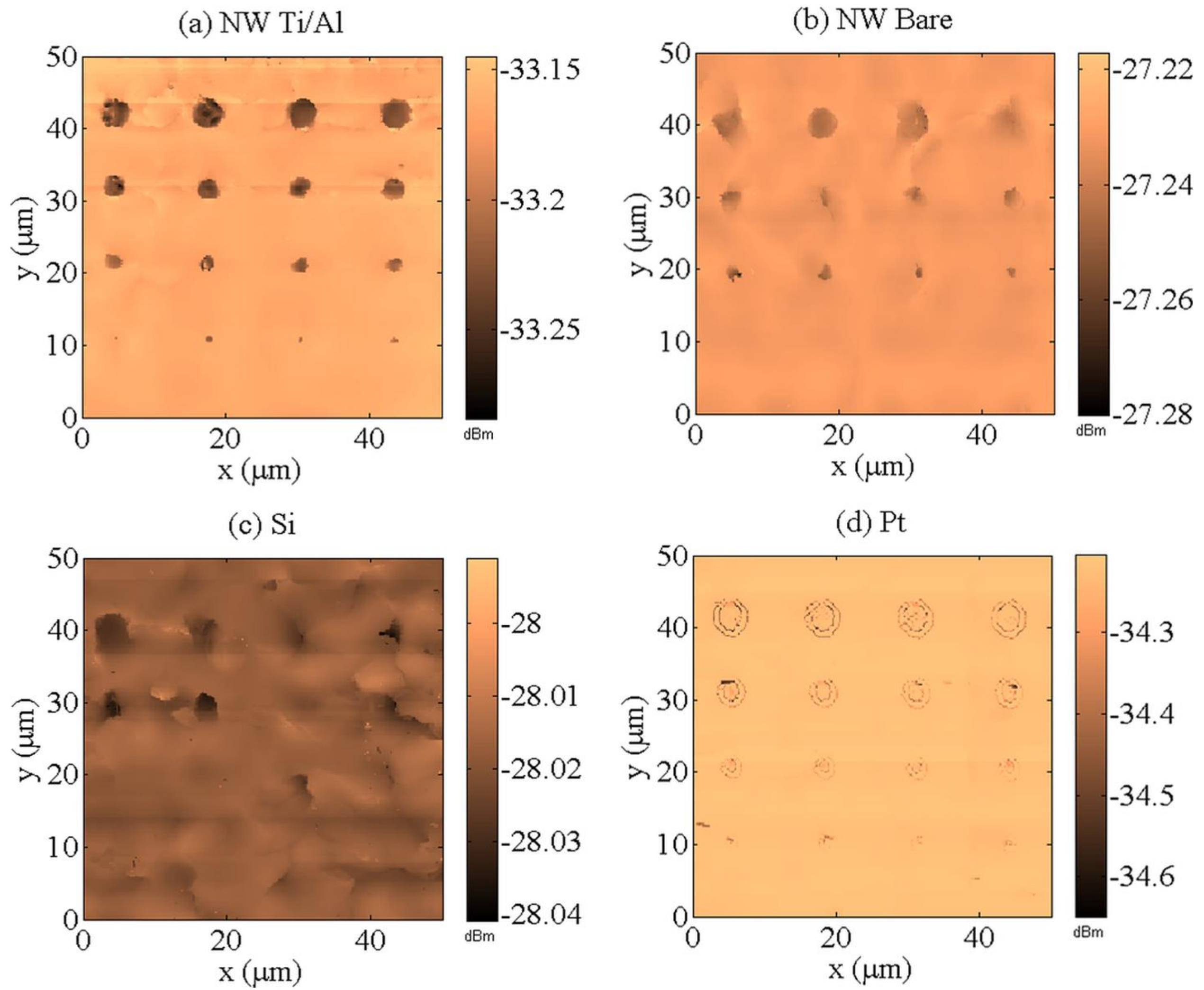

Fig.3.5 (a) Scan results for Ti/Al NW probe over DUT showing change in the amplitude of the microwave reflection coefficient $|S_{11}|$. All microcapacitors are present in the image, indicating sensitivity to at least 0.7 fF. (b) $|S_{11}|$ image with bare NW probe indicates a minimum sensitivity of 3 fF. (c) $|S_{11}|$ image with Si probe indicates a minimum sensitivity of 6 fF. (d) $|S_{11}|$ image with Pt probe indicates a minimum sensitivity of 0.7 fF. All scans are plotted with different Z-axis color scales for clarity.

We can plot more detailed line scans across the top row of large microcapacitors to enable a quantitative comparison of probe performance. These results are shown in Fig. 3.6 below, with the data offset along the Y-axis to facilitate comparison. As expected, the Ti/Al NW probe clearly shows the four microcapacitors in the $|S_{11}|$ line scan in contrast with the bare NW and commercial Si probes. The commercial Pt probe, while showing the largest maximum $|\Delta S_{11}|$, suffers from

inconsistencies in its $|S_{11}|$ readout across each microcapacitor with large spikes and regions of almost no response. This is attributed to the relatively soft Pt tip experiencing difficulty maintaining firm contact with the Ti/Au pad during scanning. Further comparison of probe performance is carried out by looking at the maximum $|\Delta S_{11}|$ and mean $|\Delta S_{11}|$ between each pad and the SiO_2 background, as shown in Fig. 3.7 (a) and 3.7 (b), respectively. The Pt probe once again shows the largest max $|\Delta S_{11}|$, while both the Ti/Al NW and Pt probes demonstrate an increased $|\Delta S_{11}|$ as a function of increasing capacitance. The flat trend demonstrated by the bare NW and Si probes is attributed to the measured values of $|\Delta S_{11}|$ being near the noise floor of the test equipment. In Fig. 3.7 (b), the Ti/Al NW probe has the greatest mean $|\Delta S_{11}|$, with a measurement sensitivity of about twice that of the Pt probe and about four times that of the bare NW and Si probes for the 10 nm-thick microcapacitors. This is coupled with a significantly reduced standard deviation for the Ti/Al NW probe compared with the Pt probe, indicating reduced measurement uncertainty. The Ti/Al NW probe does not show the expected increase in $|\Delta S_{11}|$ signal as a function of increasing capacitance, likely due to small signal variations across each microcapacitor. We will seek to improve upon this in future designs by switching from the evaporated Ti/Al layer to a conductive atomic layer deposition coating to simultaneously improve both NW sidewall coverage and continuity of the microwave signal pathway.

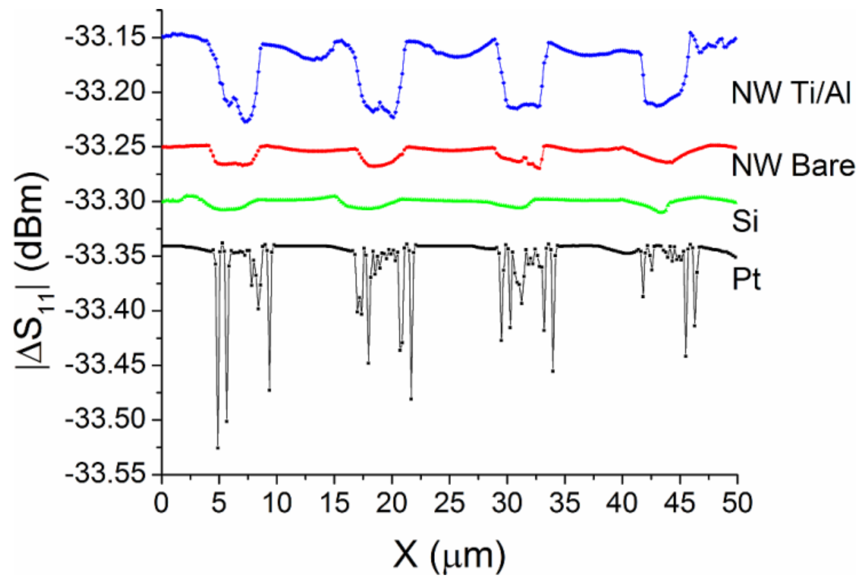

Fig. 3.6 $|S_{11}|$ line scans for each probe over the large 4 μm diameter microcapacitors. The Pt probe shows the highest contrast between the Ti/Au pads and SiO_2 background while also picking up large variability attributed to poor contact between the soft tip and DUT. The data are offset along the y-axis.

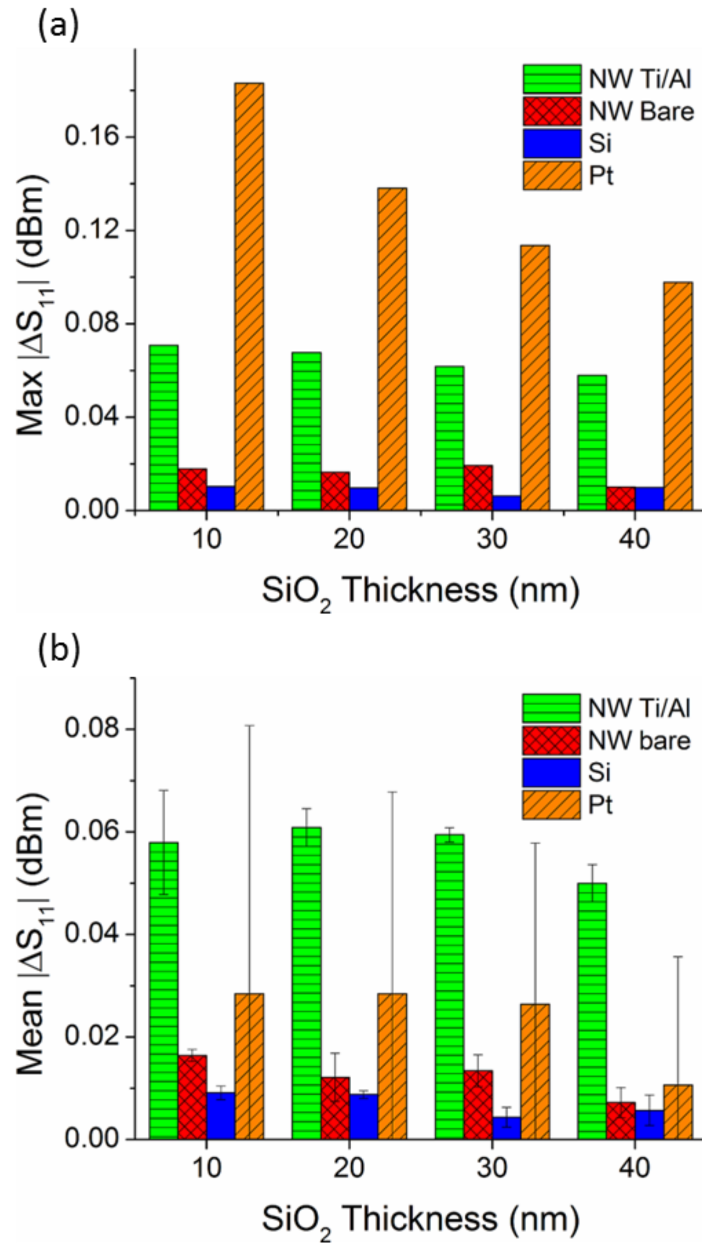

Fig. 3.7 (a) Maximum $|\Delta S_{11}|$ amplitude changes for the 4-μm diameter microcapacitors as a function of SiO_2 thickness. The Pt probe has the highest maximum $|\Delta S_{11}|$ with the Si and bare NW probes near the noise floor. (b) Mean $|\Delta S_{11}|$ amplitude changes for the 4-μm diameter microcapacitors as a function of SiO_2 thickness with respective 95 % confidence intervals. The Ti/Al probe has the highest mean $|\Delta S_{11}|$ across all microcapacitors, followed by the Pt probe.

3.2.4 Topography and Mechanical Wear Results

To evaluate the coated NW probe's overall performance, it is also important to analyze the GaN NW tip's topographical imaging capabilities. Each of the four probes clearly imaged the ~ 220 nm height change between each microcapacitor and the SiO_2 background (Fig. 3.8). More importantly, each probe also detected the 10 nm step in SiO_2 thickness between each microcapacitor. This indicates that the NW probe suffers no vertical resolution loss down to the nanometer scale, while the $|S_{11}|$ line scans in Fig. 3.7 show that it simultaneously improves contact with the sample during microwave scanning. The wear resistance of the coated NW probe was also tested by SEM imaging the tip before and after twelve scans over the microcapacitor DUT. Figure 3.9 (a) shows that the tip radius of the Ti/Al NW probe remains virtually unchanged at 150 nm after multiple scans. By comparison, the same test was also performed with a previously unused commercial Pt tip. Before the 12 scans, Fig. 3.9 (b) shows that the Pt possessed a sharp tip with an approximate 50 nm radius. However, after test completion, Fig. 3.9 (c) shows that the tip was worn, leaving an effective tip with a radius greater than 150 nm. The NW probe's hardness, inherent in its defect-free crystalline structure, enables it to better maintain imaging consistency between scans. Because the tip geometry is robust, the capacitive coupling to the sample remains constant and quantitative measurements can be made repeatedly with no need for re-calibration of the system.

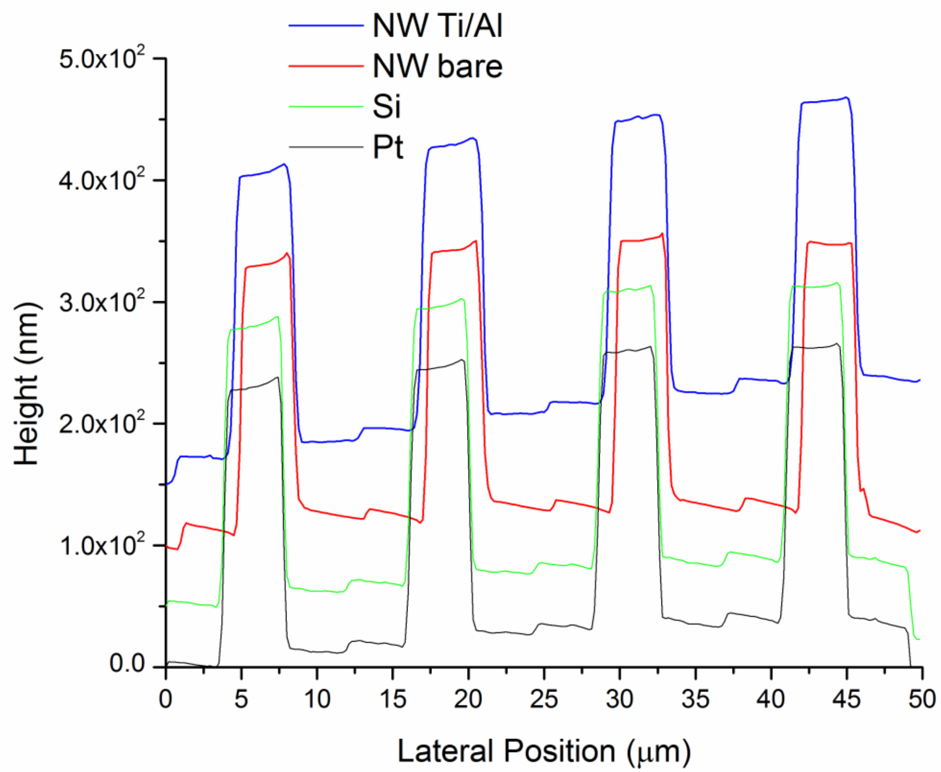

FIG. 3.8 Topography line cuts from each probe across the microcapacitor calibration sample. Each probe was able to detect the 10 nm SiO_2 steps.

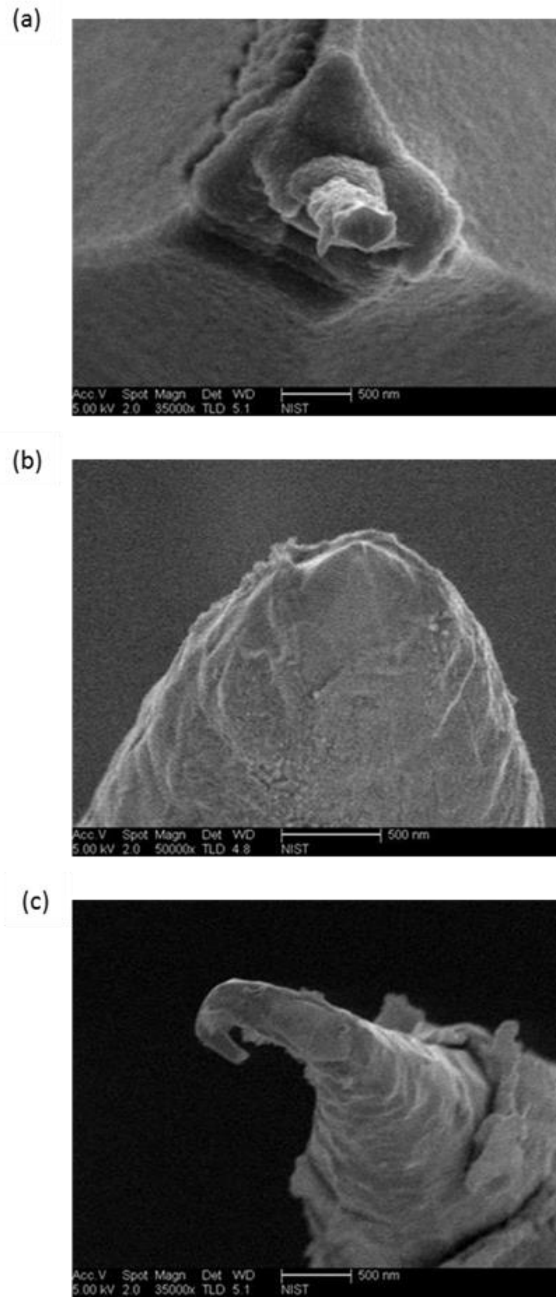

FIG. 3.9 (a) Ti/Al coated NW probe after 12 contact scans. (b) Commercial Pt probe prior to use. (c) Same commercial Pt probe after 12 contact scans.

3.3 Fabrication and Testing of W-ALD NW Probe

3.3.1 Fabrication

In an effort to improve upon the microwave and topographical resolution of the first NW probe, a new probe was fabricated using a process similar to that previously established in Section 3.2. To create a microwave pathway from the AFM chip body to the tip, the entire structure was coated using atomic layer deposition (ALD) with a structure comprised of 30 cycles Al_20_3 (3.5 nm)/ 63 cycles W (25.6 nm)/ 10 cycles Al_20_3 (1.2 nm)[123-125]. The depositions were performed in a viscous flow stainless steel ALD reactor with an inner diameter of ~ 9 in. The body walls of the reactor were held at 130 ^{o}C while the precursor vessels were kept at room temperature. N_2 (ultra-high purity Airgas) was used as the carrier gas, with each precursor line having an N_2 flow of 40 sccm. The Al_2O_3 buffer layer was used to promote W nucleation and was grown using 30 cycles of trimethylaluminum (TMA, Aldrich 97 %) and deionized H_2O. Dose times for both TMA and H_2O were 3 sec, with 55 sec purges in between reactant doses. The resultant Al_2O_3 growth rate was about 1.2 Å/c. The proceeding W layer was grown with 63 cycles of disilane (Si_2H_6, Voltaix UHP Grade 99.998 %) and tungsten hexafluoride (WF_6, Aldrich 99.9 %). Due to the size of the reactor, gas was dosed over a 15 sec interval to ensure good diffusion and followed with a long purge (80 sec after Si_2H_6 and 70 sec after WF_6). WF_6 doses were ~9.6E5 L while Si_2H_6 doses were ~1.8E6 L, resulting in a W growth rate of ~4 Å/c. Finally, a capping layer of 10 c Al_2O_3 was grown on top of the W layer with the same parameters as the buffer layer. The ALD reactions are summarized in Table 3.1 below.

Table 3.1. ALD Surface Reactions

Al_2O_3	A	$AlOH^* + Al(CH_3)_3 \rightarrow AlOAl(CH_3)_2^* + CH_4$
	B	$AlCH_3^* + H_2O \rightarrow AlOH^* + CH_4$
W	A	$WF_5^* + Si_2H_6 \rightarrow WSiF_2H^* + SiF_3H + 2H_2$
	B	$WSiF_2H^* + WF_6 \rightarrow WWF_5^* + SiF_3H$

Deposited thicknesses were independently measured through X-ray reflectivity (Fig. 3.10) while X-ray diffraction data indicated the deposited metal to be comprised primarily of β-phase W (Fig. 3.11)[126]. Figure 3.12 is an SEM image showing the NW probe, post-ALD. The NW protrudes ~6 μm from the Si base and has a radius of ~120 nm. The uniform coverage afforded by ALD enables a continuous electrical pathway free of pinholes and cracks without significantly increasing the mechanical probe radius during scanning.

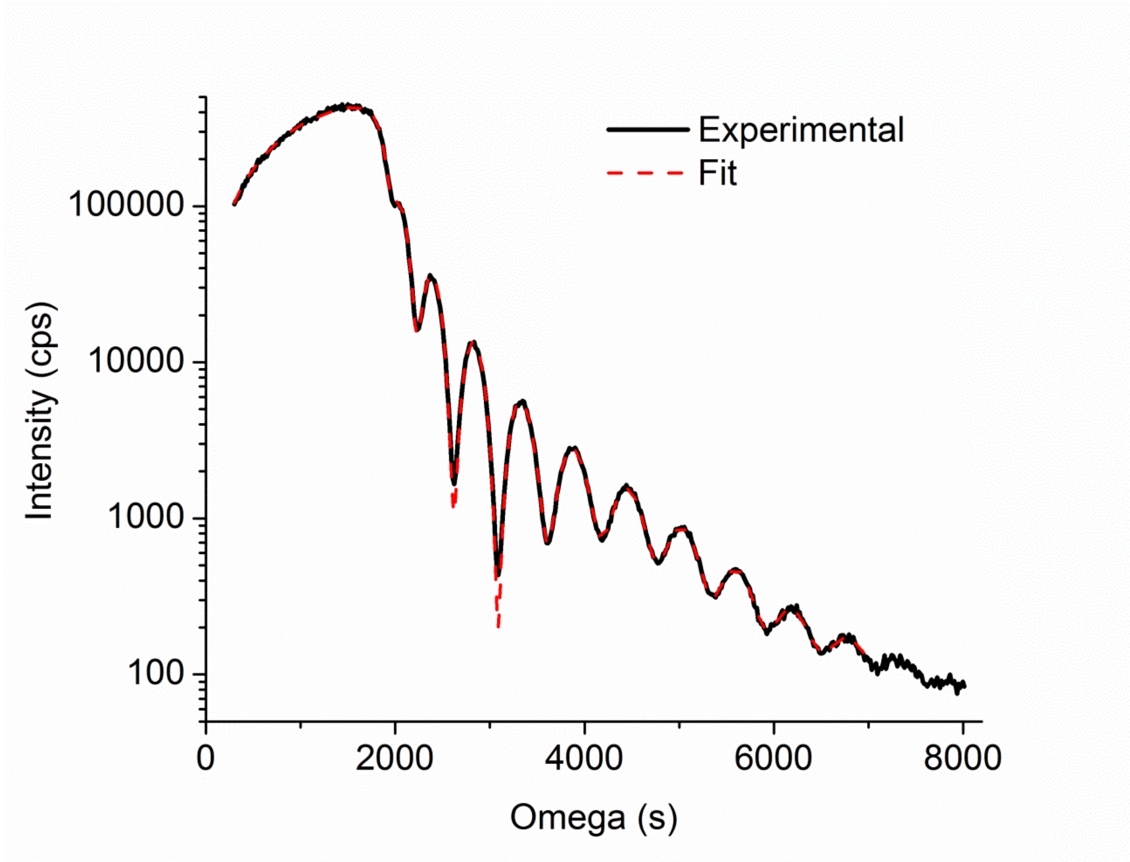

FIG. 3.10 XRR data (black solid line) modeled with interface layers between the Al_2O_3 and W to improve the fit (red dashed line). Resulting thicknesses were found to be 3.5 nm for the Al_2O_3 buffer layer, 25.6 nm for the W layer, and 1.2 nm for the Al_2O_3 capping layer.

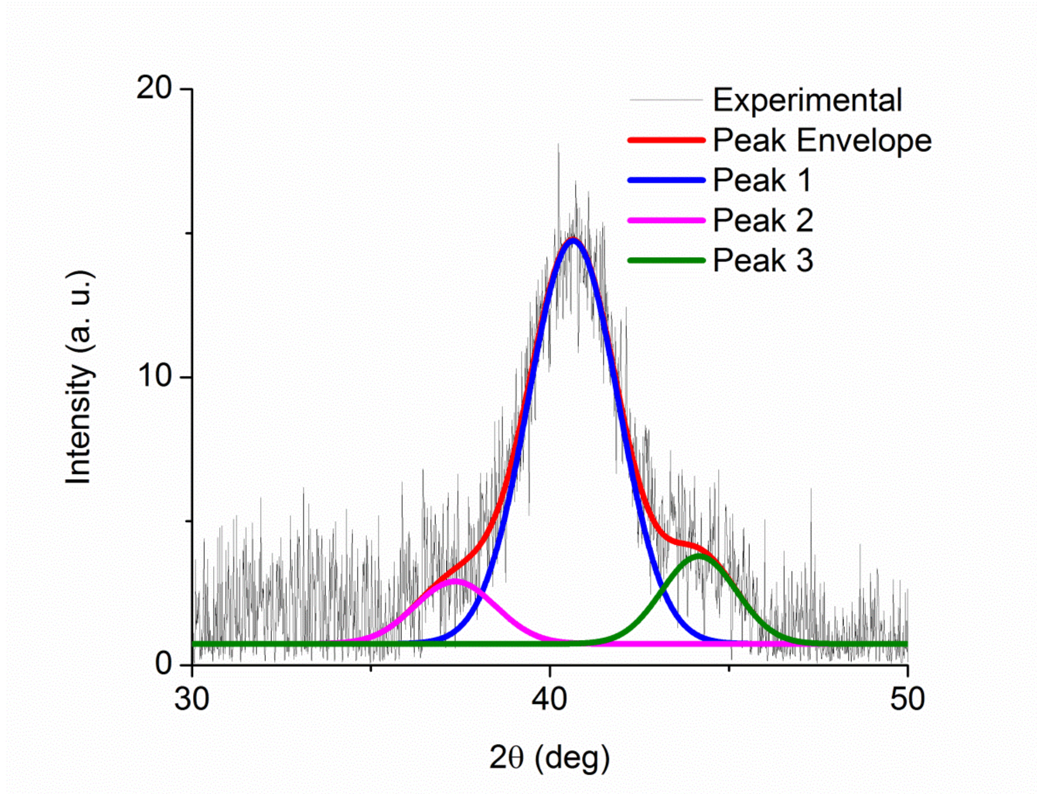

FIG. 3.11 XRD data (black line) with peaks fit to data. The peak envelope is shown with the red line and further broken down into a center peak (blue line), a left peak (magenta line), and a right peak (green line). The presence of a sharp center peak with two additional peaks between 30 deg and 50 deg indicates the ALD resulted in mostly beta-W. The peaks are shifted slightly from the calculated peak positions of 35.3 deg, 39.6 deg, and 43.6 deg. This may be caused by stresses in the deposited film.

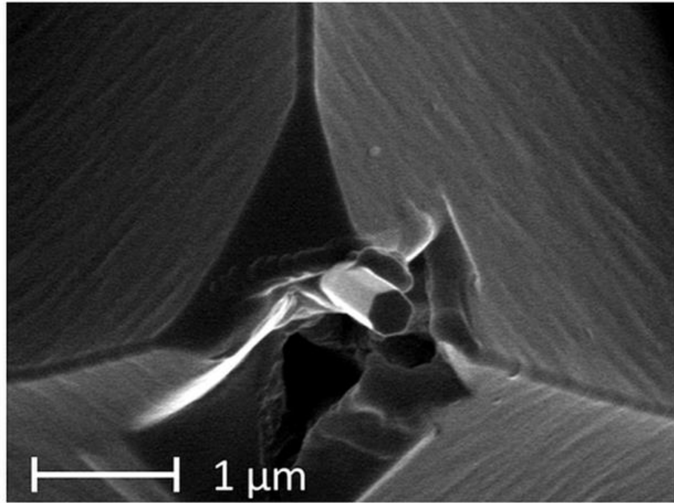

FIG. 3.12 (a) SEM image of fabricated GaN NW probe post W ALD.

3.3.2 Microwave Results and Modeling

The microcapacitor sample was once again used to calibrate the capacitance resolution of the W-ALD NW probe. Prior to scanning, the probe was brought into contact over the 40 nm thick SiO_2 step and the resonance peak was tuned to -50 dBm at a frequency of 2.3 GHz. The VNA measuring frequency was minimum offset and tracked during a 50 μm x 50 μm scan. In Figure 3.13 (a), the improved microwave contrast of the W-ALD NW probe can be clearly seen relative to the original Ti/Al NW probe (Fig. 3.13 (b)). The difference in microwave signal, or $|\Delta S_{11}|$, between each Au microcapacitor pad and the surrounding SiO_2 step on which the pad is located was recorded. Following Ref. 12, the $|\Delta S_{11}|$ data was then converted to capacitance using the relation

$$C_{tot} = \alpha * |\Delta S_{11}| \tag{3.3}$$

and fit with a circuit model. The model consists of stray capacitance caused by the cantilever C_{cant} in parallel with three additional capacitances in series: tip capacitance C_{tip} due to the 12 nm $Al_2 0_3$

ALD passivation layer, dielectric capacitance C_{diel} from the SiO_2 layer under the microcapacitor, and back or parasitic capacitance C_{back} due to fringing effects and depletion in the Si substrate. Because $|\Delta S_{11}|$ data is presented as a difference measurement, effects due to the largely constant C_{cant} may be ignored. C_{back} is treated as a fitting parameter that scales relative to the area of the microcapacitor in question with values on the order of 0.3 fF. C_{tip} and C_{diel} are modeled as simple parallel plate capacitors governed by

$$C_{tip} = \frac{\varepsilon_{tip} A_{tip}}{t_{tip}} \quad 3.4$$

$$C_{diel} = \frac{\varepsilon_{diel} A_{diel}}{t_{diel}} \quad 3.5$$

$$\frac{1}{C_{tot}} = \frac{1}{C_{tip}} + \frac{1}{C_{diel}} + \frac{1}{C_{back}} \quad 3.6$$

where A_{tip} is the area of the NW surface, A_{diel} is the area of the microcapacitor, t_{tip} is the thickness of the outer Al_2O_3 ALD layer, t_{diel} is the thickness of the SiO_2 layer, ε_{tip} is the permittivity of Al_2O_3, and ε_{diel} is the permittivity of SiO_2. To obtain the plot shown in Fig. 3.14, the model was fit to the experimental data for the 3.1 μm^2 microcapacitors with $\alpha = 0.5$ fF/|ΔdBm|. The α and C_{back} fitting parameters were held constant and applied to the other three microcapacitor sizes. As expected, increasing microcapacitor area and decreasing dielectric thickness correlate with an increase in measured total capacitance. The capacitance model tracks these trends well with deviations likely attributed to error caused by fringe effects in the parallel plate capacitors and a variable C_{tip} due to bending of the NW during scanning.

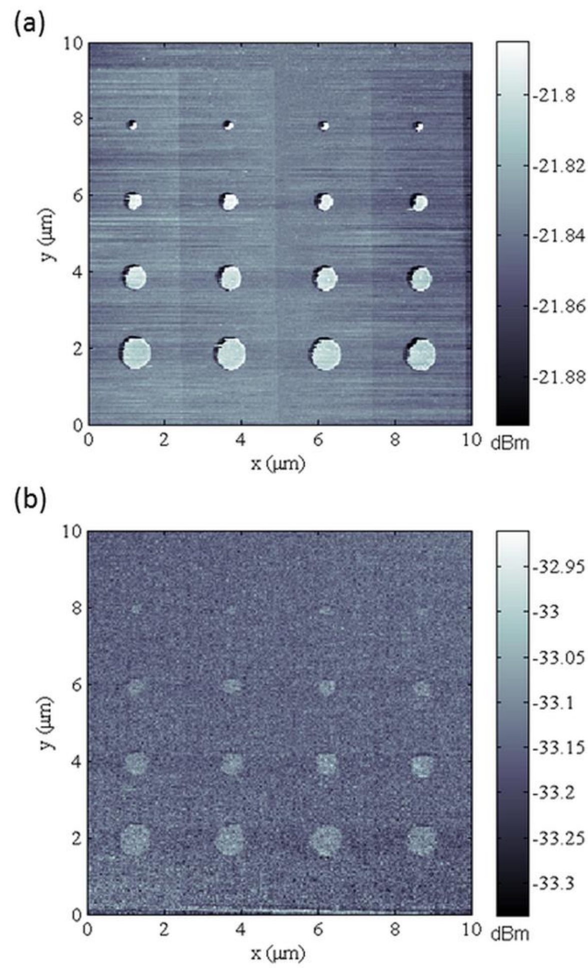

FIG. 3.13 (a) Microwave reflection coefficient S_{11} image taken with the W-ALD NW probe showing contrast for both the microcapacitors and SiO_2 steps. (b) S_{11} image taken with the Ti/Al NW probe reported in Ref. 20. SiO_2 steps are not visible while microcapacitor edge resolution is reduced.

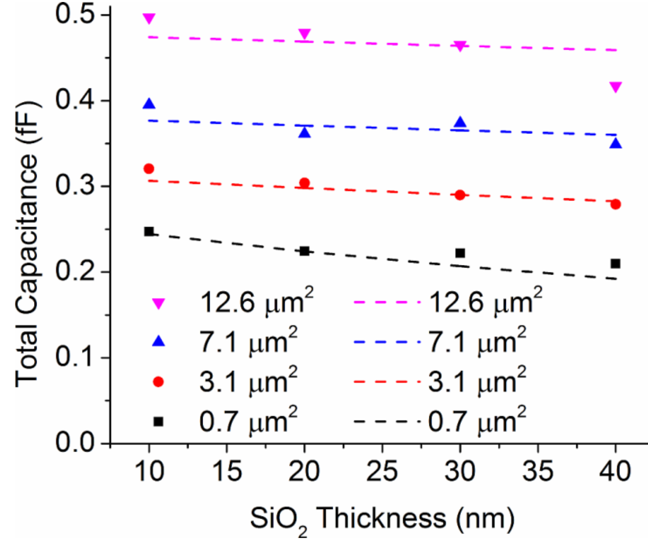

FIG. 3.14 $|\Delta S_{11}|$ between each microcapacitor and background SiO_2 converted to capacitance and plotted as a function of SiO_2 thickness (solid symbols). Experimental data for 3.1 μm^2 microcapacitors was fit (dashed lines) using C_{back} and α as fitting parameters. These parameters were then held constant for the other three microcapacitor areas shown.

To determine the resolution limit and measurement noise floor attributed to the W-ALD NW probe and microscope, a line scan across the SiO_2 steps without the presence of microcapacitors was taken. Here, the total capacitance model is reduced to C_{cant} in parallel with C_{tip} and C_{step} in series. C_{tip} is once again modeled as a simple parallel plate capacitor and retains the same value from the model presented above. C_{step}, however, must account for fringing effects as the ratio of the parallel plate radius (tip radius) R to half the dielectric SiO_2 thickness d ranges from 6 – 12. An empirical equation derived from the Kirchhoff-Hutson expression with error < 1% when compared to numerical simulations for this R/d range was used[127]:

$$\frac{C_{diel}}{C_{elem}} \approx 1 + \frac{2d}{\pi R} ln \frac{8\pi R}{ed} + (\frac{d}{\pi R} ln \frac{d}{8\pi R})^2 \qquad 3.7$$

$$C_{tot} = \left[\frac{1}{C_{tip}} + \frac{1}{C_{diel}}\right]^{-1} + C_{cant} \qquad 3.8$$

where C_{elem} is the parallel plate model, d is half the SiO_2 thickness, e is the permittivity of free space, and R is the NW radius. From Fig. 3.15, it can be seen that the SiO_2 steps are at the measurement threshold for the W-ALD NW probe because 10 nm changes in SiO_2 thickness correspond to a ~0.03 fF change in capacitance, with measurement noise for each step also corresponding to ~0.03 fF. C_{cant} was determined by measuring $|S_{11}|$ as a function of tip-sample separation with a 2 μm approach curve. By this method, the stray capacitance contribution of C_{cant} was found from a linear relation to be 0.6 ± 0.04 aF/nm, indicating that each 10 nm increase in topography due to the SiO_2 staircase results in a ~6 aF decrease in C_{cant}. Because this contribution is approximately one order of magnitude smaller than the measurement resolution of our system, C_{cant} was once again determined to be negligible and omitted from the model. Using the same value of α = 0.5 fF/|ΔdBm| previously calculated, the model provides a reliable first order approximation for the SiO_2 steps across the thicknesses measured and agrees with the experimental data to within 10 %, as shown in Figure 3.15. Improvements can be further made to the fit by decreasing the value of C_{tip}. This is attributed to the likely case where the NW end facet is not flush with the sample during scanning, resulting in a reduced contact area and an increased effective dielectric thickness.

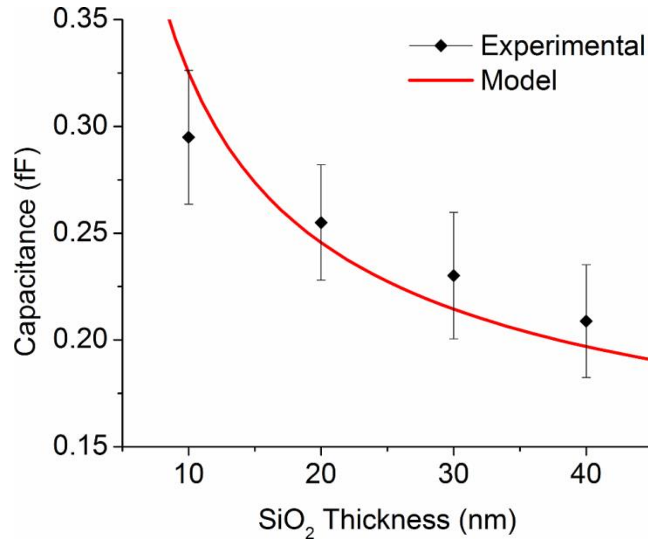

FIG. 3.15 Measured capacitance of each SiO_2 step (black diamonds). Error bars represent measurement noise during scanning across each step. Data is fitted with a capacitance model with fringe capacitance across the SiO_2 layer taken into account.

3.3.3 Imaging MoS_2 Sample

To further assess the performance of the W-ALD NW probe, we compared its topographical and microwave resolution against that of the commercial Pt NSMM probe. We chose a MoS_2 sample for imaging measurements due to its potential applications in CMOS-like logic devices and as a transparent semiconductor in photovoltaic and other optoelectronic structures[128-129]. MoS_2 is a member of the layered transition-metal dichalcogenide materials with crystals comprised of vertically stacked layers held together by van der Waals forces. Unlike pure graphene, MoS_2 is a direct bandgap semiconductor (1.8 eV) and thus a candidate for replacing Si in transistor designs without the need for increased fabrication complexity. One- to four-layer-thick MoS_2 was extracted from a bulk sample using the Scotch Tape method and then deposited on 260 nm of SiO_2 grown on a p-type Si wafer[130]. Both probes were scanned over the same MoS_2 patch at ~2.3 GHz and with a scan area of 10 μm x 10 μm. Figure 3.16 (a) shows the topographical results for the W-

ALD NW probe. The different layers (each 6.5 Å thick) are clearly visible with sheet edges well defined. By comparison, in Fig. 3.16 (d), the topographical results for the Pt probe are shown, and the sheet edges are no longer sharp while the single layer region is poorly resolved. In Fig. 3.16 (b) and 3.16 (c), the amplitude and phase components of the microwave reflection S_{11} are shown for the W-ALD NW probe. Both single and multilayer MoS_2 sheets are clearly visible in the S_{11} amplitude and phase images. The dashed white oval highlights the transition from one- to two-layer MoS_2, which can be seen in all three W-ALD NW image modes. The physics underlying the microwave contrast in the MoS_2 sample will be explored in depth in an upcoming publication. Figures 3.16 (e) and 3.16 (f) show the amplitude and phase results respectively for the Pt tip. These images are set to the same intensity scale as the W-ALD NW results, allowing for a direct comparison between the image contrasts. Although it maintains good multilayer edge resolution, phase contrast is reduced with a loss of sensitivity to the single-layer MoS_2 sheet. Furthermore, amplitude sensitivity is almost completely eliminated in the case of the Pt tip with measurement noise dominating the scan.

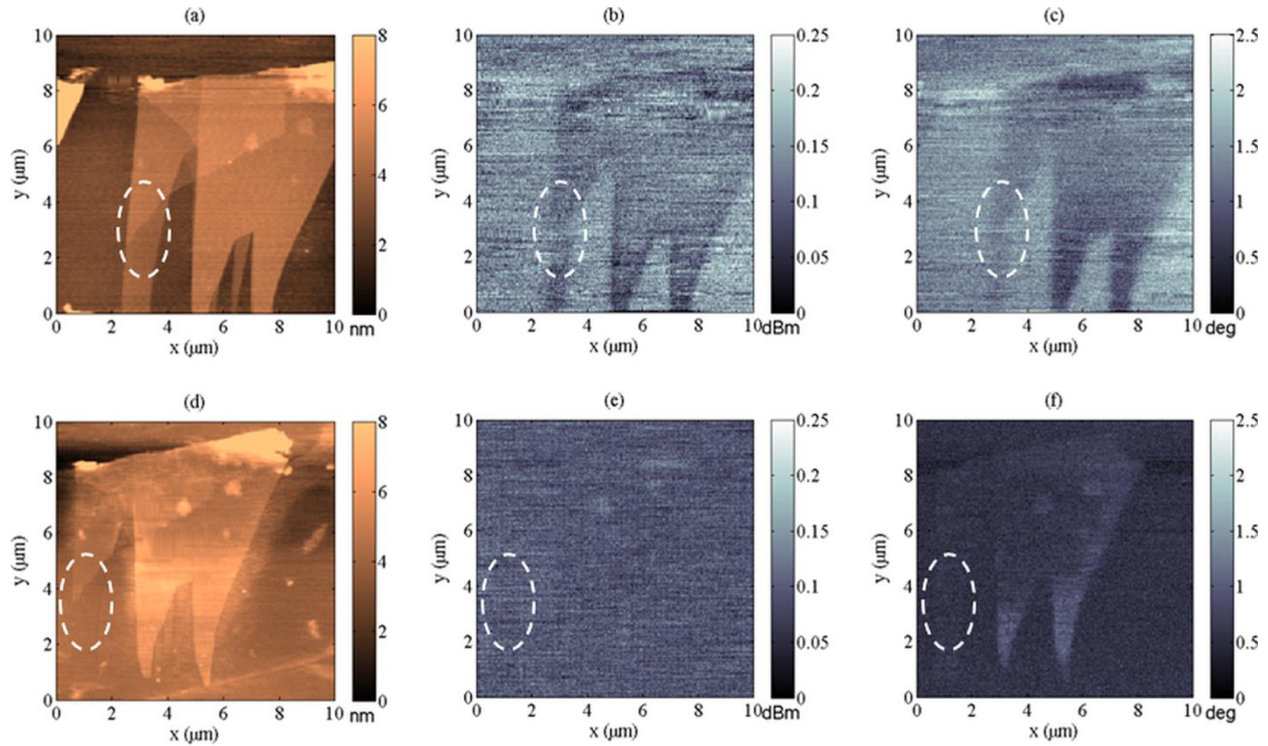

FIG. 3.16 (a) Topography of MoS_2 sample with W-ALD NW probe showing high edge definition. (b) and (c) $|S_{11}|$ amplitude and phase, respectively, with W-ALD NW probe with sensitivity to both the one- to two-layer transition (dashed white oval) and internal inhomogeneities within the MoS_2 sheets. (d) Topography result from commercial Pt probe showing reduced edge definition and lack of sensitivity to the single layer region. (e) and (f) $|S_{11}|$ amplitude and phase, respectively, from the commercial Pt probe with only minimal contrast present in the phase image.

The MoS_2 sample was further examined in an effort to determine the cause of varying resolution between the two probes. For the above data, the MoS_2 was imaged first by the commercial Pt probe before being scanned by the W-ALD NW probe. Figure 3.17 (a) shows a follow up topography scan with the Pt probe showcasing improved edge definition and single layer contrast. Line cuts of 2.5 μm across the single layer region (solid white line) and across the multilayer-SiO_2 region (dashed white line) were taken from the same area for each of the three topography scans. The results are shown in Fig. 3.17 (b) and 3.17 (c), respectively. In Fig. 3.17 (b), the top line scan (black) represents the first Pt probe result which exhibits no obvious topographical sensitivity to the single layer region. The middle line scan (red) represents the W-ALD NW probe, and here the

single layer region is clearly shown with a lateral resolution of ~100 nm for the 6.5 Å step. The bottom line scan (blue) represents the final Pt probe scan. Sensitivity to the single layer region is now improved with a lateral resolution of ~400 nm. In Fig. 3.17 (c), the line cuts produce a similar trend across the multilayer region. The W-ALD NW probe once again yields the cleanest edge definition followed by the second of the two Pt probe scans.

These line cuts indicate that the MoS_2 sheets have a glue residue from the scotch-tape on their surface. During scanning with the Pt probe, this residue results in a convolution between the topographical amplitude and phase as the cantilever rotates out of plane, subsequently reducing sensitivity to the MoS_2 edge boundaries. Because these scanning artifacts are reduced after the W-ALD NW probe imaging, we attribute the improvement in sensitivity observed with the commercial probe to "cleaning" of the sample surface through the removal of portions of the glue residue. It is important to note that the sample was scanned first with the Pt tip ten times with no apparent change in topography while the first scan with the W-ALD NW probe yielded the resolution shown in Fig. 3.16 (a). This indicates that the Pt probe performed negligible cleaning, if any, of the sample over the course of repeated scanning. Furthermore, the W-ALD NW probe still exhibits the highest contrast relative to either Pt probe result with a lateral resolution on the order of its tip radius, indicating that its flexible, high-aspect ratio structure is relatively immune to any remaining glue residue, while providing a stable, uniform tip geometry that enables enhanced microwave contrast.

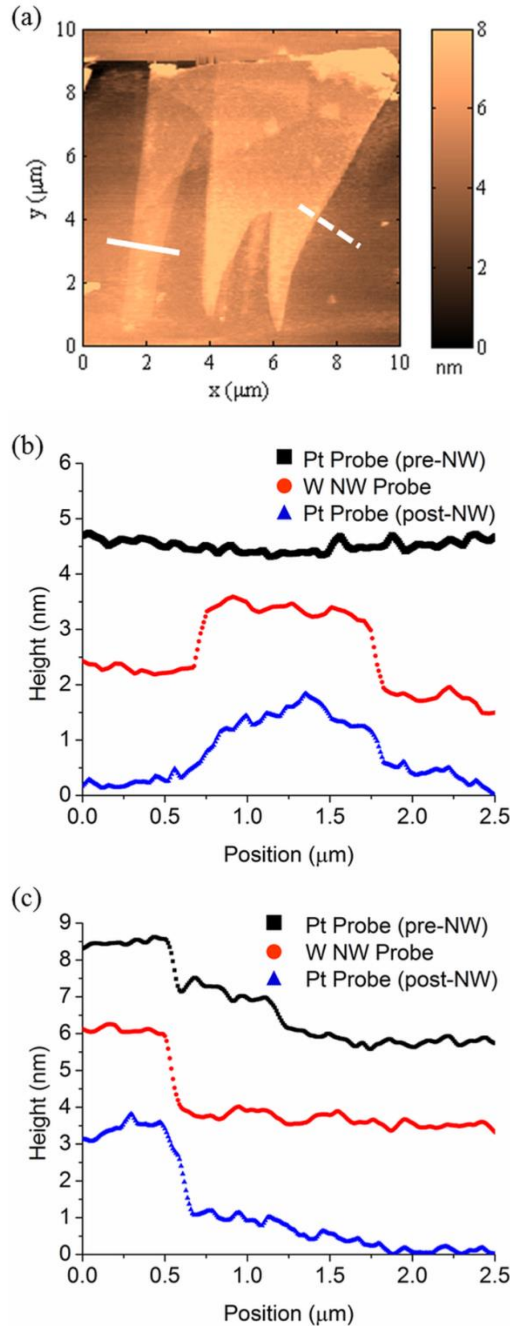

FIG. 3.17 (a) Topography image from commercial Pt probe after W-ALD NW scan. Line cuts of 2.5 μm are taken across the single layer region (solid white line) and the multilayer region (dashed white line). (b) and (c) Results from single layer and multilayer regions, respectively, with the top black line representing the Pt probe topography data before the W-ALD NW probe scan, the red line representing the W-ALD NW probe, and the blue line representing the Pt probe after the W-ALD NW probe scan. The latter Pt probe line cuts reveal an improved sensitivity to the MoS_2 edge, owing to a reduction in presence the of glue residue. Note: line scans have been offset along the y-axis for viewing clarity.

Chapter 4

Conclusions and Future Work

CONTENTS

4.1 Summary and Contributions 122

4.1.1 Applying NSMM to Photovoltaics 122

4.1.2 Novel GaN NW Probe for NSMM 123

4.2 Future Work 125

4.2.1 Wafer-Scale Fabrication of NW Probes 125

4.2.2 Development of a p-n Junction LED Multi-Probe 128

4.2.3 Application of NW NSMM Probes to Biological Samples 131

4.1 Summary and Contributions

4.1.1 Applying NSMM to Photovoltaics

We developed a home-built NSMM suitable for imaging photovoltaic structures. The STM-feedback system was improved through the use of a glue-free tuning fork feedback system capable of operating on conducting, semiconducting, and insulating materials. More importantly, the tuning fork enabled the system to maintain feedback under both dark and illuminated conditions, enabling characterization of photovoltaics without interference from a laser beam-bounce system. Height profile measurements, where Δf was tracked as a function of tip-sample distance, were performed on Cu, Si, GaAs, and CIGS samples. Results on Cu indicated that temperature effects from the laser diode were negligible. First order models were fit to the semiconductors, providing an approximation for their change in carrier concentration under 405 nm illumination. The CIGS sample was further analyzed for conductivity changes under 405 nm, 680 nm, 808 nm, and 980 nm illumination. The results compared favorably against a wavelength-dependent quantum efficiency curve taken at NREL. Finally, we performed the first NSMM measurements on an inhomogeneous photovoltaic. On a high-efficiency CIGS sample, we obtained sub-micron topographical, DC, and $|S_{11}|$ images under both dark and 405 nm illuminated conditions. As expected, topographical features were unaffected through illumination. The DC and $|S_{11}|$ images, however, showed a reduction in sensitivity to grains within the sample. This effect was attributed to the presence of additional photo-generated charge carriers reducing local depletion regions commonly found at CIGS grain boundaries.

Contributions from this section are laid out below:

- Development of a glue-free tuning fork feedback system that enables easy tip-replacement.
- Modeling of height-profile measurements on photovoltaic samples.
- Wavelength-dependent $|\Delta S_{11}|$ sensitivity of high-efficiency CIGS sample.
- Sub-micron imaging of inhomogeneous CIGS photovoltaic sample.
- Illumination-dependent sensitivity to depletion regions owing to photo-generated charge carriers.

4.1.2 Novel GaN NW Probe for NSMM

We have reported on the design and fabrication of GaN NW probes suitable for NSMM. The probes were manufactured by using a FIB to micromachine commercial Si cantilevers so that a single NW could be placed perpendicular to the existing Si tip. A microwave pathway was established through either the evaporation of Ti/Al or ALD of W, making the probe compatible with a commercial Agilent NSMM. Through testing over a microcapacitor calibration sample, the capacitive resolution of the Ti/Al and W-ALD probes were found to be ~0.7 fF and ~0.03 fF, respectively. This compared favorably with the ~0.07 fF resolution of a commercial Pt probe widely used in the field. In addition to improved sensitivity and a reduction in measurement uncertainty, the GaN NW tip also exhibited improved wear resistance during contact scanning. It was found to maintain a constant tip radius on the order of 100 nm – 150 nm, depending on the NW used, after repeated measurements. Under similar scanning conditions, the commercial Pt tip experience a 3x increase in tip radius from 50 nm to >150 nm, thereby reducing certainty in any

quantitative calibrations made prior to measurement. Additional scanning over 2-D MoS_2 films indicate that GaN NW probes, owing to their flexible, high-aspect ratio structure, are resistant to topographical artifacts caused by surface contamination. This further improves their microwave and topographical resolution with regards to traditional cone-shaped probes when characterizing advanced materials.

Contributions from this section are laid out below:

- Description of FIB fabrication techniques necessary to produce a NW probe.
- Determination of effective electrical pathways from the NSMM circuitry to the probe tip.
- Improved microwave and topographical resolution with regard to commercial Pt probe.
- Reduced measurement uncertainty with regard to commercial Pt probe.
- Improved wear resistance during contact mode scanning with regard to commercial Pt probe.
- Modeling of probe-microcapacitor sample interaction presented.

4.2 Future Work

4.2.1 Wafer-Scale Fabrication of NW Probes

While our previous work focused on creating individual probes by inserting a single NW into a FIB-drilled hole on a Si cantilever, recent progress in selective GaN NW growth at NIST will enable wafer-scale production of NW probes, making them a viable candidate for commercial-scale production[116, 131] (Fig. 4.1). The process involves growing a 50 nm AlN buffer layer on a Si wafer to prevent nitridation of the wafer and interdiffusion of Ga and Si. A 75 nm Si_3N_4 layer is grown over the buffer layer and patterned. Upon being placed back in the MBE, GaN NWs are selectively grown only in regions of exposed AlN. The NW's diameter conforms to the hole etched into the Si_3N_4 layer while the growth time determines the NW length. In this way, the resultant location and mechanical properties of the NW (i.e. stiffness) can be controlled. The proposed wafer-scale process is detailed below (Fig. 4.2):

1. Start with 300 μm thick, 76.2 mm diameter, <100>, n-type, double-sided polished wafer
2. 2 μm frontside boron diffusion in furnace to define device layer
3. 50 nm AlN buffer layer grown in MBE followed by 100 nm Si_3N_4 mask
4. Define cantilever and chip body with 50 nm backside RIE etch on Si_3N_4
5. Define break-off tabs with 50 nm backside RIE etch on Si_3N_4
6. 150 μm backside KOH etch on Si followed by 50 nm RIE backside etch on Si_3N_4
7. 148 μm backside KOH etch on Si until reaching boron-doped etch stop
8. Lithographically define NW growth hole and cantilever with frontside RIE etch on Si_3N_4
9. Protect NW growth hole with resist and etch exposed Si_3N_4 and AlN with RIE
10. Etch through boron-doped Si while simultaneously removing resist with frontside RIE

11. Grow GaN NW with MBE and coat with conductive ALD layer

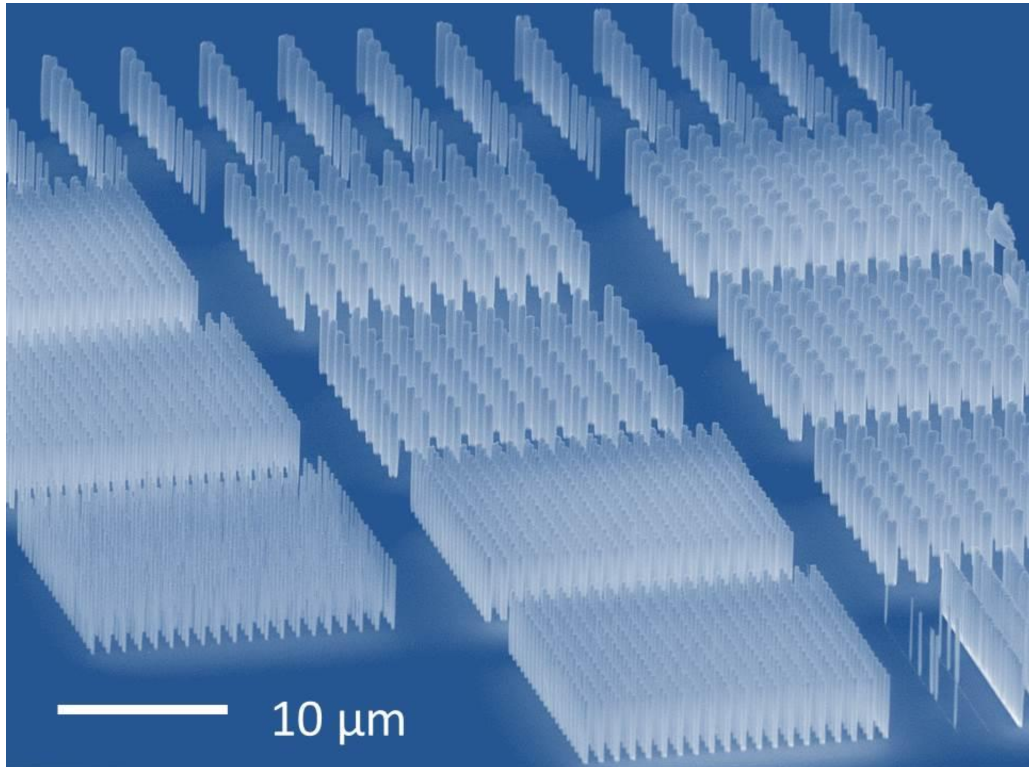

FIG. 4.1. Selective epitaxial growth of GaN nanowires through openings in a SiN_x mask covering an AlN buffer layer. The cross sections are equilateral hexagons with diameters that track the size of the mask opening. Figure from reference[116].

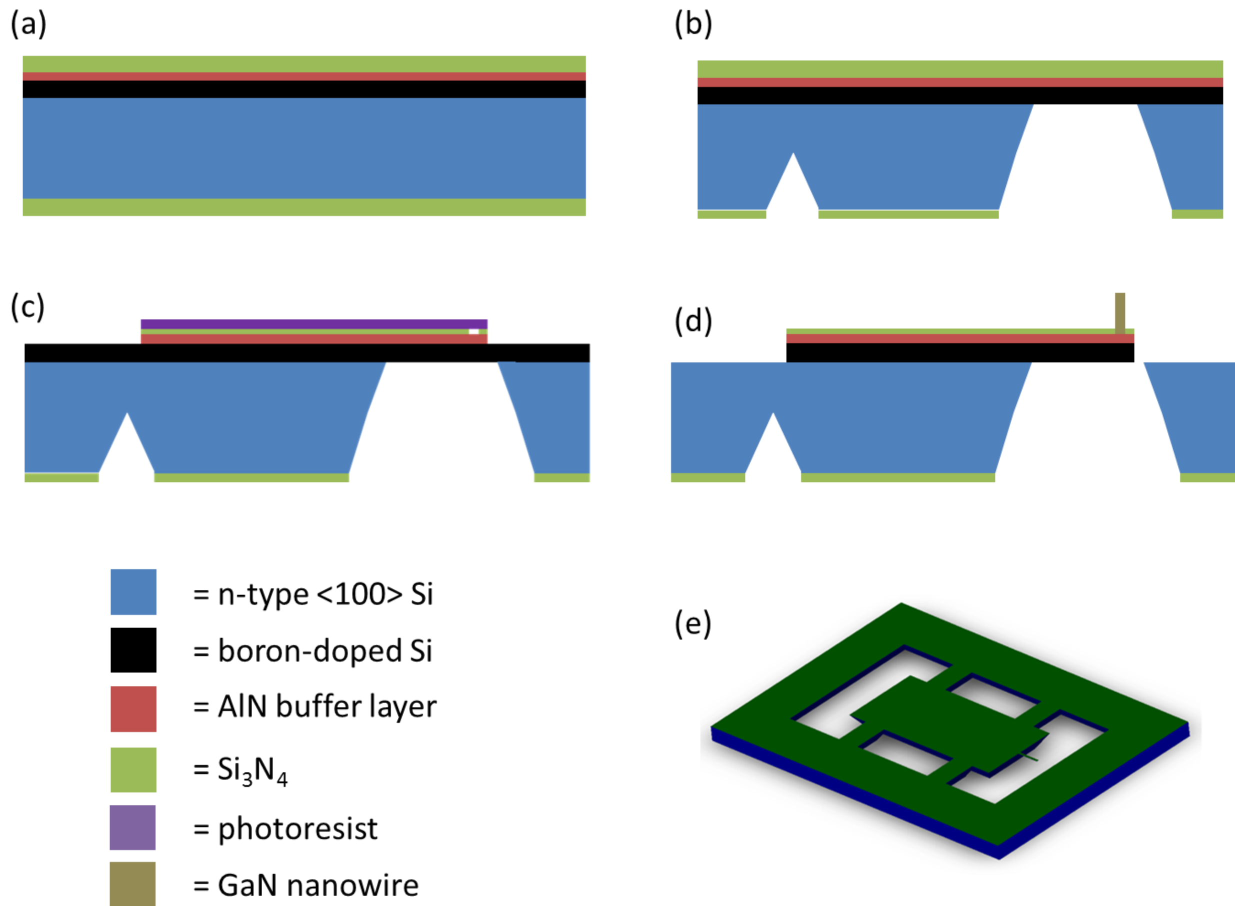

FIG. 4.2. (a) Preparation of wafer (steps 1-3). (b) Define device with backside etching (steps 4-7). (c) Define device through frontside etching (steps 8-10). (d) Growth of NW (step 11). (e) Completed probe with breakoff tabs.

By implementing a wafer-scale fabrication process, we will be able to manufacture hundreds of GaN probes simultaneously. This will open up avenues for novel probe designs including the development of a multi-probe discussed in Section 4.4. A comprehensive study analyzing the effects of nanowire diameter and length on capacitance resolution and stray capacitance, respectively, will be possible by controlling the growth time and mask parameters on each wafer. By reducing the time and cost associated with the fabrication of each individual probe, GaN NW probes for NSMM and other microscopy techniques will ideally become a financially viable alternative to current commercial probe designs.

4.2.2 Development of a p-n Junction LED Multi-Probe

GaN NWs also serve as an ideal platform for continued multi-function probe advancements beyond NSMM and AFM. Introduction of p-type and n-type dopants during the growth process enables the formation of either a lateral or core-shell p-n junction GaN NW. Biasing these two regions results in electroluminescence with an emission wavelength predominantly between 365 nm – 370 nm[132]. At NIST, two p-n junction GaN NWs have been used to demonstrate an on-chip optical interconnect[133]. By establishing a wafer-scale process with selective growth of GaN NWs, electrical contacts could be made via a lithographic process to a p-n junction NW tip. The natural waveguide properties of a NW would enable tip light emission, resulting in a contact-mode capable near-field scanning optical microscope (NSOM)[134]. As opposed to current state-of-the-art designs dependent on fiber optic cables or hollow Si AFM tips, a GaN NW-based NSOM probe could achieve higher resolution coupled with a significant improvement in wear resistance. A combined NSOM, NSMM, and AFM probe could more thoroughly characterize surface and sub-surface properties of advanced materials and biological samples at the nanoscale.

Work on the fabrication of a single GaN NW multi-probe has already begun in conjunction with Paul Blanchard and Shannon Duff at NIST. A forest of lateral p-n junction nanowires was grown in the MBE. The transition to p-type GaN correlates with a morphology change in the NW: the p-type side is short and relatively thick while the n-type side is thinner with a decreasing NW radius near the root. The NWs were first suspended in isopropanol through sonication before being deposited on a pre-patterned wafer using a microliter dispenser. Prior to deposition, 250 nm Ti contacts were evaporated onto the wafer to prevent the NWs from becoming stuck to the Si surface due to Van der Waals forces. Post-deposition, the contacts were again covered in a 20 nm Ti/ 200 nm Al layer. As is shown in Fig. 4.3(a), some NWs were randomly positioned such that two of these contacts aligned with their p- and n-type regions. These NWs were located using the SEM housed within the FIB and then removed from the wafer with a small Pt bond from the FIB's

nanomanipulator (Fig. 4.3(b)). Separately, a commercial tipless Si cantilever was prepared to allow separate electrical pathways to the p-n junction. A 600 nm thick SiO_2 wet oxide layer was thermally grown on the 1 μm cantilever, as is shown in Fig. 4.3(c). The top side was then evaporated with a 20 nm Ti/ 200 nm Au coating. The p-n junction of the NW was then placed at the lower SiO_2 layer while Pt bonds were formed connecting the n-type region to the Si and the p-type region to the Ti/Au layer (Fig. 4.3(d)). Initial I-V testing via a probe station indicated that the multi-probe experienced shorting between the Si and Ti/Au layers. This can likely be attributed to damage to the cantilever structure from handling with tweezers between the oxide growth and metal evaporation stages (Fig. 4.4). To correct this problem in the next round of fabrication, the cantilever sides will be coated with a non-conductive epoxy after the oxide growth. This will ideally eliminate direct contact between the Ti/Au and Si electrical pathways and enable current to reach the NW tip.

Beyond verifying successful emission of light from the p-n GaN NW through the use of a probe station, we will also seek to test its performance as a scanning probe tip. With the metal clip shown in Fig. 3.2 serving as the connection to the Ti/Au and p-type electrical pathway, the Agilent NSMM will be further modified to include an additional metal connection for the underside of the cantilever body to the Si/ n-type electrical pathway. The detector NW from the optical interconnect sample reported on in reference [132] will serve as a test sample. By scanning the multi-probe over the sample, we will be able to synch the signal output of the detector NW with the spatial location of the probe. As such, we can track intensity changes across the scan and correlate them to a topographical read out. At the same time, we can perform microwave measurements that will enable imaging contrast between the p- and n-type regions of the detector NW.

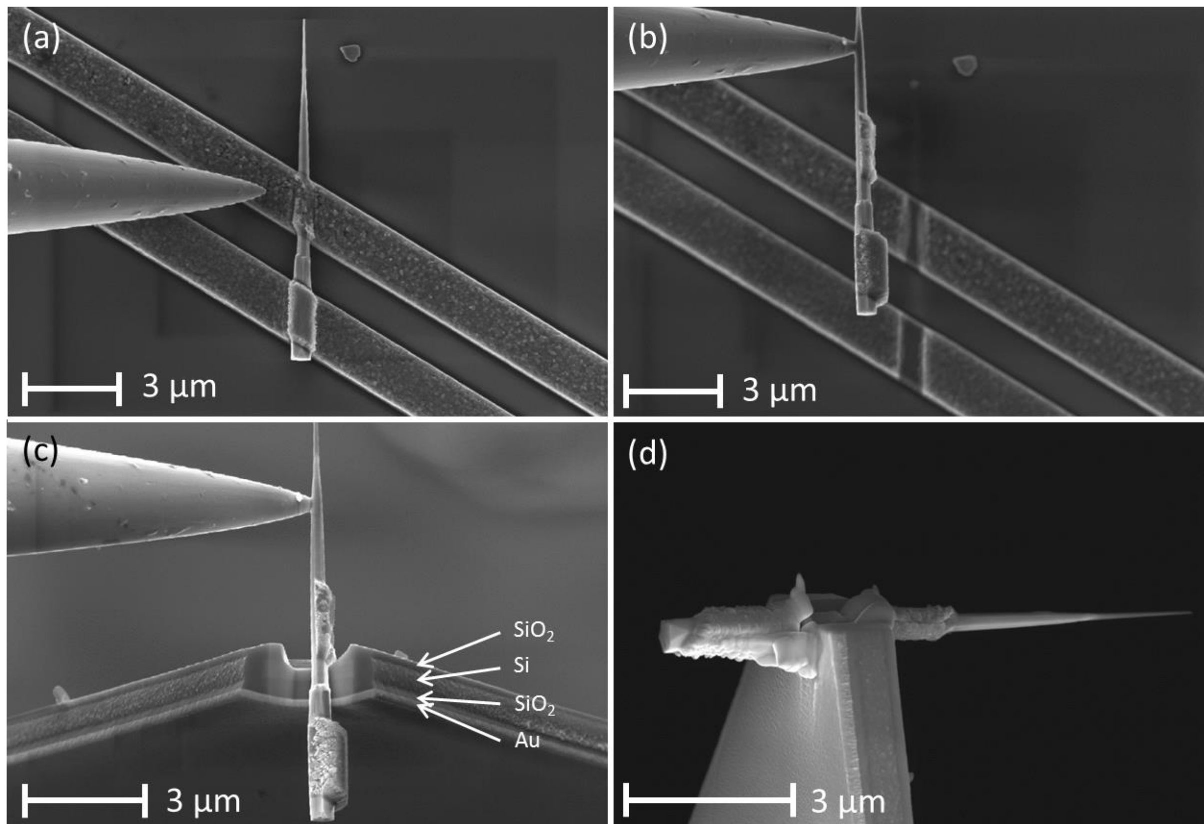

FIG. 4.3. (a) p-n GaN NW dispersed on wafer with Ti/Au contacts. (b) Removal of NWs with electrical contacts via nanomanipulator. (c) Tipless Si cantilever with SiO_2 thermally grown layer and Ti/Au evaporated contact. (d) Final p-n junction multi-probe with Pt contacts.

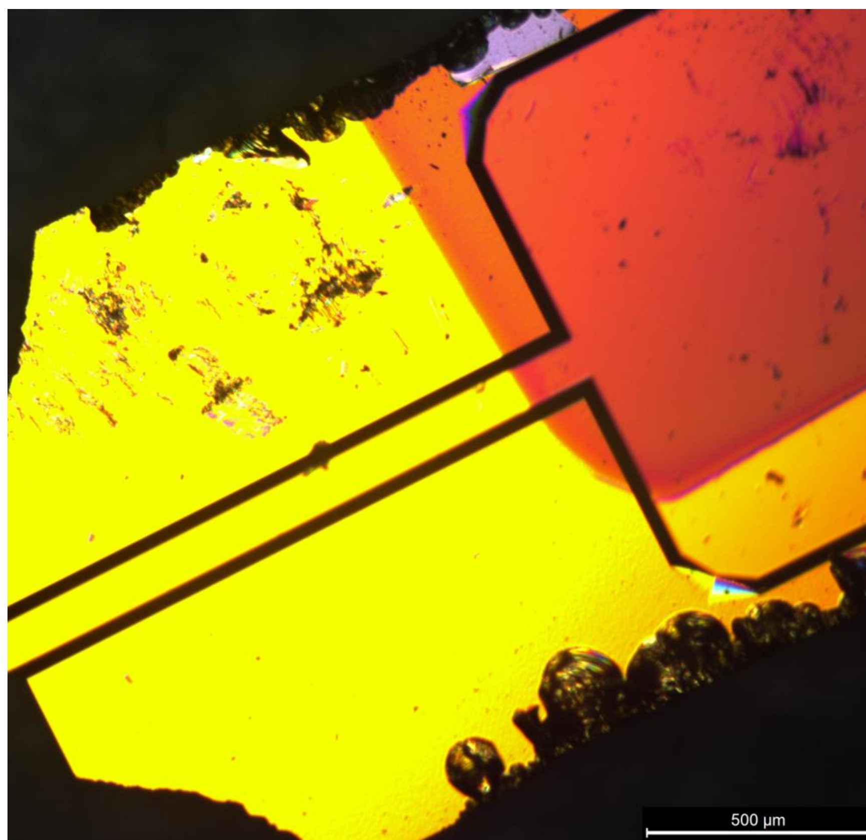

FIG. 4.4. Damage to cantilever body caused by tweezers during handling, which resulted in a between the Si and Ti/Au electrical pathways.

4.2.3 Application of NW NSMM Probes to Biological Samples

Recent application of NSMM to biological systems has opened new avenues for their characterization, however, the risk of damaging relatively delicate cellular structures during scanning sets a variety of constraints on probe design[135-138]. In NSMM, the probe is scanned in contact with the sample of interest to increase sensitivity to localized surface and sub-surface changes in resistivity and permittivity. Furthermore, NSMM requires a unique, high-aspect ratio probe that maximizes cantilever-sample distance and subsequently minimizes unwanted stray capacitance from the cantilever. Finally, application of NSMM to life sciences, where imaging often takes place in fluid environments, necessitates a corrosion-resistant probe.

A wafer-scale process for fabricating NSMM NW probes outlined in Section 4.3 will be ideally suited for studying biological systems. Living cells, in particular, make for fragile samples and necessitate a sensitive feedback system coupled with a flexible probe to achieve successful contact-mode imaging. Previous work with CNT tips has demonstrated their usefulness for topographical measurements on cells[139-141]. CNTs eliminate unwanted scanning artifacts relative to a pyramidal Si tip while their flexible nature enable imaging of contoured, cavity rich, and delicate cellular structures without damage[100]. However, CNTs fail to make ideal NSMM probes for two reasons:

1. Their small radius restricts their effective length to ~50 nm. Beyond this length, scanning artifacts arise due to tip bending. While this upper-limit on size is typically negligible for purely topographical scans, high signal-to-noise NSMM measurements require a sample-cantilever separation of at least several microns to reduce background stray capacitance.
2. Second, selective growth of a single CNT perpendicular to the cantilever is difficult to achieve. This makes integration of CNTs with a wafer-scale fabrication process problematic, requiring that each CNT be individually placed during probe creation.

GaN NWs, with a typical radius of 50 nm to 150 nm, are thicker than their CNT counterparts. When high tip resolution is a concern, annular tip milling in the FIB can be used to achieve <20 nm tip radius (Fig. 4.5). The larger diameter of a GaN NW allows for longer probe lengths that are immune to both scanning artifacts and stray capacitance during scanning.

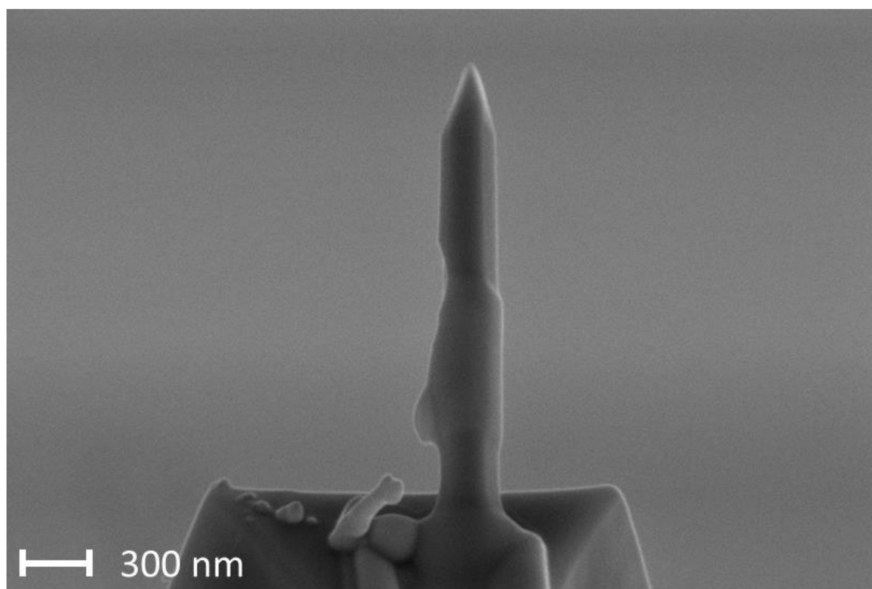

FIG. 4.5. GaN NW probe that has been annular milled in the FIB to achieve a ~ 20 nm tip radius. Image credited to Paul Blanchard.

The advantages of NSMM for studying biological systems have only recently begun to be investigated. This includes work on deriving ionic strength information from human leukemia cells[137] and imaging the morphological interaction between carbon nanotubes (CNT) and muscle cells[138]. Of important note is Jewook Park's research, that provides an ideal format for testing the sensitivity of a new probe design[135]. The resonant frequency and quality factor of the microwave S_{11} were tracked as a function of NaCl concentration in water to verify high sensitivity to minute variations in cellular salinity. Scans of an epidermal monolayer of a *Y. filamentosa* leaf revealed microwave contrast between cell wall and cytoplasm due to differing water content. Further testing on animal tissue successfully differentiated between blood vessels and osseous tissue (bone matrix) due to the higher dielectric index of the blood.

In addition to its suitability for imaging nanostructures and permittivity changes in biological systems, a GaN NW NSMM probe would be ideal for spatial and temporal tracking of metallic ions in mammalian cells. Metallic ion concentrations are maintained at extremely low levels under

resting conditions. However, perturbations caused by oxidative stress and nitric oxide cellular signals generate relatively high levels of free metallic ion signals that are, in turn, critical for a variety of biological processes[142-143]. A greater understanding of the origin and location of these free metallic ions would provide invaluable insight into the fundamental relationships between metal regulation and cellular function. Work currently underway at CU Boulder's BioFrontier's program focuses on protein-based fluorescent sensors that bind to and enable the detection of metallic ions. Since fluorescent sensors are tracked optically, this method is only suitable for relatively small, transparent cells[143]. A GaN NW NSMM probe could compliment this technique by providing a direct method of imaging metallic, sub-surface imbalances without relying on external markers that may alter cellular function.

Bibliography

1. Synge, E. H., A suggested method for extending microscopic resolution into the ultra-microscopic region. *Philos Mag* **1928,** *6* (35), 356-362.

2. Soohoo, R. F., A Microwave Magnetic Microscope. *Journal of Applied Physics* **1962,** *33* (3), 1276-1277.

3. Frait, Z.; Kamberský, V.; MÁlek, Z.; Ondris, M., Local variations of uniaxial anisotropy in thin films. *Czechoslovak Journal of Physics* **1960,** *10* (8), 616-617.

4. Ash, E.; Nicholls, G., Super-resolution aperture scanning microscope. **1972**.

5. Bryant, C.; Gunn, J., Noncontact technique for the local measurement of semiconductor resistivity. *Review of Scientific Instruments* **1965,** *36* (11), 1614-1617.

6. Fee, M.; Chu, S.; Hänsch, T., Scanning electromagnetic transmission line microscope with sub-wavelength resolution. *Opt Commun* **1989,** *69* (3), 219-224.

7. Gao, C.; Xiang, X. D., Quantitative microwave near-field microscopy of dielectric properties. *Review of Scientific Instruments* **1998,** *69* (11), 3846-3851.

8. Talanov, V. V.; Scherz, A.; Moreland, R. L.; Schwartz, A. R., A near-field scanned microwave probe for spatially localized electrical metrology. *Applied physics letters* **2006,** *88* (13), 134106-134106-3.

9. Kim, J.; Lee, K.; Friedman, B.; Cha, D., Near-field scanning microwave microscope using a dielectric resonator. *Applied physics letters* **2003,** *83* (5), 1032-1034.

10. Imtiaz, A.; Anlage, S. M., A novel STM-assisted microwave microscope with capacitance and loss imaging capability. *Ultramicroscopy* **2003,** *94* (3), 209-216.

11. Hovsepyan, A.; Babajanyan, A.; Sargsyan, T.; Melikyan, H.; Kim, S.; Kim, J.; Lee, K.; Friedman, B., Direct imaging of photoconductivity of solar cells by using a near-field scanning microwave microprobe. *Journal of Applied Physics* **2009,** *106* (11), 114901-114901-6.

12. Kim, J.; Babajanyan, A.; Sargsyan, T.; Melikyan, H.; Kim, S.; Friedman, B.; Lee, K., Investigation of photoconductivity of silicon solar cells by a near-field scanning microwave microscope. *Ultramicroscopy* **2009,** *109* (8), 958-962.

13. Chisum, J. D. Low-noise Instrumentation for Near-field Microwave Microscopy. University of Colorado, 2011.

14. Anlage, S. M.; Talanov, V. V.; Schwartz, A. R., Principles of near-field microwave microscopy. *Scanning Probe Microscopy: Electrical and Electromechanical Phenomena at the Nanoscale* **2007,** *1*, 215-253.

15. Binnig, G.; Rohrer, H., Scanning tunneling microscopy. *Surface Science* **1983,** *126* (1), 236-244.

16. Betzig, E.; Finn, P.; Weiner, J., Combined shear force and near-field scanning optical microscopy. *Applied physics letters* **1992,** *60* (20), 2484-2486.

17. Toledo-Crow, R.; Yang, P.; Chen, Y.; Vaez-Iravani, M., Near-field differential scanning optical microscope with atomic force regulation. *Applied physics letters* **1992,** *60* (24), 2957-2959.

18. Talanov, V. V.; Moreland, R. L.; Scherz, A.; Schwartz, A. R.; Liu, Y. In *Scanning Near-Field Microwave Probe for In-line Metrology of Low-K Dielectrics*, MRS Proceedings, Cambridge Univ Press: 2004.

19. Kim, M. S.; Kim, S.; Kim, J.; Lee, K.; Friedman, B.; Kim, J. T.; Lee, J., Tip–sample distance control for near-field scanning microwave microscopes. *Review of Scientific Instruments* **2003,** *74* (8), 3675-3678.

20. Gao, C.; Hu, B.; Takeuchi, I.; Chang, K.-S.; Xiang, X.-D.; Wang, G., Quantitative scanning evanescent microwave microscopy and its applications in characterization of functional materials libraries. *Measurement Science and Technology* **2005,** *16* (1), 248.

21. Tabib-Azar, M.; Wang, Y., Design and fabrication of scanning near-field microwave probes compatible with atomic force microscopy to image embedded nanostructures. *Microwave Theory and Techniques, IEEE Transactions on* **2004,** *52* (3), 971-979.

22. Van der Weide, D.; Neuzil, P., The nanoscilloscope: Combined topography and AC field probing with a micromachined tip. *Journal of Vacuum Science & Technology B: Microelectronics and Nanometer Structures* **1996,** *14* (6), 4144-4147.

23. Tselev, A.; Anlage, S. M.; Christen, H. M.; Moreland, R. L.; Talanov, V. V.; Schwartz, A. R., Near-field microwave microscope with improved sensitivity and spatial resolution. *Review of Scientific Instruments* **2003,** *74* (6), 3167-3170.

24. Lipson, A.; Lipson, S. G.; Lipson, H., *Optical physics*. Cambridge University Press: 2010.

25. Xiang, X. D.; Gao, C., Quantitative complex electrical impedance microscopy by scanning evanescent microwave microscope. *Materials characterization* **2002,** *48* (2), 117-125.

26. Imtiaz, A., *Quantitative materials contrast at high spatial resolution with a novel near-field scanning microwave microscope*. 2005.

27. Pozar, D. M., *Microwave engineering*. John Wiley & Sons: 2009.

28. Tabib-Azar, M.; Su, D. P.; Pohar, A.; LeClair, S.; Ponchak, G., 0.4 μm spatial resolution with 1 GHz (λ= 30 cm) evanescent microwave probe. *Review of Scientific Instruments* **1999,** *70* (3), 1725-1729.

29. Bourgoin, J. P.; Johnson, M.; Michel, B., Semiconductor characterization with the scanning surface harmonic microscope. *Applied physics letters* **1994,** *65* (16), 2045-2047.

30. Gao, C.; Duewer, F.; Xiang, X. D., Quantitative microwave evanescent microscopy. *Applied physics letters* **1999,** *75* (19), 3005-3007.

31. Imtiaz, A.; Baldwin, T.; Nembach, H. T.; Wallis, T. M.; Kabos, P., Near-field microwave microscope measurements to characterize bulk material properties. *Applied physics letters* **2007,** *90* (24), 243105-243105-3.

32. C. Balusek, B. F., D. Luna, B. Oetiker, A. Babajanyan, and K. Lee, A three-dimensional finite elment model of near-field scanning microwave microscopy. Unpublished.

33. Chapin, D.; Fuller, C.; Pearson, G., A New Silicon p-n Junction Photocell for Converting Solar Radiation into Electrical Power. *Journal of Applied Physics* **1954,** *25* (5), 676-677.

34. Miles, R.; Hynes, K.; Forbes, I., Photovoltaic solar cells: An overview of state-of-the-art cell development and environmental issues. *Progress in Crystal Growth and Characterization of Materials* **2005,** *51* (1), 1-42.

35. Gray, J. L., The physics of the solar cell. *by A. Luque, S. Hegedus.–Chichester: John Wiley & Sons Ltd* **2003**, 61-112.

36. Pierret, R. F., *Semiconductor device fundamentals*. Addison-Wesley Reading, MA: 1996.

37. Pankove, J. I., *Optical processes in semiconductors*. Dover Publications: 2010.

38. Fraas, L. M.; Partain, L. D., *Solar cells and their applications*. Wiley: 2010; Vol. 217.

39. Green, M. A., Solar cells: operating principles, technology, and system applications. *Englewood Cliffs, NJ, Prentice-Hall, Inc., 1982. 288 p.* **1982,** *1*.

40. Green, M. A.; Emery, K.; King, D. L.; Igari, S.; Warta, W., Short communication: Solar cell efficiency tables (version 25). *Progress in Photovoltaics: Research and Applications* **2005,** *13* (1), 49-54.

41. Willeke, G. P. In *The crystalline silicon solar cell—history, achievements and perspectives*, Proceedings of the 19th European Photovoltaic Solar Energy Conference, Paris, 2004; pp 383-386.

42. Ralph, E. In *Recent advancements in low cost solar cell processing*, 11th Photovoltaic Specialists Conference, 1975; p 315.

43. Loferski, J. In *Tandem photovoltaic solar cells and increased solar energy conversion efficiency*, 12th Photovoltaic Specialists Conference, 1976; pp 957-961.

44. Gokcen, N.; Loferski, J., Efficiency of tandem solar cell systems as a function of temperature and solar energy concentration ratio. *Solar Energy Materials* **1979,** *1* (3), 271-286.

45. Razykov, T.; Ferekides, C.; Morel, D.; Stefanakos, E.; Ullal, H.; Upadhyaya, H., Solar photovoltaic electricity: Current status and future prospects. *Solar Energy* **2011,** *85* (8), 1580-1608.

46. Ramanathan, K.; Contreras, M. A.; Perkins, C. L.; Asher, S.; Hasoon, F. S.; Keane, J.; Young, D.; Romero, M.; Metzger, W.; Noufi, R., Properties of 19.2% efficiency ZnO/CdS/CuInGaSe2 thin-film solar cells. *Progress in Photovoltaics: Research and Applications* **2003,** *11* (4), 225-230.

47. Albin, D. S.; Carapella, J. J.; Tuttle, J. R.; Contreras, M. A.; Gabor, A. M.; Noufi, R.; Tennant, A. L., Recrystallization method to selenization of thin-film Cu (In, Ga) Se. sub. 2 for semiconductor device applications. Google Patents: 1995.

48. Contreras, M. A.; Egaas, B.; Ramanathan, K.; Hiltner, J.; Swartzlander, A.; Hasoon, F.; Noufi, R., Progress toward 20% efficiency in Cu (In, Ga) Se2 polycrystalline thin-film solar cells. *Progress in Photovoltaics: Research and Applications* **1999,** *7* (4), 311-316.

49. Contreras, M. A.; Romero, M. J.; To, B.; Hasoon, F.; Noufi, R.; Ward, S.; Ramanathan, K., Optimization of CBD CdS process in high-efficiency Cu (In, Ga) Se< sub> 2</sub>-based solar cells. *Thin Solid Films* **2002,** *403*, 204-211.

50. Tuttle, J. R.; Contreras, M. A.; Ward, J. S.; Gabor, A. M.; Ramanathan, K. R.; Tennant, A. L.; Wang, L.; Keane, J.; Noufi, R. In *High-efficiency Cu(In,Ga)Se₂-based thin-film solar cells: 16.8% total-area 1-sun and 17.2% total-area 22-sun device performance*, Photovoltaic Energy Conversion, 1994., Conference Record of the Twenty Fourth. IEEE Photovoltaic Specialists Conference - 1994, 1994 IEEE First World Conference on, 5-9 Dec 1994; 1994; pp 1942-1945 vol.2.

51. Rau, U.; Schock, H. W., Cu (In, Ga) Se2 solar cells. *Clean Electricity from Photovoltaics* **2001,** 277-345.

52. Research Cell Efficiency Records. www.nrel.gov/ncpv/ (accessed May 21st, 2014).

53. Holt, D.; Ogden, R., Observation of dislocations in a silicon phototransistor by scanning electron microscopy using the barrier electron voltaic effect. *Solid-State Electronics* **1976,** *19* (1), 37-40.

54. Mattis, R. L.; Baroody, A. J., *Carrier lifetime measurement by the photoconductive decay method*. US Dept. of Commerce, National Bureau of Standards: 1972; Vol. 736.

55. Chen, M., Photoconductivity lifetime measurements on HgCdTe using a contactless microwave technique. *Journal of Applied Physics* **1988,** *64* (2), 945-947.

56. Borrego, J.; Gutmann, R.; Jensen, N.; Paz, O., Non-destructive lifetime measurement in silicon wafers by microwave reflection. *Solid-State Electronics* **1987,** *30* (2), 195-203.

57. Ahrenkiel, R. K., Minority-carrier lifetime in iii-v semiconductors. *Semiconductors and semimetals* **1993,** *39*, 39-150.

58. Orton, J. W.; Blood, P., The electrical characterization of semiconductors: measurement of minority carrier properties. *Techniques of physics* **1990,** (13).

59. Bachrach, R., A photon counting apparatus for kinetic and spectral measurements. *Review of Scientific Instruments* **1972,** *43* (5), 734-737.

60. Kazmerski, L. L., Photovoltaics characterization- A survey of diagnostic measurements. *Journal of materials research* **1998,** *13* (10), 2684-2708.

61. Schaafsma, D.; Mossadegh, R.; Sanghera, J.; Aggarwal, I.; Gilligan, J.; Tolk, N.; Luce, M.; Generosi, R.; Perfetti, P.; Cricenti, A., Singlemode chalcogenide fiber infrared SNOM probes. *Ultramicroscopy* **1999,** *77* (1), 77-81.

62. Mönig, H.; Smith, Y.; Caballero, R.; Kaufmann, C.; Lauermann, I.; Lux-Steiner, M. C.; Sadewasser, S., Direct Evidence for a Reduced Density of Deep Level Defects at Grain Boundaries of Cu (In, Ga) Se_ {2} Thin Films. *Physical review letters* **2010,** *105* (11), 116802.

63. Binnig, G.; Quate, C. F.; Gerber, C., Atomic force microscope. *Physical review letters* **1986,** *56* (9), 930-933.

64. Azulay, D.; Millo, O.; Balberg, I.; Schock, H. W.; Visoly-Fisher, I.; Cahen, D., Current routes in polycrystalline CuInSe< sub> 2</sub> and Cu (In, Ga) Se< sub> 2</sub> films. *Solar energy materials and solar cells* **2007,** *91* (1), 85-90.

65. Reid, O. G.; Munechika, K.; Ginger, D. S., Space charge limited current measurements on conjugated polymer films using conductive atomic force microscopy. *Nano letters* **2008,** *8* (6), 1602-1609.

66. Coffey, D. C.; Reid, O. G.; Rodovsky, D. B.; Bartholomew, G. P.; Ginger, D. S., Mapping local photocurrents in polymer/fullerene solar cells with photoconductive atomic force microscopy. *Nano letters* **2007,** *7* (3), 738-744.

67. Xin, H.; Reid, O. G.; Ren, G.; Kim, F. S.; Ginger, D. S.; Jenekhe, S. A., Polymer Nanowire/Fullerene Bulk Heterojunction Solar Cells: How Nanostructure Determines Photovoltaic Properties. *ACS nano* **2010,** *4* (4), 1861-1872.

68. Nonnenmacher, M.; Oboyle, M.; Wickramasinghe, H., Kelvin probe force microscopy. *Applied physics letters* **1991,** *58* (25), 2921-2923.

69. Marrón, D. F.; Sadewasser, S.; Meeder, A.; Glatzel, T.; Lux-Steiner, M. C., Electrical activity at grain boundaries of Cu (In, Ga) Se_ {2} thin films. *Phys Rev B* **2005,** *71* (3), 033306.

70. Rusu, M.; Glatzel, T.; Neisser, A.; Kaufmann, C.; Sadewasser, S.; Lux-Steiner, M. C., Formation of the physical vapor deposited CdS∕Cu (In, Ga) Se interface in highly efficient thin film solar cells. *Applied physics letters* **2006,** *88*, 143510.

71. Rusu, M.; Bar, M.; Lehmann, S.; Sadewasser, S.; Weinhardt, L.; Kaufmann, C.; Strub, E.; Rohrich, J.; Bohne, W.; Lauermann, I., Three-dimensional structure of the buffer/absorber interface in< equation>< font face='verdana'> CdS/< font face='verdana'> CuGaSe< sub> 2</sub></equation> based thin film solar cells. *Applied physics letters* **2009,** *95* (17), 173502-173502-3.

72. Glatzel, T.; Rusu, M.; Sadewasser, S.; Lux-Steiner, M. C., Surface photovoltage analysis of thin CdS layers on polycrystalline chalcopyrite absorber layers by Kelvin probe force microscopy. *Nanotechnology* **2008,** *19* (14), 145705.

73. Coffey, D. C.; Ginger, D. S., Time-resolved electrostatic force microscopy of polymer solar cells. *Nature materials* **2006,** *5* (9), 735-740.

74. Reid, O. G.; Rayermann, G. E.; Coffey, D. C.; Ginger, D. S., Imaging Local Trap Formation in Conjugated Polymer Solar Cells: A Comparison of Time-Resolved Electrostatic Force Microscopy and Scanning Kelvin Probe Imaging†. *The Journal of Physical Chemistry C* **2010,** *114* (48), 20672-20677.

75. Giridharagopal, R.; Rayermann, G. E.; Shao, G.; Moore, D. T.; Reid, O. G.; Tillack, A. F.; Masiello, D. J.; Ginger, D. S., Submicrosecond Time Resolution Atomic Force Microscopy for Probing Nanoscale Dynamics. *Nano letters* **2012,** *12* (2), 893-898.

76. Gütay, L.; Pomraenke, R.; Lienau, C.; Bauer, G. H., Subwavelength inhomogeneities in Cu (In, Ga) Se2 thin films revealed by near-field scanning optical microscopy. *physica status solidi (a)* **2009,** *206* (5), 1005-1008.

77. Cadby, A.; Khalil, G.; Fox, A.; Lidzey, D., Mapping exciton quenching in photovoltaic-applicable polymer blends using time-resolved scanning near-field optical microscopy. *Journal of Applied Physics* **2008,** *103* (9), 093715-093715-5.

78. Hecht, B.; Sick, B.; Wild, U. P.; Deckert, V.; Zenobi, R.; Martin, O. J. F.; Pohl, D. W., Scanning near-field optical microscopy with aperture probes: Fundamentals and applications. *The Journal of Chemical Physics* **2000,** *112*, 7761.

79. Kim, S.; Yoo, H.; Lee, K.; Friedman, B.; Gaspar, M. A.; Levicky, R., Distance control for a near-field scanning microwave microscope in liquid using a quartz tuning fork. *Applied physics letters* **2005,** *86* (15), 153506-153506-3.

80. Imtiaz, A.; Wallis, T. M.; Lim, S. H.; Tanbakuchi, H.; Huber, H. P.; Hornung, A.; Hinterdorfer, P.; Smoliner, J.; Kienberger, F.; Kabos, P., Frequency-selective contrast on variably doped p-type silicon with a scanning microwave microscope. *Journal of Applied Physics* **2012,** *111* (9), 093727-093727-6.

81. Kim, M. S.; Kim, S.; Kim, J.; Lee, K.; Friedman, B.; Kim, J.-T.; Lee, J., Tip--sample distance control for near-field scanning microwave microscopes. *Review of Scientific Instruments* **2003,** *74* (8), 3675-3678.

82. Caughey, T.; O'Kelly, M., Effect of damping on the natural frequencies of linear dynamic systems. *Journal of the Acoustical Society of America* **1961,** *33* (11), 1458-1461.

83. Dennis, T.; Schlager, J. B.; Yuan, H. C.; Wang, Q.; Friedman, D. In *A novel solar simulator based on a super-continuum laser*, Photovoltaic Specialists Conference (PVSC), 2012 38th IEEE, IEEE: 2012; pp 001845-001848.

84. Künzel, H.; Döhler, G.; Ploog, K., Determination of photoexcited carrier concentration and mobility in GaAs doping superlattices by hall effect measurements. *Applied Physics A: Materials Science & Processing* **1982,** *27* (1), 1-10.

85. Yu, L.; Liu, Q.; Guan, Z.; Lau, S., Direct measurement of the refractive index change of silicon with optically injected carriers. *Applied physics letters* **1996,** *68* (11), 1546-1548.

86. Noufi, R.; Gabor, A. M.; Tuttle, J. R.; Tennant, A. L.; Contreras, M. A.; Albin, D. S.; Carapella, J. J., Method of fabricating high-efficiency Cu (In, Ga)(SeS). sub. 2 thin films for solar cells. Google Patents: 1995.

87. Jiang, C. S.; Noufi, R.; AbuShama, J.; Ramanathan, K.; Moutinho, H.; Pankow, J.; Al-Jassim, M., Local built-in potential on grain boundary of< equation>< font face='verdana'> Cu (In, Ga) Se< sub> 2</sub></equation> thin films. *Applied physics letters* **2004,** *84* (18), 3477-3479.

88. McDaniel, A. A.; Hsu, J.; Gabor, A., Near-field scanning optical microscopy studies of< equation>< font face='verdana'> Cu (In, Ga) Se< sub>< font face='verdana'> 2</sub></equation> solar cells. *Applied physics letters* **1997,** *70* (26), 3555-3557.

89. Eich, D.; Herber, U.; Groh, U.; Stahl, U.; Heske, C.; Marsi, M.; Kiskinova, M.; Riedl, W.; Fink, R.; Umbach, E., Lateral inhomogeneities of Cu (In, Ga) Se< sub> 2</sub> absorber films. *Thin Solid Films* **2000,** *361*, 258-262.

90. Loader, C., *Local regression and likelihood*. springer New York: 1999.

91. Polzehl, J.; Spokoiny, V., Propagation-separation approach for local likelihood estimation. *Probability Theory and Related Fields* **2006,** *135* (3), 335-362.

92. Kaelin, M.; Rudmann, D.; Kurdesau, F.; Meyer, T.; Zogg, H.; Tiwari, A., CIS and CIGS layers from selenized nanoparticle precursors. *Thin Solid Films* **2003,** *431*, 58-62.

93. Jiang, C. S.; Noufi, R.; Ramanathan, K.; AbuShama, J.; Moutinho, H.; Al-Jassim, M., Does the local built-in potential on grain boundaries of Cu (In, Ga) Se thin films benefit photovoltaic performance of the device? *Applied physics letters* **2004,** *85*, 2625.

94. Sadewasser, S.; Abou-Ras, D.; Azulay, D.; Baier, R.; Balberg, I.; Cahen, D.; Cohen, S.; Gartsman, K.; Ganesan, K.; Kavalakkatt, J., Nanometer-scale electronic and microstructural properties of grain boundaries in Cu (In, Ga) Se2. *Thin Solid Films* **2011,** *519* (21), 7341-7346.

95. Rau, U.; Taretto, K.; Siebentritt, S., Grain boundaries in Cu (In, Ga)(Se, S) 2 thin-film solar cells. *Applied Physics A: Materials Science & Processing* **2009,** *96* (1), 221-234.

96. Zhang, X.-Y.; Wang, X.-C.; Xu, F.; Ma, Y.-G.; Ong, C. K., High frequency dielectric properties distribution of BiFeO[sub 3] thin film using near-field microwave microscopy. *Review of Scientific Instruments* **2009,** *80* (11), 114701.

97. Michel, B.; Mizutani, W.; Schierle, R.; Jarosch, A.; Knop, W.; Benedickter, H.; Bachtold, W.; Rohrer, H., Scanning surface harmonic microscopy: Scanning probe microscopy based on microwave field-induced harmonic generation. *Review of Scientific Instruments* **1992,** *63* (9), 4080-4085.

98. Wintle, H.; Kurylowicz, S., Edge corrections for strip and disc capacitors. *Instrumentation and Measurement, IEEE Transactions on* **1985,** *34* (1), 41-47.

99. Gomila, G.; Toset, J.; Fumagalli, L., Nanoscale capacitance microscopy of thin dielectric films. *Journal of Applied Physics* **2008,** *104* (2), 024315-024315-8.

100. Kalinin, S.; Kalinin, S. V. e.; Gruverman, A., *Scanning probe microscopy*. Springer: 2007.

101. Hafner, J. H.; Cheung, C. L.; Lieber, C. M., Growth of nanotubes for probe microscopy tips. *Nature* **1999,** *398* (6730), 761-762.

102. Dai, H.; Hafner, J. H.; Rinzler, A. G.; Colbert, D. T.; Smalley, R. E., Nanotubes as nanoprobes in scanning probe microscopy. *Nature* **1996,** *384* (6605), 147-150.

103. Li, J. F.; Huang, Y. F.; Ding, Y.; Yang, Z. L.; Li, S. B.; Zhou, X. S.; Fan, F. R.; Zhang, W.; Zhou, Z. Y.; Ren, B., Shell-isolated nanoparticle-enhanced Raman spectroscopy. *Nature* **2010,** *464* (7287), 392-395.

104. Flöhr, K.; Sladek, K.; Günel, H. Y.; Lepsa, M. I.; Hardtdegen, H.; Liebmann, M.; Schäpers, T.; Morgenstern, M., Scanning tunneling microscopy with InAs nanowire tips. *Applied physics letters* **2012,** *101* (24), 243101.

105. Kalkbrenner, T.; Ramstein, M.; Mlynek, J.; Sandoghdar, V., A single gold particle as a probe for apertureless scanning near-field optical microscopy. *Journal of Microscopy* **2001,** *202* (1), 72-76.

106. Burt, D. P.; Wilson, N. R.; Weaver, J. M.; Dobson, P. S.; Macpherson, J. V., Nanowire probes for high resolution combined scanning electrochemical Microscopy-Atomic force Microscopy. *Nano letters* **2005,** *5* (4), 639-643.

107. Ju, Y.; Hamada, M.; Kobayashi, T.; Soyama, H., A microwave probe nanostructure for atomic force microscopy. *Microsystem Technologies* **2009,** *15* (8), 1195-1199.

108. Lai, K.; Kundhikanjana, W.; Kelly, M. A.; Shen, Z. X., Calibration of shielded microwave probes using bulk dielectrics. *Applied physics letters* **2008,** *93* (12), 123105.

109. Lai, K.; Kundhikanjana, W.; Kelly, M.; Shen, Z. X., Modeling and characterization of a cantilever-based near-field scanning microwave impedance microscope. *Review of Scientific Instruments* **2008,** *79* (6), 063703.

110. Weide, D. W. v. d., Localized picosecond resolution with a near-field microwave/scanning-force microscope. *Applied physics letters* **1997,** *70* (6), 677-679.

111. Rosner, B. T.; Weide, D. W. v. d., High-frequency near-field microscopy. *Review of Scientific Instruments* **2002,** *73* (7), 2505-2525.

112. Engstrom, D. S.; Savu, V.; Zhu, X.; Bu, I. Y. Y.; Milne, W. I.; Brugger, J.; Boggild, P., High throughput nanofabrication of silicon nanowire and carbon nanotube tips on afm probes by stencil-deposited catalysts. *Nano letters* **2011,** *11* (4), 1568-1574.

113. Burt, D. P.; Wilson, N. R.; Weaver, J. M. R.; Dobson, P. S.; Macpherson, J. V., Nanowire probes for high resolution combined scanning electrochemical Microscopy-Atomic force Microscopy. *Nano letters* **2005,** *5* (4), 639-643.

114. Tay, A. B. H.; Thong, J. T. L., High-resolution nanowire atomic force microscope probe grown by a field-emission induced process. *Applied physics letters* **2004,** *84* (25), 5207-5209.

115. Lee, W.; Jeong, M. C.; Myoung, J. M., Catalyst-free growth of ZnO nanowires by metal-organic chemical vapour deposition (MOCVD) and thermal evaporation. *Acta Materialia* **2004,** *52* (13), 3949-3957.

116. Bertness, K. A.; Sanford, N. A.; Davydov, A. V., GaN nanowires grown by molecular beam epitaxy. *Selected Topics in Quantum Electronics, IEEE Journal of* **2011,** *17* (4), 847-858.

117. Bertness, K. A.; Schlager, J. B.; Sanford, N. A.; Roshko, A.; Harvey, T. E.; Davydov, A. V.; Levin, I.; Vaudin, M. D.; Barker, J. M.; Blanchard, P. T. In *High degree of crystalline perfection*

in spontaneously grown GaN nanowires, Materials Research Society Symposium Proceedings, Warrendale, Pa.; Materials Research Society; 1999: 2006; p 799.

118. Bertness, K. A.; Roshko, A.; Mansfield, L. M.; Harvey, T. E.; Sanford, N. A., Nucleation conditions for catalyst-free GaN nanowires. *Journal of crystal growth* **2007,** *300* (1), 94-99.

119. Bertness, K. A.; Sanford, N. A.; Barker, J. M.; Schlager, J. B.; Roshko, A.; Davydov, A. V.; Levin, I., Catalyst-free growth of GaN nanowires. *J Electron Mater* **2006,** *35* (4), 576-580.

120. Huber, H. P.; Moertelmaier, M.; Wallis, T. M.; Chiang, C. J.; Hochleitner, M.; Imtiaz, A.; Oh, Y. J.; Schilcher, K.; Dieudonne, M.; Smoliner, J., Calibrated nanoscale capacitance measurements using a scanning microwave microscope. *Review of Scientific Instruments* **2010,** *81* (11), 113701-113701-9.

121. Tanbakuchi, H., The challenges of the Nanoscale material and deivce characterization. Unpublished.

122. Rocky Mountain Nanotechnology, LLC. (accessed 10/30/12).

123. Fabreguette, F.; Sechrist, Z.; Elam, J.; George, S., Quartz crystal microbalance study of tungsten atomic layer deposition using WF< sub> 6</sub> and Si< sub> 2</sub> H< sub> 6</sub>. *Thin Solid Films* **2005,** *488* (1), 103-110.

124. George, S. M., Atomic layer deposition: an overview. *Chemical reviews* **2009,** *110* (1), 111-131.

125. Klaus, J.; Ferro, S.; George, S., Atomic layer deposition of tungsten using sequential surface chemistry with a sacrificial stripping reaction. *Thin Solid Films* **2000,** *360* (1), 145-153.

126. Rossnagel, S.; Noyan, I.; Cabral Jr, C., Phase transformation of thin sputter-deposited tungsten films at room temperature. *Journal of Vacuum Science & Technology B* **2002,** *20* (5), 2047-2051.

127. Sloggett, G.; Barton, N.; Spencer, S., Fringing fields in disc capacitors. *Journal of Physics A: Mathematical and General* **1986,** *19* (14), 2725.

128. Radisavljevic, B.; Radenovic, A.; Brivio, J.; Giacometti, V.; Kis, A., Single-layer MoS2 transistors. *Nature nanotechnology* **2011,** *6* (3), 147-150.

129. Mak, K. F.; Lee, C.; Hone, J.; Shan, J.; Heinz, T. F., Atomically thin MoS 2: a new direct-gap semiconductor. *Physical review letters* **2010,** *105* (13), 136805.

130. Novoselov, K. S.; Geim, A. K.; Morozov, S.; Jiang, D.; Zhang, Y.; Dubonos, S.; Grigorieva, I.; Firsov, A., Electric field effect in atomically thin carbon films. *science* **2004,** *306* (5696), 666-669.

131. Sanders, A., **2012**.

132. Brubaker, M. D.; Blanchard, P. T.; Schlager, J. B.; Sanders, A. W.; Herrero, A. M.; Roshko, A.; Duff, S. M.; Harvey, T. E.; Bright, V. M.; Sanford, N. A., Toward Discrete Axial p–n Junction Nanowire Light-Emitting Diodes Grown by Plasma-Assisted Molecular Beam Epitaxy. *J Electron Mater* **2013**, 1-7.

133. Brubaker, M. D.; Blanchard, P. T.; Schlager, J. B.; Sanders, A. W.; Roshko, A.; Duff, S. M.; Gray, J. M.; Bright, V. M.; Sanford, N. A.; Bertness, K. A., On-Chip Optical Interconnects Made with Gallium Nitride Nanowires. *Nano letters* **2013,** *13* (2), 374-377.

134. Greytak, A. B.; Barrelet, C. J.; Li, Y.; Lieber, C. M., Semiconductor nanowire laser and nanowire waveguide electro-optic modulators. *Applied physics letters* **2005,** *87*, 151103.

135. Park, J.; Hyun, S.; Kim, A.; Kim, T.; Char, K., Observation of biological samples using a scanning microwave microscope. *Ultramicroscopy* **2005,** *102* (2), 101-106.

136. Friedman, B.; Gaspar, M. A.; Kalachikov, S.; Lee, K.; Levicky, R.; Shen, G.; Yoo, H., Sensitive, label-free DNA diagnostics based on near-field microwave imaging. *Journal of the American Chemical Society* **2005,** *127* (27), 9666-9667.

137. Oh, Y. J.; Huber, H.-P.; Hochleitner, M.; Duman, M.; Bozna, B.; Kastner, M.; Kienberger, F.; Hinterdorfer, P., High-frequency electromagnetic dynamics properties of THP1 cells using scanning microwave microscopy. *Ultramicroscopy* **2011,** *111* (11), 1625-1629.

138. Farina, M.; Di Donato, A.; Monti, T.; Pietrangelo, T.; Da Ros, T.; Turco, A.; Venanzoni, G.; Morini, A., Tomographic effects of near-field microwave microscopy in the investigation of muscle cells interacting with multi-walled carbon nanotubes. *Applied physics letters* **2012,** *101* (20), -.

139. Uchihashi, T.; Choi, N.; Tanigawa, M.; Ashino, M.; Sugawara, Y.; Nishijima, H.; Akita, S.; Nakayama, Y.; Tokumoto, H.; Yokoyama, K., Carbon-nanotube tip for highly-reproducible imaging of deoxyribonucleic acid helical turns by noncontact atomic force microscopy. *Japanese Journal of Applied Physics* **2000,** *39*, 887.

140. Nishijima, H.; Kamo, S.; Akita, S.; Nakayama, Y.; Hohmura, K. I.; Yoshimura, S. H.; Takeyasu, K., Carbon-nanotube tips for scanning probe microscopy: Preparation by a controlled process and observation of deoxyribonucleic acid. *Applied physics letters* **1999,** *74* (26), 4061-4063.

141. Chen, L.; Cheung, C. L.; Ashby, P. D.; Lieber, C. M., Single-walled carbon nanotube AFM probes: optimal imaging resolution of nanoclusters and biomolecules in ambient and fluid environments. *Nano letters* **2004,** *4* (9), 1725-1731.

142. Dean, K. M.; Qin, Y.; Palmer, A. E., Visualizing metal ions in cells: An overview of analytical techniques, approaches, and probes. *Biochimica et Biophysica Acta (BBA)-Molecular Cell Research* **2012,** *1823* (9), 1406-1415.

143. Dittmer, P. J.; Miranda, J. G.; Gorski, J. A.; Palmer, A. E., Genetically encoded sensors to elucidate spatial distribution of cellular zinc. *Journal of Biological Chemistry* **2009,** *284* (24), 16289-16297.